10-21-2013

Direct Observation of the Second 2+ State in 12C

William R. Zimmerman
zimmerman@phys.uconn.edu

Direct Observation of the Second $J^\pi = 2^+$ State in ^{12}C

William R. Zimmerman, Ph.D.

University of Connecticut, 2013

A low-lying $J^\pi = 2^+$ state in ^{12}C was predicted over fifty years ago to exist as an excitation of the Hoyle state. The exact energy, width, and electromagnetic transition probability of this state is related to the structure of the Hoyle state, and measuring these parameters will help to constrain the various models which attempt to describe the clustering phenomenon in light nuclei. The second 2^+ state in ^{12}C was directly observed in the ^{12}C(γ,α)^{8}Be reaction using the intense, nearly mono-energetic γ-ray beams available at the High Intensity γ-ray Source (HIγS) facility. The α particles produced by the photodisintegration of ^{12}C were detected using an optical time projection chamber (OTPC), which allowed for the complete angular distributions necessary to definitively confirm the 2^+ nature of the state. This unique combination of a Compton-backscattered γ-ray beam and and an active-target system made possible the first unambiguous identification of this 2^+ state. The second 2^+ state in ^{12}C was found at an excitation energy of $E_{\rm x} = 10.13^{+0.06}_{-0.05}$ MeV, with a width of $\Gamma = 2080^{+330}_{-260}$ keV, and with a γ-decay width to the ground state of $\Gamma_\gamma = 135^{+16}_{-12}$ meV. The previously-measured first 1^- state in ^{12}C was found at an excitation energy of $E_{\rm x} = 10.913^{+0.020}_{-0.018}$ MeV, with a width of $\Gamma = 305^{+40}_{-36}$ keV, and an isospin-forbidden γ-decay width to the ground state of $\Gamma_\gamma = 32.4^{+2.1}_{-2.0}$ meV. These results are compared with predictions made by the various models that describe the structure of the excited states in ^{12}C. This 2^+ state increases astrophysical helium-burning reaction rates at the high temperatures which are thought to occur during core-collapse supernovae. New triple-α reaction rates have been calculated based on these results, and their possible impact on explosive nucleosynthesis is discussed.

Direct Observation of the Second $J^\pi = 2^+$ State in ^{12}C

William R. Zimmerman

Bachelor of Science, University of Connecticut, 2006

Master of Science, University of Connecticut, 2011

A Dissertation

Submitted in Partial Fullfilment of the

Requirements for the Degree of

Doctor of Philosophy

at the

University of Connecticut

2013

Approval Page

Doctor of Philosophy Dissertation

Direct Observation of the Second $J^\pi = 2^+$ State in ^{12}C

Presented by

William R. Zimmerman, B.S., M.S.

Major Advisor

Richard T. Jones

Associate Advisor

Henry R. Weller

Associate Advisor

Jeffrey S. Schweitzer

University of Connecticut

2013

Acknowledgements

First and foremost, I must express my deep gratitude to my advisor Henry, who brought me to Durham and always represented to me everything that a scientist should be. Henry's door is always open, and I have learned far more physics from Henry than from any class or textbook.

I must thank all those who worked with me in the Radiative Capture Group at TUNL: Mo, Sean, Jon, Luke, Mark, Adam, Indra, and David. These are the people who worked closely with me and were always ready to help solve any problem. I have enjoyed so many discussions over the years, and I have learned so much from such and exceptional group of colleagues.

I will always be indebted to my fellow graduate students at the University of Connecticut who helped form my fundamental understanding of physics and academia.

Of course, I must acknowledge my mother Judy and my father David, whose encouragement, love, and support brought me to where I am today.

Most of all, I need to thank my wonderful wife Melanie. Six years ago, Melanie convinced me to apply to graduate school. She has been my biggest supporter and source of inspiration, and I could not have done this without her.

Contents

List of Figures

List of Tables

List of Acronyms

ADC	Analog-to-Digital Converter
API	Application Programming Interface
ALA	Auxiliary Lens Assembly
BEC	Bose-Einstein Condensate
BGO	Bismuth Germanium Oxide
BNC	Bayonet Neill-Concelman
CCD	Charge-Coupled Device
DFELL	Duke Free Electron Laser Laboratory
EB	Event Builder
ECL	Emitter-Coupled Logic
EFT	Effective Field Theory
FADC	Flash Analog-to-Digital Converter
FMD	Fermionic Molecular Dynamics
FEL	Free Electron Laser
G/D	Gate and Delay generator
HIγS	High Intensity γ-ray Source
HPGe	High-Purity Germanium
linac	Linear Accelerator
MCP	Micro-Channel Plate
MLA	Main Lens Assembly
NACRE	Nuclear Astrophysics Compilation of Reaction Rates
NIM	Nuclear Instrumentation Module
OK	Optical Klystron
OTPC	Optical Time Projection Chamber
PDF	Probability Distribution Function
PMT	Photo-Multiplier Tube
RAID	Redundant Array of Independent Disks
RAM	Random Access Memory
RF	Radio Frequency
ROC	Read-Out Control
SBC	Single Board Computer
SRIM	Stopping and Range of Ions in Matter
TFA	Timing Filtering Amplifier
TTL	Transistor-Transistor Logic
TUNL	Triangle Universities Nuclear Laboratory

Chapter 1

Introduction

This dissertation describes a measurement performed at the High Intensity γ-ray Source (HIγS) facility at Triangle Universities Nuclear Laboratory (TUNL) to identify and measure the second $J^\pi = 2^+$ state in ^{12}C, predicted over fifty years ago to exist as an excitation of the Hoyle state [Mor56].

Many theoretical models have recently been advanced to describe the structure of the Hoyle state and its possible 2^+ excitation. A confirmation of the existence of the 2_2^+ state in ^{12}C and a measurement of its parameters would serve to constrain these models and elucidate the α-clustering phenomenon in light nuclei.

In addition to its theoretical implications, the 2_2^+ state in ^{12}C would serve as a resonance in the ^{8}Be(α,γ)^{12}C reaction, increasing the thermonuclear reaction rate of the triple-α process at high temperatures (Section 1.4). The exact parameters of the 2_2^+ state will affect the outcome of heavy element production during the explosive nucleosynthesis which is thought to occur during core-collapse supernovae and other astrophysical phenomena.

While recent interest has led to assorted experimental efforts (described in Section 1.3) to identify the 2_2^+ state, background contributions from the overlapping 0_3^+ and 3_1^- states have led to conflicting results and ambiguities in the existence and parameters of the 2_2^+ state in ^{12}C. Figure 1.1 shows the ^{12}C level scheme.

This experiment used the Compton-backscattered γ-ray beams from the HIγS facility [Wel09] to selectively populate excited states in ^{12}C. Since a photon beam cannot populate the 0_3^+ state and has a very small probability for populating the 3_1^-

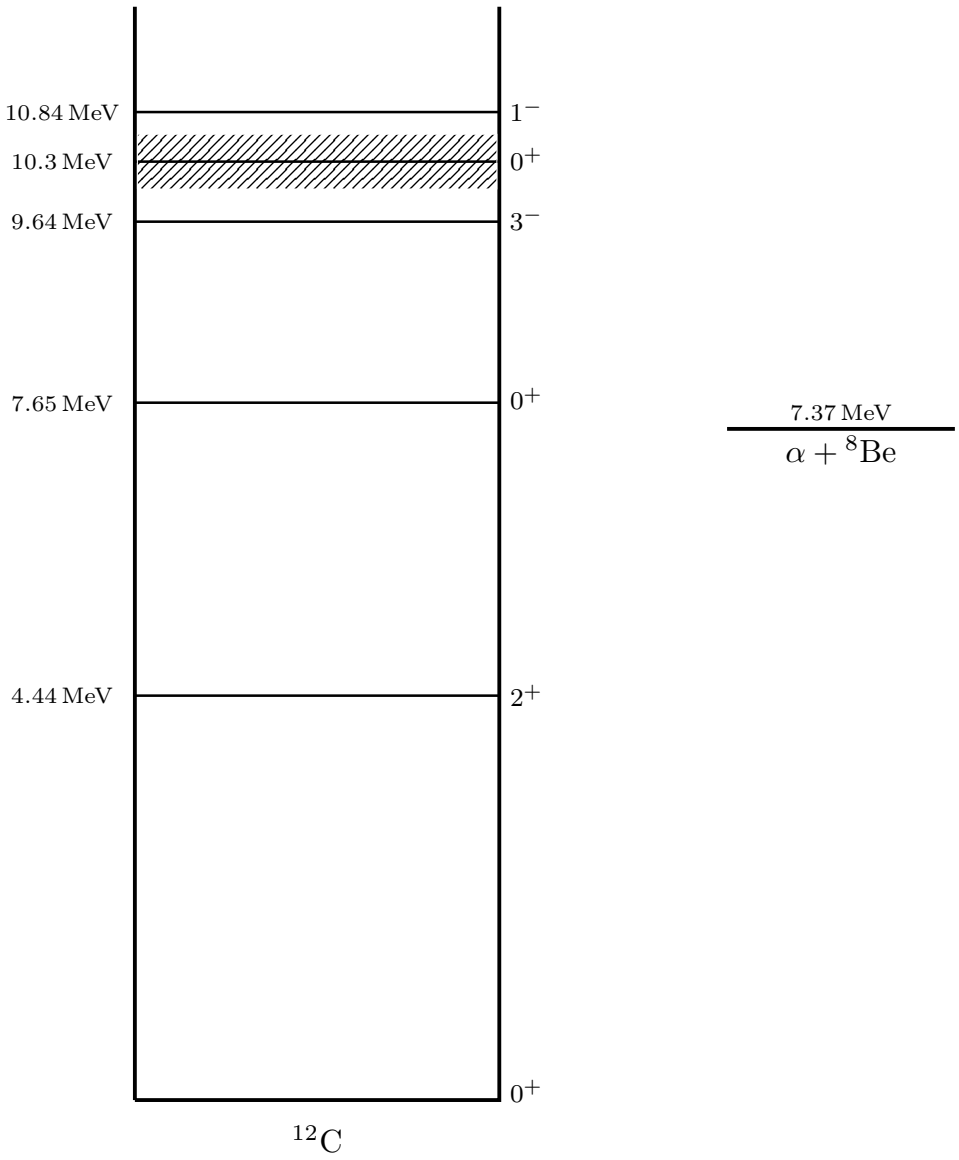

Figure 1.1: Adopted level scheme of ^{12}C [Ajz90]. Previous experimental efforts to identify the 2_2^+ state have been limited by background contributions from the 3_1^- and 0_3^+ states at 9.64 MeV and 10.3 MeV, respectively.

state, this approach represents an ideal way to search for the 2_2^+ state and measure its parameters, with the only other likely contribution arising from the 1_1^- state at $E_{\mathrm{x}} = 10.84\,\mathrm{MeV}$ [Ajz90]. The $E1$ and $E2$ components of the cross section were separated in order to accurately determine the parameters of both the 2_2^+ state as well as the 1_1^- state.

The α particles produced in the ^{12}C(γ,α_0)^{8}Be reaction were detected using an optical time projection chamber (OTPC) active-target system. Photographs of the charged-particle tracks from each event allowed for the discrimination of background events and the kinematic reconstructions necessary for the complete angular distributions required to separate the $E1$ and $E2$ amplitudes.

Preliminary results from this experiment have been previously reported [Zim13].

1.1 The Triple-α Process & the Hoyle State

It is believed that most of the carbon in the universe is produced in stars which have exhausted their supply of hydrogen. The cores of these stars are comprised mainly of helium, and Bethe [Bet39] conjectured that no significant amount of any element heavier than helium can be produced by stellar thermonuclear reactions due to the lack of stable nuclear isotopes with mass numbers between 5 and 8.

In order to explain the existence of elements heavier than helium, Salpeter [Sal52] and Öpic [Öpi51] each hypothesized that the production of ^{12}C could proceed through the intermediate nucleus ^{8}Be. Although it is unstable to α decay ($\Gamma_\alpha = 5.57(25)$ eV [Til04]), Salpeter and Öpik postulated that a small amount of ^{8}Be exists in a thermal equilibrium in the stellar cores, and a ^{8}Be nucleus may radiatively capture an α particle to form ^{12}C [Sal52]:

$$\begin{aligned} \alpha + \alpha &\rightleftharpoons {}^8\mathrm{Be} \\ \alpha + {}^8\mathrm{Be} &\rightarrow {}^{12}\mathrm{C} + \gamma \end{aligned} \tag{1.1}$$

Hoyle surmised [Hoy53] that in order for this 'triple-α process' to produce enough carbon to explain the observed natural abundances of light elements, there must exist

a resonance in the $\alpha + {}^{8}$Be reaction corresponding to a natural-parity excited state in ^{12}C. The energy of the resonance must be close to the thermal kinetic energy of α particles and ^{8}Be nuclei at a temperature of 10^{8} K, which is thought to occur in the cores of helium-burning stars. Hoyle predicted that this resonance should exist at 0.33 MeV above the $\alpha+{}^{8}$Be threshold, corresponding to a state in ^{12}C with excitation energy $E_{\mathrm{x}} = 7.70$ MeV [Hoy54].

Before Hoyle's prediction, the experimental evidence for the existence of a state in ^{12}C near 7.7 MeV was somewhat conflicting. A state was observed in the ^{14}N(d,α)^{12}C reaction at 7.62 MeV [Hol40] and 7.3 MeV [Gug47], although this was not confirmed by a similar experiment [Mal51] which found no evidence for a state in this region. Evidence for a state at 7.5 MeV was observed in inelastic proton scattering on ^{12}C [Bri52] and in the ^{9}Be(α,n)^{12}C reaction [Gui52].

At Hoyle's suggestion, Dunbar *et al.* [Dun53] searched for the state once more using the ^{14}N(d,α)^{12}C reaction, and it was definitively identified at $E_{\mathrm{x}} = 7.68(3)$ MeV with a width $\Gamma < 25$ keV. The spin-parity $J^{\pi} = 0^{+}$ was assigned to the state by Cook *et al.* [Coo57], who observed α-decays following the β-decay of ^{12}B. The state is now known as the 'Hoyle state,' and its adopted energy and width are [Ajz90]: $E_{\mathrm{x}} = 7.6542(15)$ MeV and $\Gamma = 8.5(10)$ eV.

Because the Hoyle state in ^{12}C is close in energy to the three-α-particle threshold and has $J^{\pi}; T = 0^{+}; 0$, it is widely regarded to be an α-cluster state [Ike68], in which the twelve nucleons are arranged into three distinct groups of α-particle-like clusters.

1.2 2^{+} Excitation of the Hoyle State

While the cluster nature of the Hoyle state is generally accepted, the structure and arrangement of the three constituent α-clusters remains unknown [Fyn11]. One

possible experimental investigation into the structure of the Hoyle state is the identification of its possible rotational excitation. Assuming that the Hoyle state wavefunction has some intrinsic anisotropy, then there should exist a 2^+ state with an excitation energy equal to $\frac{3\hbar^2}{I}$ above the Hoyle state [Boh75], where I is the moment of inertia. The greater the deformation, the smaller the gap in energy between the Hoyle state and its 2^+ rotational excitation. A measurement of a second 2^+ state in ^{12}C will therefore determine the moment of inertia of the Hoyle state under the assumption that the two states are members of a rotational band. For example, Morinaga [Mor56] conjectured that the structure of the Hoyle state consists of a linear chain of α-clusters and calculated that its subsequent 2^+ rotational excitation should be found at $E_\mathrm{x} = 9.7\,\mathrm{MeV}$.

The measurement of a 2^+ state in ^{12}C above the Hoyle state would also give insight into the α-cluster structure even if the two states are not members of a rotational band. Several theoretical predictions [Yam05, Che07] show a non-rotational 2^+ excitation of the Hoyle state, and an unambiguous measurement of the resulting 2^+_2 state in ^{12}C would constrain the various models and shed light onto the α-cluster structure of the Hoyle state. Predictions made by various models are discussed in Chapter 2.

1.3 Previous Experiments

Recent interest in the α-clustering phenomenon and the structure of the Hoyle state [Fyn11, Fre12a, Ebr12, Oer06] has led to several experimental attempts to measure the 2^+_2 state in ^{12}C, with somewhat inconsistent results. Table 1.1 shows the results of the previous measurements.

Inelastic Scattering

Itoh *et al.* [Ito04] were the first to observe experimental evidence for the existence of the 2_2^+ state in ^{12}C near 10 MeV using the inelastic scattering of 386 MeV α particles incident on a ^{12}C target. With improved statistics [Ito11] they used a multipole decomposition analysis to conclude the existence of an unexplained $\ell = 2$ strength corresponding to the 2_2^+ state in ^{12}C at $E_{\rm x} = 9.84(6)$ MeV with a width of $\Gamma = 1010(150)$ keV.

Freer *et al.* [Fre09] performed a similar inelastic scattering experiment using 66 MeV and 200 MeV protons and a high-resolution magnetic spectrometer. They concluded that the line shapes of the resulting energy spectra suggested the existence of a broad $\Gamma = 600(100)$ keV 2^+ state at $E_{\rm x} = 9.6(1)$ MeV submerged beneath the 0_3^+ state at 10.3 MeV and the 3_1^- state at 9.6 MeV. A separate experiment [Zim11] also measured the ^{12}C(p,p') reaction using 25 MeV protons and reported results consistent with Freer *et al.* A subsequent re-analysis [Fre12b] of the experimental data from the ^{12}C(p,p') data from Freer *et al.* [Fre09] as well as the ^{12}C(α,α') data from Itoh *et al.* [Ito04, Ito11] showed the 2_2^+ state to be an excitation energy of $E_{\rm x} = 9.75(15)$ MeV with a width of $\Gamma = 600(100)$ keV.

All of the inelastic scattering experiments are limited by contributions from the 0_3^+ and 3_1^- states, and the extracted parameters of the 2_2^+ state depend strongly on the subtraction of the resulting background.

β-Delayed α-Decay

Fynbo *et al.* [Fyn05, Dig05] searched for the 2_2^+ state by populating the low-lying excited states in ^{12}C through the β-decays of ^{12}B and ^{12}N. The excitation spectrum of ^{12}C was reconstructed by measuring the energy of the subsequent three-α-particle

decays. Since this method can only populate 0^+, 1^+, and 2^+ states in ^{12}C, the results are not sensitive to any contribution from the 3^-_1 state. Fynbo *et al.* reported that their measured α-particle spectra corresponding to excitation energies in ^{12}C near 10 MeV could be explained by interfering 0^+ states and concluded that the previously-reported 2^+_2 state is likely nonexistent. The same group later reported [Hyl10] that with improved statistics and analysis techniques there was evidence for a 2^+ state at $E_\mathrm{x} = 11.1(3)$ MeV, significantly higher in energy than the state seen in the inelastic scattering experiments.

$^{10/11}$B(^{3}He,p/d)^{12}C

Several recent experiments [Smi12, Alc12] investigated the spectrum of the low-lying excited states in ^{12}C using ^{3}He beams incident on boron targets. Smit *et al.* [Smi12] used a high-resolution magnetic spectrometer to detect deuterons from the ^{11}B(^{3}He,d)^{12}C reaction. Their results are consistent with a 2^+ state in ^{12}C at $E_\mathrm{x} = 9.7$ MeV, and they categorically exclude the existence of a 2^+ state near $E_\mathrm{x} = 11$ MeV as was seen in the β-delayed α-decay experiments [Fyn05, Dig05, Hyl10].

A similar experiment was performed by Alcorta *et al.* [Alc12], who used an array of double-sided silicon strip detectors to detect protons and deuterons from the ^{10}B(^{3}He,p)^{12}C and ^{11}B(^{3}He,d)^{12}C reactions, respectively. In addition, they detected the α particles from the subsequent decay of the excited ^{12}C nucleus. They found no evidence of any new 2^+ state in ^{12}C.

The various conflicting experimental evidence suggests the need for for a new direct measurement to identify any new 2^+ excited state in ^{12}C. An unambiguous identification of the state would resolve this experimental incongruity.

Table 1.1: Parameters of the 2_2^+ state in ^{12}C as measured in previous experiments.

Experiment	Ref.	E_x (MeV)	Γ (keV)
β-delayed α-decay	[Fyn05, Dig05]	(no state)	—
	[Hyl10]	11.1(3)	1400(400)
^{12}C(x,x′)^{12}C	[Fre12b]†	9.75(15)	750(150)
	[Fre09, Zim11]	9.6(1)	600(100)
	[Ito11, Ito04]	9.84(6)	1010(150)
$^{10/11}$B(^{3}He,p/d)^{12}C	[Smi12]	9.7	—
	[Alc12]	(no state)	—

†The results presented by Freer *et al.* [Fre12b] represent a re-analysis of previously published inelastic scattering data [Fre09, Ito11, Ito04]

1.4 High Temperature Triple-α Reaction Rates

Most of the heavy elements in the universe are believed to originate in the nucleosynthesis which occurs during supernovae and other explosive astrophysical phenomena [Bur57], and individual thermonuclear reaction rates can have a profound impact on the chemical evolution of galaxies [Bra12].

In red giant stars, the hydrostatic burning of helium into carbon is governed completely by a single resonance in ^{12}C—the Hoyle state [Rol88]. However, for helium burning at the higher temperatures associated with explosive nucleosynthesis, higher-lying resonances in ^{12}C may significantly increase the thermonuclear triple-α reaction rates [Buc06].

The production of heavy elements during explosive nucleosynthesis is influenced by these changes in the triple-α reaction rate at high temperatures [Eid05]. For example, Bravo *et al.* [Bra12] calculated that the production of nitrogen, nickel, copper, zinc, and titanium during type Ia supernovae is especially sensitive to the triple-α reaction rate at temperatures from 1–10 GK. Furthermore, changes to the rate of

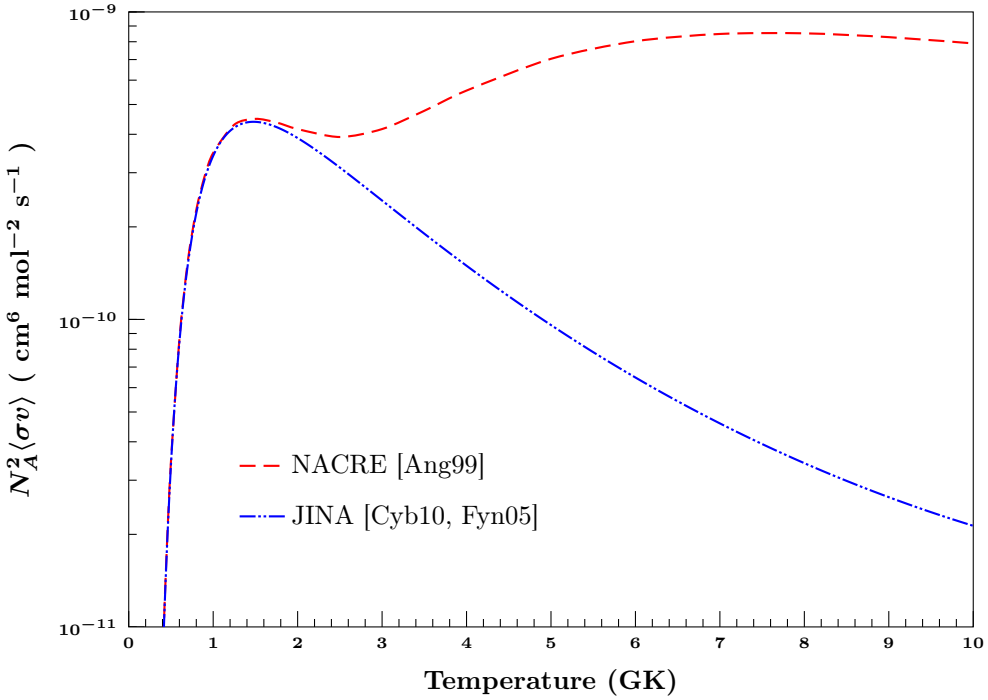

Figure 1.2: Triple-α reaction rates listed in the NACRE compilation [Ang99] compared with those listed in the JINA-REACLIB compilation [Cyb10]. The NACRE reaction rates include the contribution from a theoretical 2_2^+ state in ^{12}C; the JINA rates are based on the experimental results of Fynbo *et al.* [Fyn05], and do not include any significant contribution from any 2_2^+ state.

the triple-α reaction will affect the results of a newly-discovered explosive nucleosynthesis mechanism known as the νp-process [Frö06]—in which neutrino-driven winds induce (n, p) reactions in heavy nuclei—which is thought to occur during core-collapse supernovae. Wanajo *et al.* [Wan11] calculated the effect that changes in the high-temperature triple-α reaction rate would have on the final abundances of elements produced during the νp-process. They found that at temperatures above 3 GK, the triple-α process dominates the flow from $A < 12$ to $A \geq 12$ over the competing ^{7}Be$(\alpha,\gamma)^{11}$C$(\alpha, p)^{14}$N and ^{7}Be$(\alpha,p)^{10}$B$(\alpha, p)^{13}$C reactions. The increased triple-α reaction rates due to contributions from resonances above the Hoyle state in ^{12}C will substantially reduce the production of proton-rich nuclei in the mass range

$A = 100$–110 [Wan11]. This effect is due in part to the absorption of protons by ^{12}C and other nuclei produced as a result of the triple-α process, which would otherwise contribute to the synthesis of heavy elements.

Figure 1.2 shows the triple-α reaction rates published in several recent compilations. The Nuclear Astrophysics Compilation of Reaction Rates (NACRE) [Ang99] includes in their calculated rates a purely theoretical 2_2^+ state in ^{12}C at $E_{\mathrm{x}} = 9.12\,\mathrm{MeV}$ with an α-decay width of $\Gamma_\alpha = 560\,\mathrm{keV}$ and a γ-decay width of $\Gamma_\gamma = 200\,\mathrm{meV}$. The Joint Institute for Nuclear Astrophysics (JINA) 'REACLIB' database [Cyb10] lists the rates calculated using the results from the β-delayed α-decay experiment of Fynbo *et al.* [Fyn05]. Unlike the NACRE reaction rates, the rates listed by JINA do not include a contribution from a 2_2^+ state in ^{12}C, and the reaction rates listed by the two compilations disagree at high temperatures by more than an order of magnitude.

Resolving this long-standing ambiguity in the existence and properties of the 2_2^+ state in ^{12}C and in the resulting triple-α reaction rates at high temperatures will help to constrain the models which attempt to explain the observed abundances of heavy elements in the universe [Die11].

Chapter 2

Models of the ^{12}C Nucleus

Following the failure of various attempts to describe the Hoyle state with shell model calculations [Coh65, Kar95, Nav00a, Nav00b], nuclear models incorporating α-clustering have emerged with predictions regarding low-lying excited states in ^{12}C. In 1987, Descouvemont and Baye [Des87] pioneered a microscopic cluster model which treats the ^{12}C nucleus as a three-α-particle system and manages to accurately reproduce the energy of the Hoyle state. Since then, many different models have attempted to accurately describe the structure of ^{12}C.

Table 2.1: Theoretical predictions of the parameters of the 1^-_1 and 2^+_2 states in ^{12}C measured in this experiment from selected models describing the structure of the low-lying excited states in ^{12}C. $E_{\rm x}$ is the excitation energy of the state, γ^2_α is the reduced α-decay width (see Section 5.2.4), and B($E\lambda \rightarrow 0^+_1$) represents the reduced electromagnetic transition probability to the ground state (see Section 5.2.4).

Theory	Ref.	State	$E_{\rm x}$ (MeV)	γ^2_α (keV)	B($E\lambda \rightarrow 0^+_1$) (e^2 fm$^{2\lambda}$)
Microscopic Cluster	[Des87]	1^-_1	12.50	61.5	—
		2^+_2	9.27	356	4.1
BEC	[Yam05]	1^-_1	10.48	—	—
		2^+_2	9.7	1200	—
FMD	[Che07, Nef12]	2^+_2	10.06	—	0.46
EFT	[Epe12]	2^+_2	9.65	—	2(1)

†The FMD 2^+_2 energy was calculated from the predicted energy difference relative to the three-α threshold [Nef12].

Below are descriptions of three selected leading models of the ^{12}C nucleus: (i) a Bose-Einstein condensate (BEC) theory which models the ^{12}C nucleus as three α particles in a dilute degenerate gas, (ii) a model based on fermionic molecular dynamics (FMD) which begins with single-particle Gaussian wave packets and predicts an α-cluster structure for many of the low-lying excited states of ^{12}C, and (iii) *ab initio* lattice calculations in the framework of chiral effective field theory (EFT), which also predict α clustering for low-lying states in ^{12}C without assuming it *a priori*. Table 2.1 summarizes the predictions made by these models regarding the parameters of the 1_1^- and 2_2^+ states in ^{12}C measured in this experiment.

2.1 Bose-Einstein Condensate (BEC)

Tohsaki *et al.* [Toh01] pioneered the description of excited states in ^{12}C nucleus as a degenerate α-particle condensate. They started with a simple wavefunction to describe N α clusters:

$$|\Phi_{N\alpha}\rangle = \left(C_\alpha^\dagger\right)^N |0\rangle, \tag{2.1}$$

where $C_\alpha^\dagger$ is the creation operator for an α-cluster, and the wavefunction can be written as [Toh01, Yam04]:

$$\langle \vec{r}_1 \dots \vec{r}_N | \Phi_{N\alpha}\rangle \propto \mathcal{A}\left\{ e^{-\nu\left(r_1^2 \dots r_N^2\right)} \phi(\alpha_1) \dots \phi(\alpha_N) \right\}, \tag{2.2}$$

where $\phi(\alpha)$ is the internal α-cluster wavefunction, which describes the individual nucleons as Gaussian wave packets. $\mathcal{A}$ antisymmetrizes the individual nucleons within each α cluster, and the parameter ν describes the size of the α clusters. The size of the α clusters as well as the size of the Gaussian wave packets which describe the individual nucleons are left as parameters and are treated variationally. Using an

effective two- and three-nucleon potential [Toh94], Tohsaki *et al.* [Toh01] were able to correctly reproduce the binding energy and radius of ^{4}He as well as the phase shifts from elastic α-α scattering. They showed that for a nucleus consisting of three α-particle clusters there should be a 0^+ state corresponding to three interacting α clusters all occupying the same $0s$ harmonic oscillator state near the three-α breakup threshold, and that this state appears at the same energy as the Hoyle state. Tohsaki *et al.*'s 0^+ state is a dilute system of α clusters with small enough overlap that the Pauli effect between the individual nucleons is quite weak, and the state may be considered to be a condensate of α clusters, similar in structure to a classic BEC. The ground state, however, is predicted to be dense enough that the Pauli effect is important. Therefore, the ground state of ^{12}C can be considered to be neither an α-cluster condensate nor even a state made up of distinct α clusters.

Funaki *et al.* [Fun03] generalized this approach and confirmed the results using different effective nucleon potentials. They further showed that previous microscopic α-cluster calculations were in fact equivalent to the BEC approach, while the BEC approach offers the advantage of greatly reduced degrees of freedom.

The BEC model was extended by Yamada *et al.* [Yam04], who showed that there exists a 0^+ state near the α-breakup threshold in every $4n$ self-conjugate nucleus up to ^{40}Ca. Funaki *et al.* [Fun05] further extended the model by introducing a deformed α-condensate wavefunction and calculated 2^+ and 4^+ excitations of the Hoyle state. They predicted that the 2^+ excitation corresponds to a 2^+_2 state in ^{12}C, and a very large overlap between the 0^+_2 state and the 2^+_2 state indicates that the 2^+_2 state shares the α-condensate nature of the Hoyle state. These results by Funaki *et al.* [Fun05] were supported by calculations from Yamada *et al.* [Yam05], who further extended the model to include the odd-parity Hoyle state excitations, and calculated the parameters of the low-lying excited states in ^{12}C. The results of these calculations

pertaining to the 1^-_1 and 2^+_2 states are listed in Table 2.1.

2.2 Fermionic Molecular Dynamics (FMD)

Unlike the BEC approach or other cluster models, the FMD approach [Rot04] does not assume *a priori* the α-cluster nature of the low-lying excited states in ^{12}C. In the FMD model of the ^{12}C nucleus developed by Chernykh *et al.* [Che07], the wave-function describing the twelve-nucleon system is generated using antisymmetrized single-particle Gaussian wave packets. These states can describe both shell-model configurations as well as cluster states, without presupposing either. In their description of the ^{12}C nucleus, Chernykh *et al.* model the nucleon-nucleon interactions using the potential presented by Roth *et al.* [Rot05], with empirical corrections to reproduce the experimentally-observed properties of the ground states of assorted nuclei with mass numbers $A \leq 48$. The parameters of the single-particle states are treated variationally to minimize the energy of the first three 0^+ states [Che07].

In order to determine the extent of clustering in the low-lying states of ^{12}C, Chernykh *et al.* constructed an α-cluster projection operator using 165 FMD states in which the twelve nucleons are grouped into spinless and isospinless products of four Gaussian wave packets. They found that the ground state has a 52 % overlap with the α-cluster states, the overlap of the Hoyle state is 85 %, and the overlap of the 2^+_2 state is 99 % [Che07]. This supports the conclusion of Tohsaki *et al.* [Toh01] that the ground state of ^{12}C is poorly described by the BEC dilute α-cluster model. The FMD model also concludes that while the Hoyle state does have a large overlap with pure α-cluster configurations, there is still a significant shell-model-like component which cannot be reproduced using the BEC approach.

Furthermore, the leading α-cluster components in the FMD description of the

Hoyle state are ^{8}Be+α configurations, where two of the α clusters are close together and the third is farther away. This type of configuration is not predicted in the BEC model, where the relative positions of the three α clusters are necessarily uncorrelated. The 2_2^+ state is also predicted to have a ^{8}Be+α configuration, but with a prolate bent-arm shape unlike that of the Hoyle state. This difference in structure leads to the conclusion that the Hoyle state and the 2_2^+ state are not members of a rotational band [Che07].

Chernykh *et al.* also a give a specific prediction of the excitation energy of the 2_2^+ state in the FMD model which is listed in Table 2.1.

2.3 Lattice Effective Field Theory (EFT)

As in the FMD approach, lattice EFT calculations do not assume *a priori* an α-cluster structure. Furthermore, the lattice EFT approach is an *ab initio* approach; the wavefunction is not assumed to be a product of Gaussian wave packets or any other prescribed form. Chiral effective field theory is a framework which models the interactions between nucleons as an expansion in powers of nucleon momenta, and provides intrinsic estimates of the theoretical uncertainty which is reduced with each additional term in the expansion. The low-energy expansion of chiral EFT is organized in powers of Q/Λ, where Q is the typical momentum scale associated with the particles, and Λ is the cutoff momentum at which the effective theory breaks down. Lattice EFT is a technique where space and time are discretized in order to numerically calculate properties of systems within the chiral EFT framework, and the cutoff momentum Λ is inversely proportional to the lattice spacing.

Epelbaum *et al.* [Epe09, Epe10a, Epe10b] developed a method for calculating the structure of nuclei up to $A = 12$ using supercomputer EFT lattice simulations.

They used a cutoff momentum of $\Lambda = 314\,\mathrm{MeV}$ which permits convergent solutions for $\mathrm{Q} \lesssim 100\,\mathrm{MeV}$. Their calculations include Coulomb interactions with an effective two-nucleon contact term to avoid singularities arising from two protons on the same lattice site, and isospin symmetry breaking is included using terms which depend on the mass difference between the π_0 and $\pi_\pm$. Three-nucleon interactions are explicitly included in three diagrams at next-to-next-to-leading-order (NNLO or $\mathcal{O}(Q^3/\Lambda^3)$), which allowed Epelbaum *et al.* to correctly reproduce the difference in binding energy between ^{3}He and ^{3}H [Epe10a]. Using an effective four-nucleon interaction, Epelbaum *et al.* also used this method to investigate the α-clustering phenomenon, and they correctly calculated the binding energies of both ^{4}He and ^{8}Be [Epe11].

For the case of the ^{12}C nucleus, Epelbaum *et al.* [Epe12] explicitly calculated the structure of the ground state, the Hoyle state, and its 2^+ excitation. They used six unique initial configurations of six neutrons and six protons, and followed each one forward through discrete steps in time. The configurations that approached a spinless state with the binding energy of ^{12}C were identified as components of the 0^+_1 ground state, while those that approached a spinless state at an intermediate plateau in energy were identified as the components of the 0^+_2 Hoyle state. The structure of the Hoyle state was found to be dominated by α clusters in an oblate triangular or bent-arm configuration. A spin-2 state was also identified as a low-lying 2^+ rotational excitation of the Hoyle state.

Epelbaum *et al.* [Epe12] calculated specific attributes of the 2^+_2 state including the electromagnetic transition rate to the ground state, listed in Table 2.1. They estimated the uncertainty in their simulations using the size of the corrections from including higher order terms, extrapolating to infinite time, and Monte Carlo statistical uncertainties.

Chapter 3

Experiment Description

3.1 High Intensity γ-ray Source (HIγS)

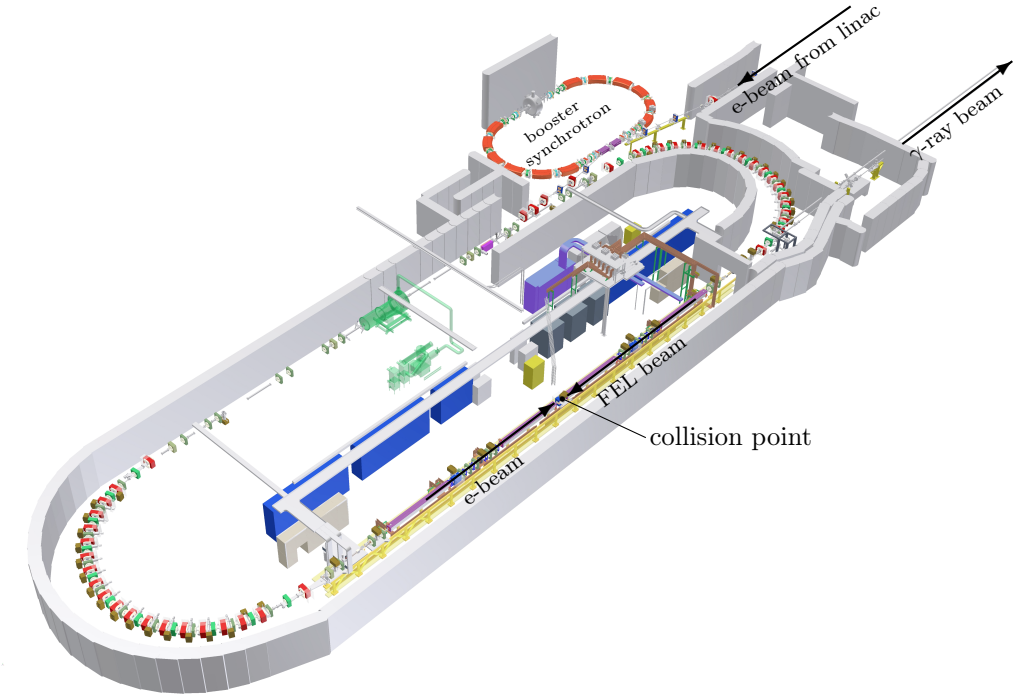

Figure 3.1: The HIγS facility. An electron beam circulating in the storage ring produces coherent FEL light inside an optical cavity. FEL photons are backscattered by the electron beam, and the resulting γ rays propagate downstream to the target.

The High Intensity γ-ray Source (HIγS) at the Duke Free Electron Laser Laboratory (DFELL) is located on the Duke University campus and operated by the Triangle Universities Nuclear Laboratory (TUNL). At the HIγS facility (Figure 3.1), γ-ray beams are produced by the Compton backscattering of free electron laser (FEL) photons. This technique was pioneered by Litvinenko *et. al* [Lit97], and the facility

has since undergone a series of upgrades with significant improvements in performance and reliability [Wel09]. γ-ray beams at HIγS are either linearly or circularly polarized, with on-target intensities of up to $5 \times 10^8\,\gamma/\mathrm{s}$, and available beam energies of 1–100 MeV.

3.1.1 Free Electron Laser

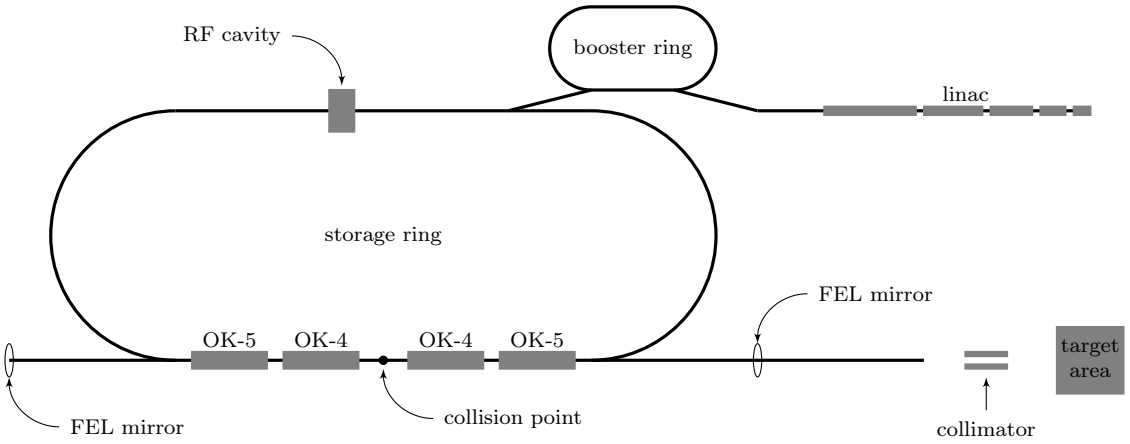

Figure 3.2: Schematic of the HIγS facility. Figure is not drawn to scale.

Figure 3.2 shows a schematic of the accelerators which make up the DFELL: a linear accelerator (linac), a booster ring, and the main electron storage ring.

At the start of the linac, electrons are produced using pulses from a N_2 laser incident on a lanthanum hexaboride (LaB_6) photocathode. The electrons are accelerated in bunches through seven linac sections to an energy of 163 MeV and injected into the booster ring.

The booster ring is an auxiliary synchrotron 31.9 m in circumference which ramps the electrons to their full energy of up to 1.2 GeV and then injects them into the storage ring. Because the electrons are injected at the full energy, the booster ring can continuously top off the storage ring to maintain full electron beam current.

The storage ring is a racetrack-shaped synchrotron with a circumference of 107.46 m. Along the north (upwards in Figure 3.2) straight section is a radio frequency (RF) cavity which bunches the electrons and replaces electron beam energy lost to synchrotron radiation in the curved sections. The RF cavity can also ramp the electron beam energy up or down.

Along the south (downwards in Figure 3.2) straight section are four undulators, also called wigglers. These wigglers make up two optical klystron (OK) configurations capable of producing FEL light: OK-4 for linearly polarized and OK-5 for circularly polarized FEL light. The OK-4 wigglers have a series of coplanar magnets making up 33 periods of 10 cm each. There is a 25 mm gap between the poles of the magnets, which can create a field of up to 536 mT [Lit96, Wu96]. Each of the OK-5 helical wigglers is made up of two planar wigglers: one oriented horizontally and the other oriented vertically. The two planar wigglers are offset by $\frac{1}{4}$ of a period with respect to one another such that the magnetic field causes the electrons to follow a helical path. The OK-5 wigglers have 30 periods of 12 cm each. The gap between the magnets of the OK-5 wigglers is 40 mm, resulting in a maximum field of 286 mT [Lit01, Wu01]. The current experiment exclusively used circularly polarized light from the OK-5 wigglers.

As an electron bunch in the storage ring enters the OK-5 wigglers, the magnetic field causes the electrons to travel in a helical path, radiating circularly polarized photons. Two mirrors are located at either end of the south straight section, defining an optical cavity 53.73 m long, exactly one-half the circumference of the storage ring. Consequently, photons radiated by an ultrarelativistic electron bunch will reflect off of each mirror and co-propagate precisely with the same electron bunch as it travels once again through the wigglers.

As the electron bunch co-propagates with the photons, the electrons interact

with the photons' electromagnetic field. This interaction divides the electron bunch (5–10 cm in length) into micro-bunches separated from one another by the wavelength of the photons (190–1065 nm). When the micro-bunched electrons enter the downstream wiggler, the photons are radiated precisely in phase with those already co-propagating, resulting in coherent FEL light.

3.1.2 γ-Ray Production

HIγS uses collisions of electrons and FEL light to produce nearly monoenergetic γ-ray beams. During γ-ray production, two electron bunches are injected into the storage ring 180° apart. Due to the geometry of the storage ring and the optical cavity, FEL photons produced by one electron bunch will collide head-on with the second electron bunch in the region between the wigglers (Figure 3.2). The Compton backscattering mechanism for producing γ rays is shown in Figure 3.3.

The energy of the outgoing γ ray is given by:

$$E_\gamma = E_{\text{FEL}} \frac{1+\beta}{1+\frac{E_{\text{FEL}}}{E_e} - \left(\beta - \frac{E_{\text{FEL}}}{E_e}\right)\cos\theta}, \tag{3.1}$$

where E_{FEL} is the energy of the FEL photon, E_e is the energy of the incoming electron, β is the ratio of the velocity of the incoming electron to the speed of light, and θ is scattering angle of the outgoing γ ray (Figure 3.3).

For the ultrarelativistic electron beams at HIγS, $\gamma = (1-\beta^2)^{-1/2} \gg 1$. For the case where θ is small, equation 3.1 can be written [Lit97]:

$$E_\gamma \approx E_{\text{FEL}} \frac{4\gamma^2}{1+(\gamma\theta)^2 + 4\gamma^2 \frac{E_{\text{FEL}}}{E_e}}. \tag{3.2}$$

The energy of the outgoing γ ray strongly depends on the scattering angle θ and

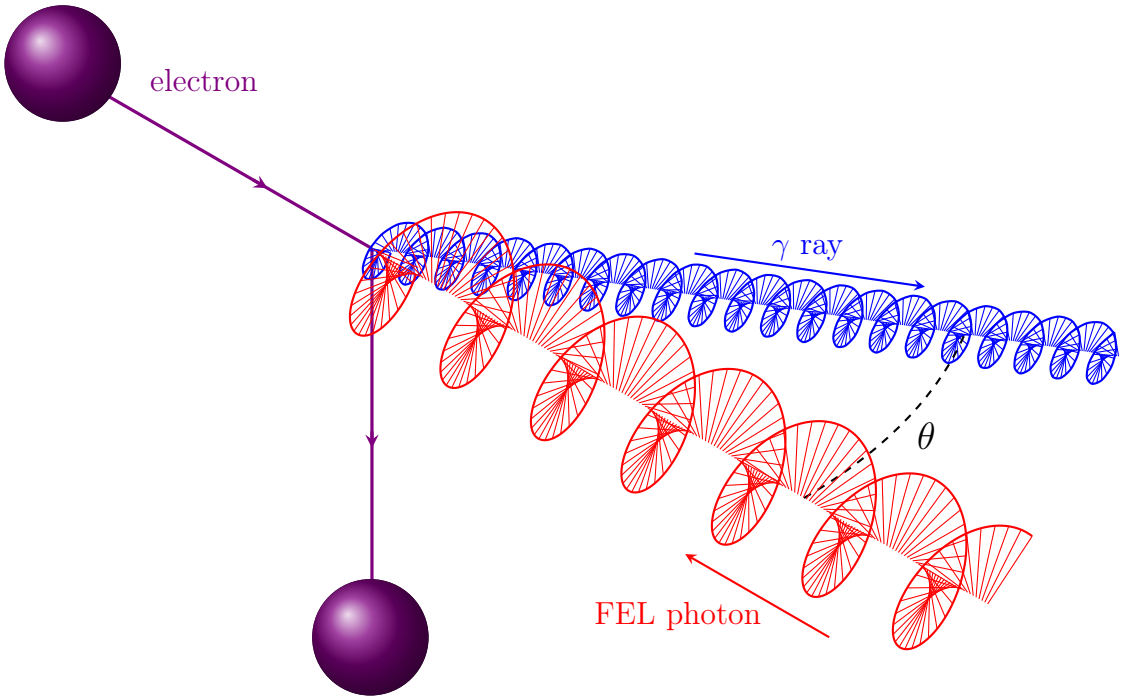

Figure 3.3: γ-ray production through Compton backscattering. An FEL photon (1.2–6.5 eV) collides head-on with a relativistic electron (280–1200 MeV) resulting in an outgoing γ-ray photon (1–100 MeV). The angle θ of the scattered γ ray is exaggerated in the illustration; θ is typically less than one mrad.

peaks at $\theta = 0$. By collimating the γ-ray beam, the highest energy backscattered photons can be selected with minimal energy spread.

3.1.3 Alignment

The γ-ray beam used in this experiment was collimated with a 10.5 mm diameter lead collimator. Because the collimator is approximately 10 m upstream of the target room, the diameter of the γ-ray beam is approximately 12.5 mm by the time it reaches the target. The experimental apparatus has an opening for the beam with a minimum diameter of 15 mm, so precise alignment with respect to the beam is essential.

In order to align the OTPC with respect to the beam, two 4 mm long lead plugs were mounted at the center of the entrance and exit ports of the drift chamber. A

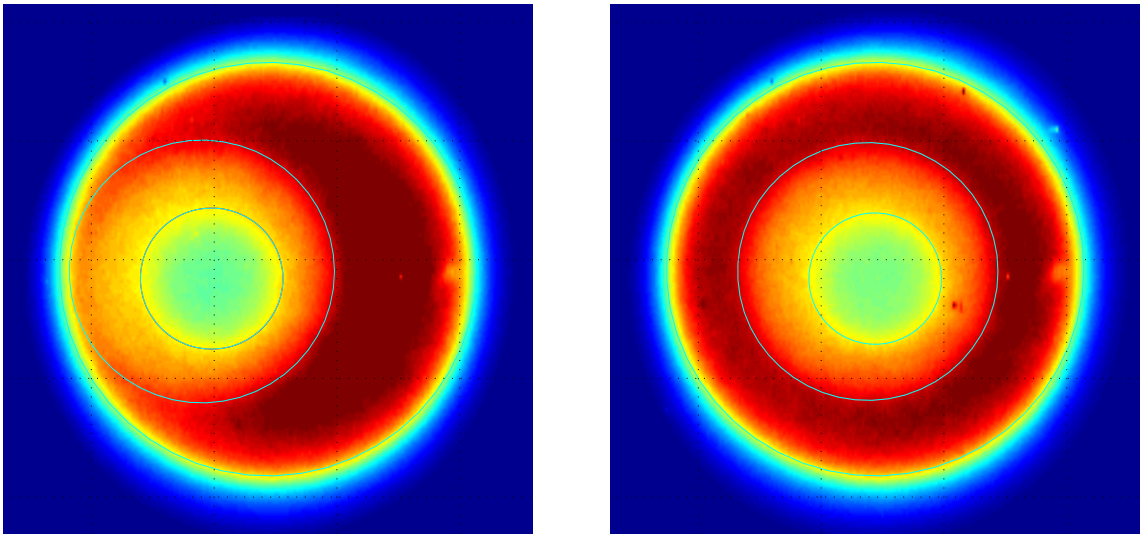

Figure 3.4: Images of the beam downstream of the HIγS OTPC recorded with BGO γ-ray imager [Sun11] before (left) and after (right) alignment. The shadows of two lead plugs mounted at the center of the entrance and exit ports of the drift chamber are visible; the smaller plug is on the entrance window and the larger is on the exit window.

BGO (bismuth germanium oxide, $Bi_4Ge_3O_{12}$) based γ-ray imaging system, developed by Sun [Sun09a], was placed downstream of the OTPC and an image showing the shadows of the two lead plugs was recorded (Figure 3.4). The alignment of the OTPC was then adjusted and the process repeated until the centers of the lead plugs were within 0.3 mm of the center of the beam.

3.2 Beam Diagnostics

3.2.1 Intensity

Absolute Intensity Measurement

The absolute intensity of the γ-ray beam was measured with a large, 10 in $\times$ 12 in NaI(Tl) detector placed directly in the beam. Because the detector could operate at

a maximum useful counting rate of a few kHz, the beam intensity was reduced by approximately five orders of magnitude whenever absolute intensity measurements were taken. Five copper attenuators 35 m upstream of the target are used to reduce the beam intensity by known amounts. Any of the five attenuators can be remotely placed in or out of the beam, and the thickness of each attenuator is known precisely. The attenuation factor of the copper attenuators can be calculated using the published photon attenuation cross sections [Ber98]]. Ahmed *et al.* measured the attenuation of the copper attenuators and found excellent agreement with the published cross sections [Ahm08]. The total systematic uncertainty in the attenuation factor has been previously calculated to be 2 % [Per10]. Extraction of the total beam intensity using these attenuators and a large NaI(Tl) detector is discussed in more detail in Section 4.1.1.

Relative Intensity Monitors

Because the absolute intensity measurements using the large NaI(Tl) detector require attenuation of the γ-ray beam, they could not be performed concurrently with the experiment. In order to extract an absolute cross section, the intensity of the beam must be measured in real-time with the experiment to give the total integrated luminosity. Relative intensity measurements do not require the beam to be attenuated, and several different relative intensity monitors were used in order to cross-check each relative measurement and control systematic uncertainties. Each relative intensity monitor was calibrated against the absolute intensity measured by the NaI(Tl) detector and then run simultaneously with the experiment, providing the normalization necessary for measuring absolute cross sections. Calibration of the relative intensity monitors and extraction of the total integrated luminosity on target are discussed in Section 4.1.1.

Paddles: Upstream of the target room are two thin BC400 plastic scintillating paddles coupled to photomultiplier tubes (PMTs). When a photon from the beam deposits energy in one of the paddles, the scintillating plastic produces a flash of light and a pulse from the PMT is recorded. Typically, one interaction occurs for every thousand incident photons. Each paddle provided an independent relative intensity measurement and was independently calibrated against the absolute intensity measurements using the large NaI(Tl) detector.

Heavy Water Cell: A small polyethylene cell filled with heavy water is located at the downstream end of the target room. The cell is 47.4 mm long, 40.8 mm in diameter, and has 0.7 mm thick walls. Neutrons from the photodisintegration of deuterons in the heavy water were detected by two Bicron BC-501A scintillating neutron detectors, placed 48 cm from the cell at a scattering angle of 90°. Although an absolute intensity measurement is possible using this setup [Sta08], the uncertainties in neutron detector efficiencies and scattering of neutrons inside the cell cause a 15–20 % systematic uncertainty in beam intensity. For this experiment, smaller uncertainties in the total integrated luminosity were found by using the heavy water cell as a relative counter and relying on the absolute measurements of the attenuated beam using the large NaI(Tl) detector.

3.2.2 Energy

The energy profile of the γ-ray beam was measured with a large 123 % high-purity germanium (HPGe) detector placed directly in the beam. Like the NaI(Tl) detector, the HPGe detector is useful only at count rates below a few kHz, so the beam intensity was reduced using the attenuators previously described in the Section 3.2.1 while making energy measurements. For the γ-ray beam energies used in this experiment,

a significant portion of the events recorded in the HPGe detector do not deposit their full energy in the detector due to Compton scattering and pair production. A Monte Carlo algorithm developed by Sun *et al.* [Sun09b] was used to reconstruct spectra from the HPGe detector and is discussed in more detail in Section 4.1.2. During later runs, a 3 in thick segmented NaI(Tl) annulus was placed around the HPGe detector to detect and measure radiation leaving the detector, greatly simplifying the analysis.

3.3 Optical Time Projection Chamber

The optical time projection chamber (OTPC) used in this work consists of a parallel-grid drift chamber or time projection chamber (TPC) along with an optical readout system to record photographs of the ionization tracks. This concept was first developed for imaging Čerenkov rings from high energy electrons by Charpack *et al.* [Cha78, Bre79], and the first OTPC capable of imaging charged-particle tracks was developed by Potter [Pot84]. The basic design was then extensively developed by Charpak *et al.* [Cha87]. Subsequently, Miernik *et al.* used a charge-particle detecting OTPC which they designed and built [Mie07a] to perform the first successful nuclear physics experiment involving this type of detector: a measurement of the two-proton decay of ^{45}Fe [Mie07b].

The HIγS OTPC was designed to measure cross sections and angular distributions of outgoing charged particles from photodisintegration reactions induced by the γ-ray beams available at HIγS [Gai10]. The overall layout of the detector is shown in Figure 3.5.

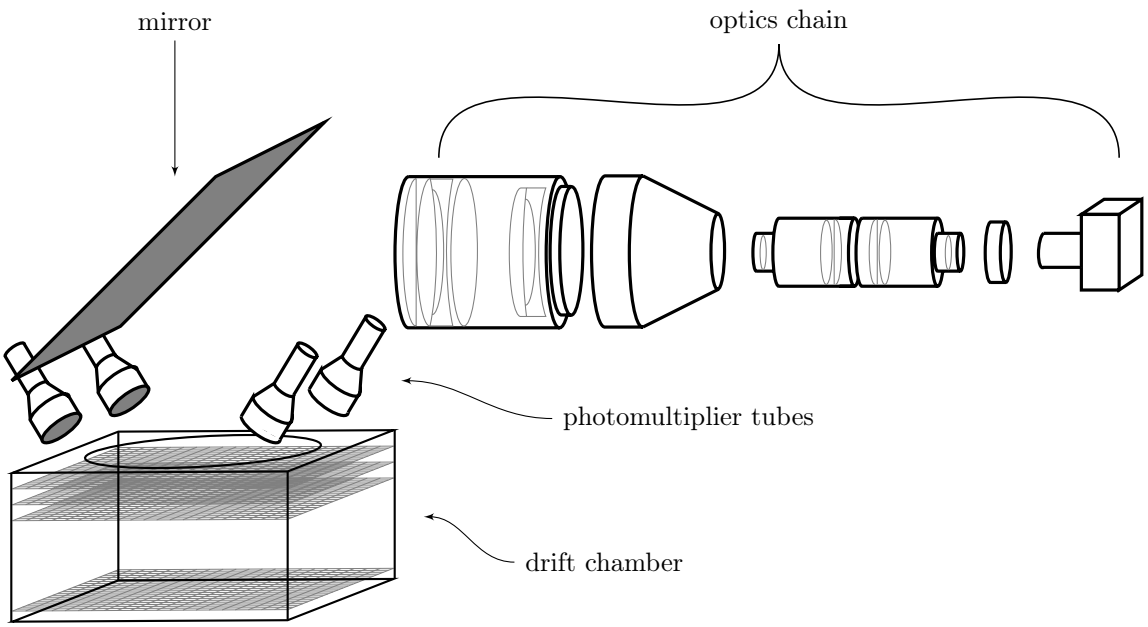

Figure 3.5: The HIγS OTPC showing the drift chamber, photomultiplier tubes, mirror and the optics chain.

3.3.1 Drift Chamber

The drift chamber, shown in Figure 3.6, is 30 cm long, 30 cm wide, and 21 cm tall. Inside the drift chamber are four high-voltage grids acting as electrodes to generate an electric field. Each of the grids is made from a mesh of 50 µm thick stainless steel wires spaced 500 µm apart from one another. The walls of the drift chamber between the anode and cathode grids are covered with 66 parallel copper strips, 2.5 mm wide with 0.4 mm spacing. The copper strips are connected to each other and to the grids with 1 MΩ resistors, establishing a homogeneous electric field inside the drift chamber.

The drift chamber is filled with a mixture of 80 % CO_2 target gas and 20 % N_2 scintillator. The CO_2 provides the target ^{12}C nuclei, while the N_2 was chosen as a scintillator to maximize light output at an acceptable wavelength [Wei06]. Most of the scintillation light from N_2 is emitted at 337 nm, but a significant amount is emitted

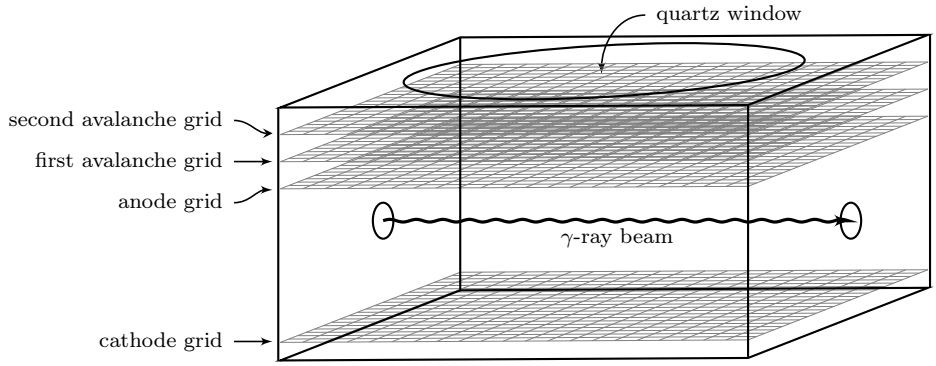

Figure 3.6: The drift chamber is filled with gas containing ^{12}C (CO_2). The γ-ray beam causes photodisintegration events in the gas, and the recoiling charged particles leave behind ionization tracks. Electrons from the ionization drift toward the anode grid. An avalanche is induced by the strong electric field between the avalanche grids, and scintillation light passes through the quartz window.

at the longer, near-visible wavelengths of 377 nm and 391 nm. The gas is kept at a pressure of 100 torr or 150 torr depending on the beam energy in order to optimize the length of the charged particle tracks. In order to maintain purity, continuous gas flow through the drift chamber is maintained at 100–200 std cm^3/min[1].

Table 3.1: Drift chamber grid operation voltages and calculated electric field strengths between the grids.

	Voltage (kV)		Field Strength (kV/cm)	
Grid / Region	100 torr	150 torr	100 torr	150 torr
cathode grid	−3.50	−4.50		
anode grid	0	0		
first avalanche grid	2.00	2.00		
second avalanche grid	5.18	6.28		
cathode-anode			0.168	0.216
anode-first avalanche			4.00	4.00
first-second avalanche			10.4	12.6

The γ-ray beam enters and exits the OTPC through 1 mm thick aluminum windows. The entrance and exit windows are mounted at the end of beam pipes 64 cm

[1]std cm^3 is defined as one cm^3 of gas at standard temperature and pressure (STP).

and 70 cm away from the drift chamber, respectively, to prevent any charged particles produced by the interaction between the beam and the windows from reaching the drift chamber. Additionally, a large permanent magnet is mounted immediately downstream of the entrance window to deflect electrons and positrons away from the drift chamber. Photodisintegration events are induced in the target gas, and the recoiling charged particles leave ionization tracks in the gas. Electrons from the ionization drift upwards toward the anode grid. The strong electric field between the anode grid and the two avalanche grids causes a cascade of ionization and electron multiplication. Operating voltages of the grids and the calculated electric field strengths between them are listed in Table 3.1.

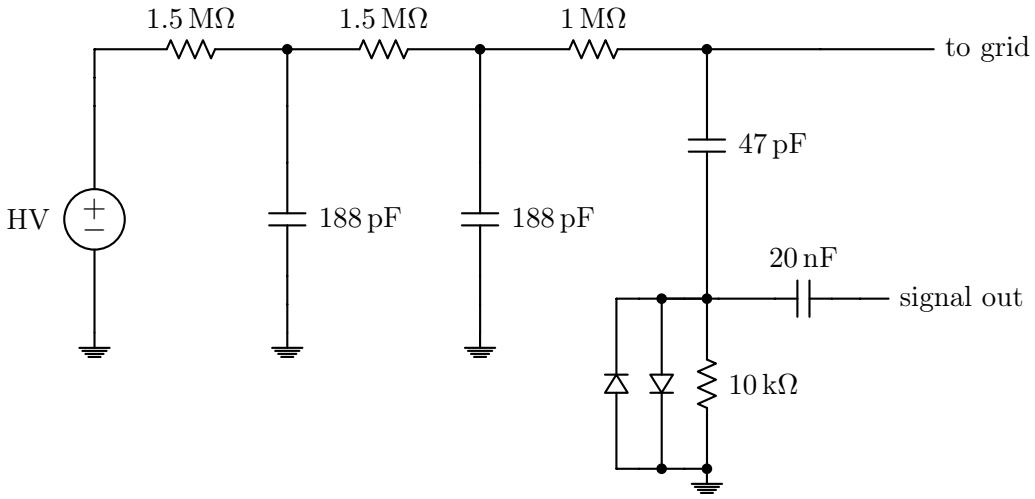

Figure 3.7: Circuit for extracting a signal from the high-voltage grid inside the drift chamber. The high voltage from the power supply is sent through a low-pass filter to the grid to reduce noise. High frequency signals from the grid are extracted, and a protection circuit keeps large voltage spikes from propagating.

The electron avalanche induces a signal in the second avalanche grid which is read out after passing through the circuit shown in Figure 3.7. The avalanche also causes scintillation in the N_2 gas, and the emitted light leaves the drift chamber through a 2.5 cm thick, 40 cm diameter quartz window and is detected by four Hamamatsu

R10133 photomultiplier tubes (PMTs) mounted around the window, as shown in Figure 3.5, and two additional PMTs (not pictured) mounted on either side of the optics chain. The signals from the PMTs are digitized to form the time projection signals which give kinematic information about the track used to reconstruct the event.

3.3.2 Optics Chain

Images of the charged particle tracks produced by the scintillation of the N_2 gas are recorded by the optics chain, shown in Figure 3.8. The optics chain is based on the opto-electronics readout system of the CERN Hybrid Oscillation Research Apparatus (CHORUS) neutrino oscillation experiment [Esk98], and many of the components come directly from one of the CHORUS intensifier chains [Ann98]. The optics chain consists of the main lens assembly, an electrostatic demagnifier, the auxiliary lens assembly, a gated image intensifier, and finally a computer-controlled camera to record a photograph of the event.

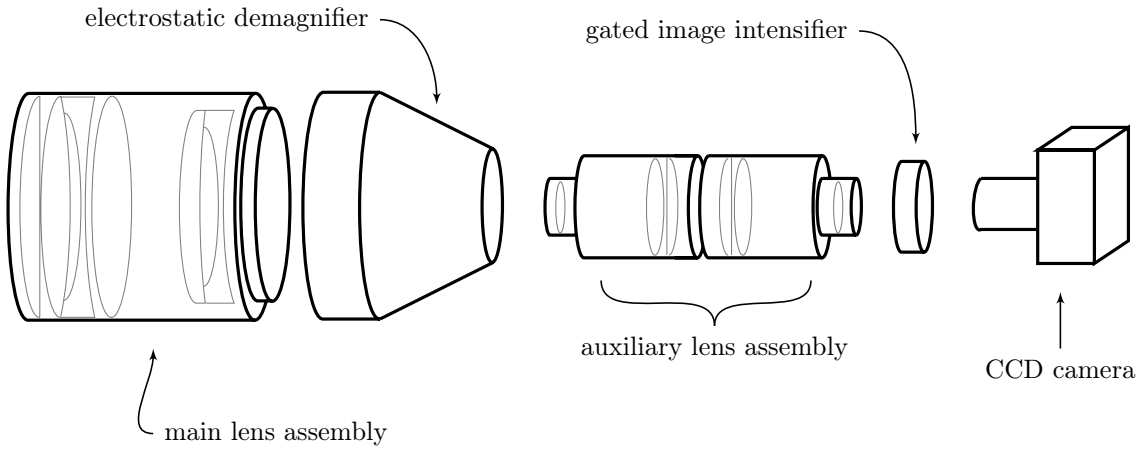

Figure 3.8: The optics chain records an image of each event.

The main lens assembly (MLA) gathers and focuses the scintillation light from the

tracks onto the electrostatic demagnifier. The MLA is 142 mm in diameter and has an f-number of f/1.4 . The face of the MLA is 635 mm from the second avalanche grid and has a field of view 370 mm in diameter. The MLA was custom designed for this system by Optical Engineering [Arn] and was fabricated by Optimax Systems [Opt].

The image projected by the MLA falls onto a Hamamatsu model V4440U electrostatic demagnifier taken from one of the CHORUS intensifier chains. On the face of the demagnifier is a 100 mm diameter photocathode, and emitted photoelectrons are focused onto a P11 phosphor 25 mm in diameter at the back of the demagnifier. P11 is a slow phosphor with a 50 µs decay time. This allows time for the gated image intensifier and camera to be triggered by a signal generated from the second avalanche grid without losing much light. The demagnifier has a quantum efficiency of 18 % and intensifies the light with a gain of 126, both measured at a wavelength of 430 nm [Ann98].

The back of the demagnifier is viewed by the auxiliary lens assembly (ALA) which consists of two 50 mm focal length Nikon AF Nikkor camera lenses. The fronts of the two lenses are mounted facing each other so that the image from the demagnifier is projected onto the 25 mm diameter photocathode of the gated image intensifier mounted 50 mm behind the ALA.

The gated image intensifier is taken from one of the CHORUS intensifier chains and consists of a photocathode, a micro-channel plate (MCP), and a P46 phosphor at the back. It has a quantum efficiency of 11 % and a gain of up to 800 at a wavelength of 520 nm [Ann98]. The photocathode of the intensifier is normally biased at 50 V, preventing any photoelectrons from being emitted. A trigger signal from a photodisintegration event (Figure 3.10) switches the bias to −200 V which allows photoelectrons to be emitted by the photocathode, multiplied by the MCP, and collected by the phosphor screen. This gate is open for 50 µs, which allows for the collection of

most of the light emitted by the demagnifier while greatly reducing background light not associated with a photodisintegration event.

The track image appearing on the phosphor screen of the image intensifier is photographed by a Hamamatsu model C10600-10B-H ORCA-R2 camera with a Sigma 50 mm f/2.8 macro lens. The hermetic vacuum-sealed CCD sensor in the camera is cooled to $-35\,^{\circ}\mathrm{C}$ with forced air flowing over a Peltier junction. The camera is capable of recording images at a resolution of 1344×1024 pixels, each read out with a 16 bit digitizer depth. In order to increase the maximum frame rate and reduce the dead time, the pixels are binned before being digitized, and the camera is read out at a reduced resolution of 672×512 pixels and a reduced 12 bit digitizer depth. At this reduced resolution and depth the camera has a maximum frame rate of 28.4 frames/s. The frame rate of the camera is the limiting factor for the total dead time of the detector, even at the reduced resolution. In order to keep the dead time less than 25 %, the maximum event rate is limited to less than 6 Hz.

3.4 Electronics

The electronics setup of the HIγS OTPC consists of three main circuits: (i) the trigger circuit starts the data acquisition system when an event deposits sufficient energy in the drift chamber, (ii) the optics circuit sends triggers to the various components of the optics chain and records the output from the PMTs, and (iii) the busy circuit ensures that no new event can be triggered while the data acquisition and optics chain are processing a previous event. All of the NIM [NIM64] and VME [VME87] modules used in the electronics setup are listed in Table 3.2.

Table 3.2: NIM and VME electronics modules used in the HIγS OTPC.

Module	Make/Model	Crate	Figures
spectroscopy amplifier	Ortec 452	NIM	3.9
timing filtering amplifier	Ortec 474	NIM	3.9
constant fraction discriminator	Phillips Scientific 406	NIM	3.9
gate generator	LeCroy 222	NIM	3.9
coincidence logic unit	Phillips Scientific 755	NIM	3.9, 3.11
logic fan	LeCroy 492A	NIM	3.11
gate & delay generator	Phillips Scientific 794	NIM	3.9, 3.10, 3.11
level translator	Phillips Scientific 726	NIM	3.10, 3.11
random pulse generator	BNC DB-2	NIM	3.11
peak-sensing ADC	CAEN V785	VME	3.9, 3.11
scalers module	Struck SIS3800	VME	3.9
FADC digitizer	Struck SIS3300	VME	3.10
VME trigger	Struck SIS3610	VME	3.10, 3.11

3.4.1 Trigger Circuit

The trigger circuit, shown in Figure 3.9, takes the signal from the last multiplication grid (Figure 3.7), pre-amplifies it, and splits it into a linear branch and a logic branch using a standard BNC tee connector. The linear branch is resistively attenuated by a factor of 8 in order to avoid saturation and then shaped using a spectroscopy amplifier with a shaping time of 6 µs. The unipolar output from the spectroscopy amplifier is fed into a 12 bit peak-sensing analog-to-digital converter (ADC) which records the pulse height. The logic branch is shaped by a timing filtering amplifier (TFA) and then sent to a constant fraction discriminator (CFD). The use of a CFD provides a trigger signal with stable timing independent of pulse height. The output signal from the CFD starts a gate generator. The 75 µs gate is sent to a logic unit which is used as the trigger OR. One output from the trigger OR goes to a VME-based [VME87] scaler module which records the total number of trigger signals. The other output from the trigger OR goes to another logic unit which is used as the trigger veto OR. This unit will inhibit any trigger signal output when

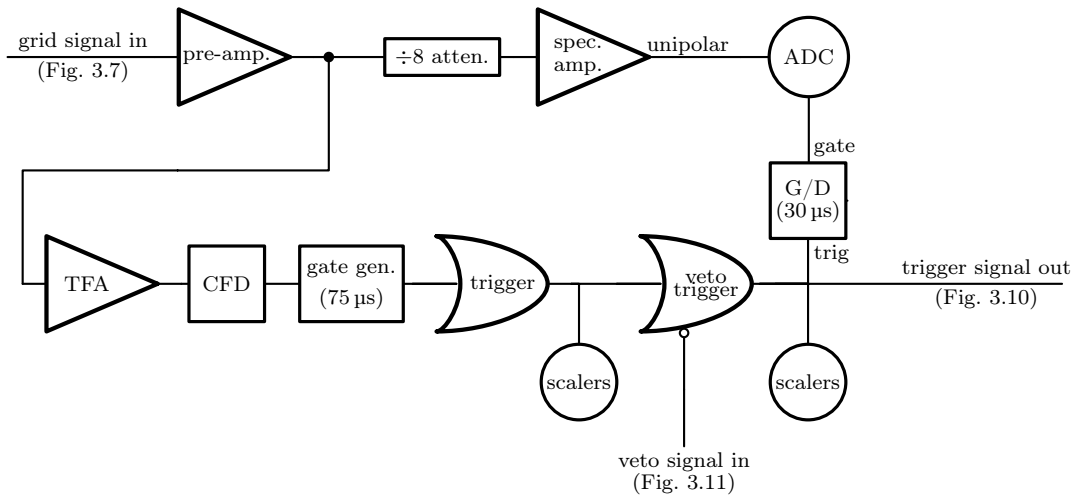

Figure 3.9: The trigger circuit creates a master trigger from the grid signal and reads the grid signal into an ADC.

the DAQ is busy by using the veto signal generated by the busy circuit, shown in Figure 3.11. One output from the veto trigger OR is sent to the scaler module, while another is sent to a gate and delay generator (G/D) with a 30 µs gate. This is used as the gate for the ADC; only pulses occurring within that window are digitized.

3.4.2 Optics Circuit

The optics circuit, shown in Figure 3.10, takes two copies of the master trigger signal generated by the trigger circuit (Figure 3.9). One copy of the master trigger signal is used to create a gate 1.2 µs wide and delayed by 7.5 µs using two channels of a gate and delay generator. This gate is used as the stop signal for a 100 MHz 12 bit flash ADC (FADC) VME module. The FADC constantly digitizes the time projection signals from the six PMTs, and when it receives a trigger, the previous 20 µs of digitized signals are recorded. Another copy of the trigger signal is sent to a separate channel of a gate and delay generator which generates a 50 µs master gate for the optics system. The NIM gate is sent to the busy circuit (Figure 3.11)

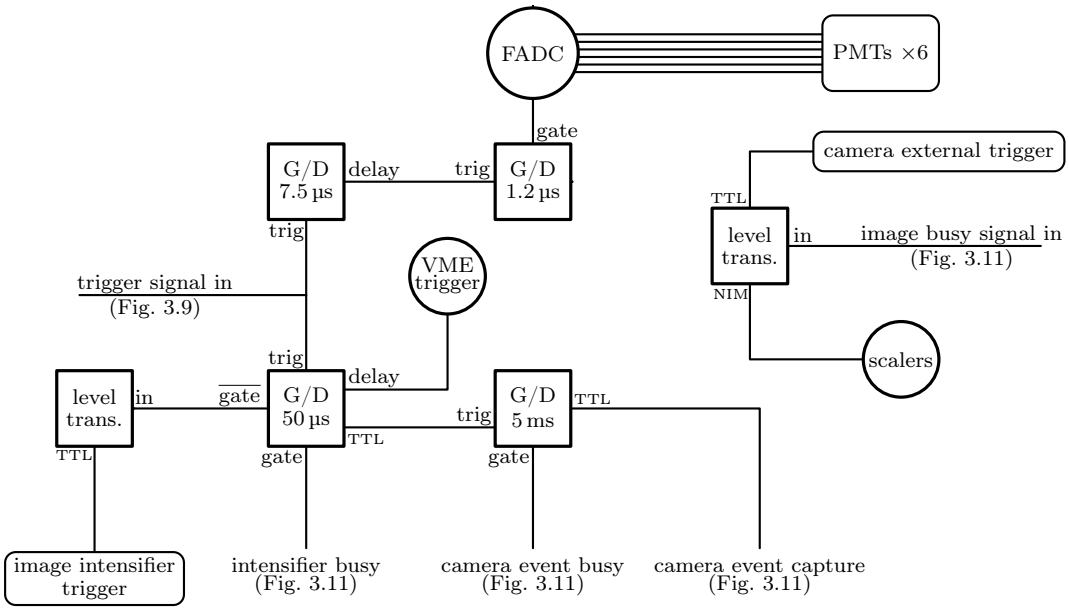

Figure 3.10: The HIγS OTPC optics circuit takes the previously-generated master trigger signal (Figure 3.9) and uses it to trigger the various optics systems.

as the 'camera event busy.' The NIM not-gate ($\overline{\text{gate}}$) is sent to a level translator, the TTL output of which is sent to trigger the internal power supply of the gated image intensifier, biasing its photocathode. The TTL output of the master optics gate triggers a new channel of a gate and delay generator, creating a 5 ms gate. The NIM and TTL outputs of this gate go to the busy circuit (Figure 3.11) as the 'camera event busy' and 'camera event capture' signals respectively. The delay output of the master optics gate is sent to trigger the VME trigger module. In order to trigger the camera, the 'image busy' signal from the busy circuit (Figure 3.11) goes through a level translator, and the TTL output is sent to the 'external trigger' input of the camera. The NIM output of the level translator is sent to the VME scaler module to record the total number of images captured.

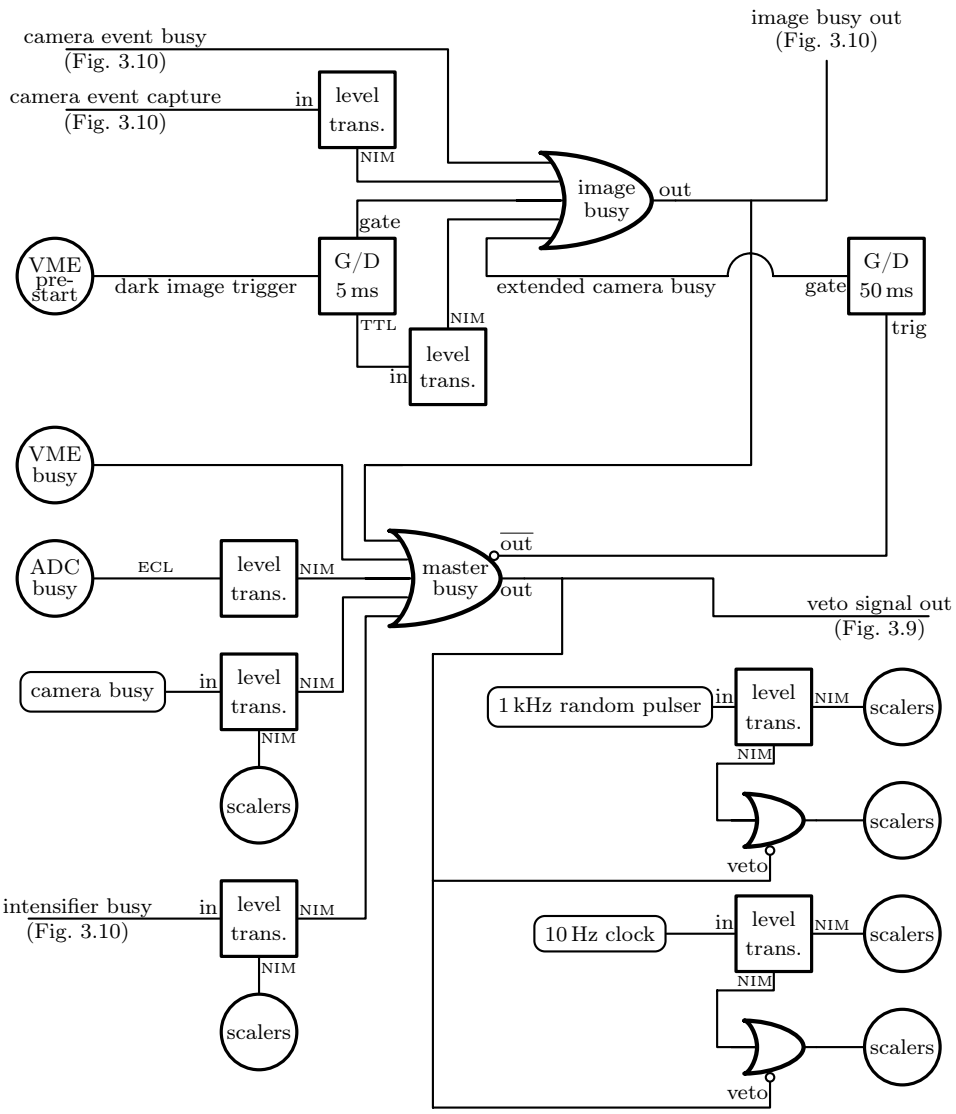

Figure 3.11: The HIγS OTPC busy circuit creates busy signals to prevent the optics system or the DAQ from triggering while a previous event is being processed.

3.4.3 Busy Circuit

Because the HIγS OTPC records data from both a camera and from VME-based modules, many redundant busy signals are latched to ensure that no part of the DAQ can be triggered while processing a previous event. The busy circuit creates two separate busy signals: the image busy and the master busy. Both busy signals are generated using logic fans as OR gates.

The inputs to the image busy OR gate include signals from the optics circuit (Figure 3.10), a signal from the VME trigger module to latch a busy while the camera captures a dark image at the beginning of each run, and the 'extended camera busy' signal from the master busy OR.

The various inputs are generated using gate and delay generators and level translators. Outputs from the image busy OR gate are sent to the optics circuit to trigger the camera (Figure 3.10) and as an input to the master busy OR.

The inputs to the master busy OR gate are the output from the image busy, the previously-generated intensifier busy (Figure 3.10), busy signals from the ADC and VME trigger module, and the camera busy signal from the input/output port of the camera control unit. Since the camera busy signal taken from the input/output port does not extend the full time needed for the camera to download the image, the not-out ($\overline{\text{out}}$) from the master busy OR gate is used to generate a 50 ms gate as the 'extended camera busy' signal which is sent as an input back to the image busy OR gate. Outputs from the master busy OR gate are sent to the trigger circuit (Figure 3.9), and used as veto signals for the scaler inputs from a 1 kHz random pulser and a 10 Hz clock. The total live time of the DAQ can be determined by comparing the total number of scaler inputs from the random pulser or clock to the vetoed versions of the same signals.

3.5 Data Acquisition

The data acquisition (DAQ) system records all relevant physics information from the HIγS OTPC. The camera images and the readouts from the ADC and FADC are recorded for each event, while a dark image from the camera and scaler information are recorded for each run.

3.5.1 CODA

All the VME-based modules in the DAQ system are controlled and read out by the CEBAF Online Data Acquisition (CODA) software tool-kit [Abb99], developed for nuclear physics experiments at Thomas Jefferson National Accelerator Facility. CODA uses a Linux workstation as a host computer and a VME-based PowerPC single-board computer (SBC) running VxWorks [Win09] to control the various digitizers.

When the VME trigger module receives a trigger (Figure 3.10), it causes the read-out control (ROC) process running on the SBC to take the digitized signals from the ADC, FADC, and scaler module, and store them in a local buffer. Data in the buffer are sent over Ethernet to the event builder (EB) process running on the host computer. The EB process parses the event data and writes them to disk for later analysis. During this process, busy signals from the ADC, FADC, and VME trigger module prevent another trigger until each module can accept another event.

3.5.2 Camera

The Hamamatsu camera uses proprietary drivers, and an application programming interface (API) provided by Hamamatsu was used to write custom software for the camera. Because the API grants only limited control over the camera, it could not be directly integrated into CODA. A separate Windows computer was used to control and record images from the camera.

When CODA initiates the pre-start routine, a dark image is recorded for background subtraction. Once the run begins, a physics event causes a trigger signal to be sent to the camera (Figure 3.10), and it records a 672×512 pixel, 12 bit image and sends it via an IEEE 1394 interface [IEE08] to the Windows computer. The computer stores the images in a virtual hard drive made up of 4 GB of random access memory (RAM).

Every sixty seconds a background process transfers the images from the RAM drive to a 5 TB redundant array of independent disks (RAID) for permanent storage. At an event rate of 4 Hz, 9.2 GB of images are recorded every hour of running. In order to ensure the images from the camera are properly matched to events from the digitizers, the camera control software increments the image file name after each event. Because the camera control software is never synchronized directly with `CODA`, an erroneous trigger received either by `CODA` or by the camera causes the event numbering to go out of sync, and the images can no longer be matched to event data from the digitizers. Since this mismatch makes analysis of the data extremely difficult, many redundant busy signals are used (Figure 3.11) to prevent erroneous triggers. However, the time taken by the camera to transfer the image is not always predictable, and the 50 ms 'extended camera busy' signal does not always cover the full time that the camera is in fact busy. This causes occasional (one event per 100,000) mismatches when running at high rates (>6 Hz).

Chapter 4

Data Reduction & Analysis

The offline analysis in this experiment was performed using the ROOT framework for large scale data analysis [Bru97]. ROOT provides C++ libraries with classes written for the analysis of data from nuclear and particle physics experiments. Apart from the images, all of the data taken during the experiment were recorded by the CODA data acquisition software (see Section 3.5). Binary event data files written by CODA were converted to a ROOT-based file format using the TUNL Real-time Analysis Package (TRAP) software.

4.1 Beam Diagnostics

4.1.1 Intensity

As described in Section 3.2.1, the γ-ray beam intensity was measured using several real-time relative monitors, each calibrated against absolute measurements made using a large NaI(Tl) detector placed directly in the beam.

Absolute Intensity

An absolute intensity measurement was taken with the NaI(Tl) detector directly in the attenuated beam, at least twice during the runs at each beam energy. Because the NaI(Tl) detector could not operate under the full intensity of the γ-ray beam, precision attenuators reduced the intensity while this detector was used (see Section 3.2.1). A typical spectrum is shown in Figure 4.1. The response function of

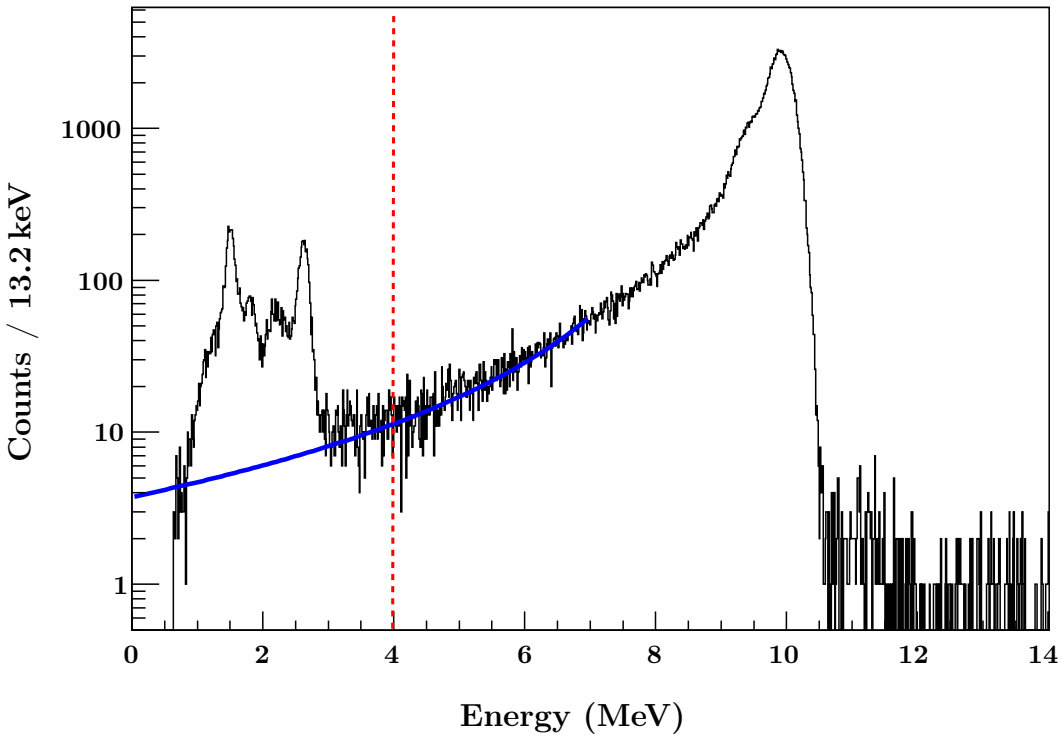

Figure 4.1: Spectrum from the NaI(Tl) detector, placed directly in the 10.1 MeV γ-ray beam. The contribution from events depositing less than 4 MeV in the detector was estimated by fitting the tail of the peak with a Lorentzian line shape (solid blue line) and extrapolating below the dotted red line.

the NaI(Tl) detector is such that the photoabsorption peak, the escape peaks, and the Compton edge all overlap with a low-energy tail reaching down to the natural background lines from ^{208}Tl and ^{40}K at 2615 keV and 1462 keV, respectively. The total number of beam-related events in each NaI(Tl) spectrum was estimated by summing the counts above a cutoff energy (typically 4 MeV), and adding to it the contribution from beam-related events occurring below the cutoff energy, estimated by fitting the low-energy tail of the distribution to a Lorentzian function and extrapolating to zero energy. Corrections were made for the efficiency of the detector and the attenuation due to the aluminum entrance window of the NaI(Tl) detector as well as the aluminum entrance and exit windows of the OTPC. Corrections due to

dead time from the electronics were not necessary, as the total number of counts was taken from the scalers. The dead time from the detector itself can be estimated to be less than 0.04 % from the decay time of a pulse from the detector (≈ 200 ns) and the maximum rate at which the detector was operated (2 kHz). The absolute beam intensity was calculated by using the published attenuation factors [Ber98] of the copper attenuators. On-target γ-ray beam intensities were typically 1–2 $\times 10^8$ γ/s.

Relative Intensity

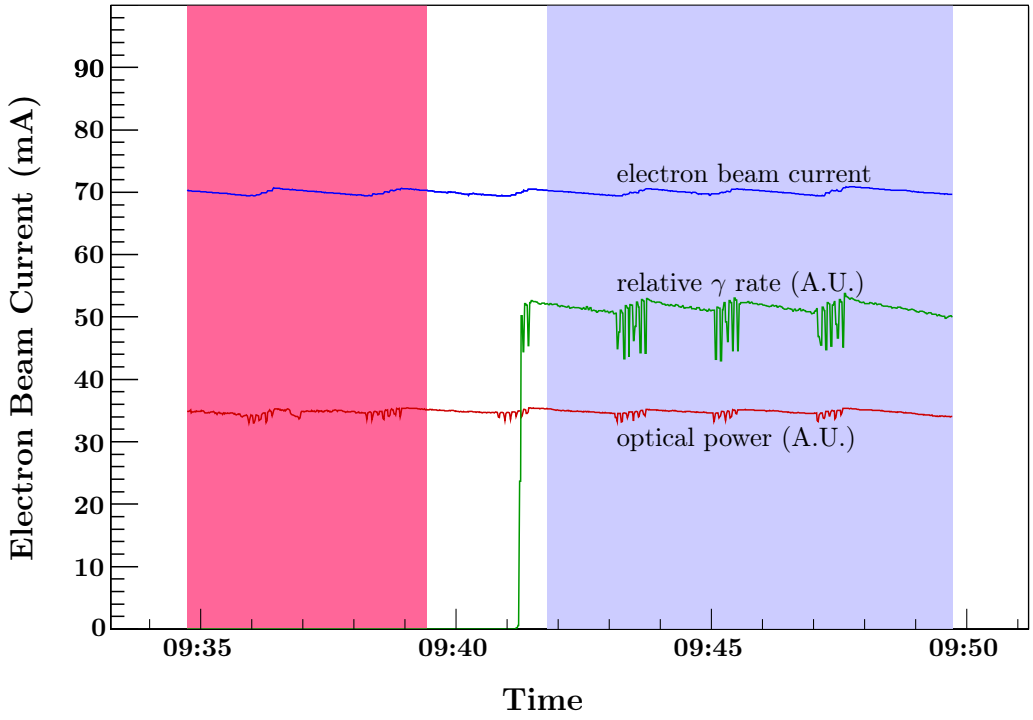

Figure 4.2: Calibration of the real-time relative intensity monitors. The pink box shows the time in which absolute intensity was measured, and the blue box shows the time of the relative measurement. The two measurements were performed close together in time, during which the beam conditions were stable. Small variations in beam intensity between the absolute and relative intensity measurements were estimated by using the electron beam current times the FEL optical power to weight the two measurements.

Because the NaI(Tl) detector could not be exposed to the unattenuated γ-ray

beam, several relative counters were used to monitor the beam intensity in real time (see Section 3.2.1). Each of the relative counters was calibrated by taking an absolute intensity measurement and a relative intensity measurement in quick succession, assuming the beam to be relatively stable over the two measurements. Corrections for variations in beam intensity were made by weighting each intensity measurement using the integrated product of the electron beam current and the FEL optical power, which is proportional to the beam intensity. The current and optical power were measured once per second from the HIγS accelerator control system and integrated over each intensity measurement. These corrections were typically less than 2 %. Figure 4.2 shows a typical calibration of the relative counters, which was performed at least twice during the runs at each γ-ray beam energy.

4.1.2 Energy

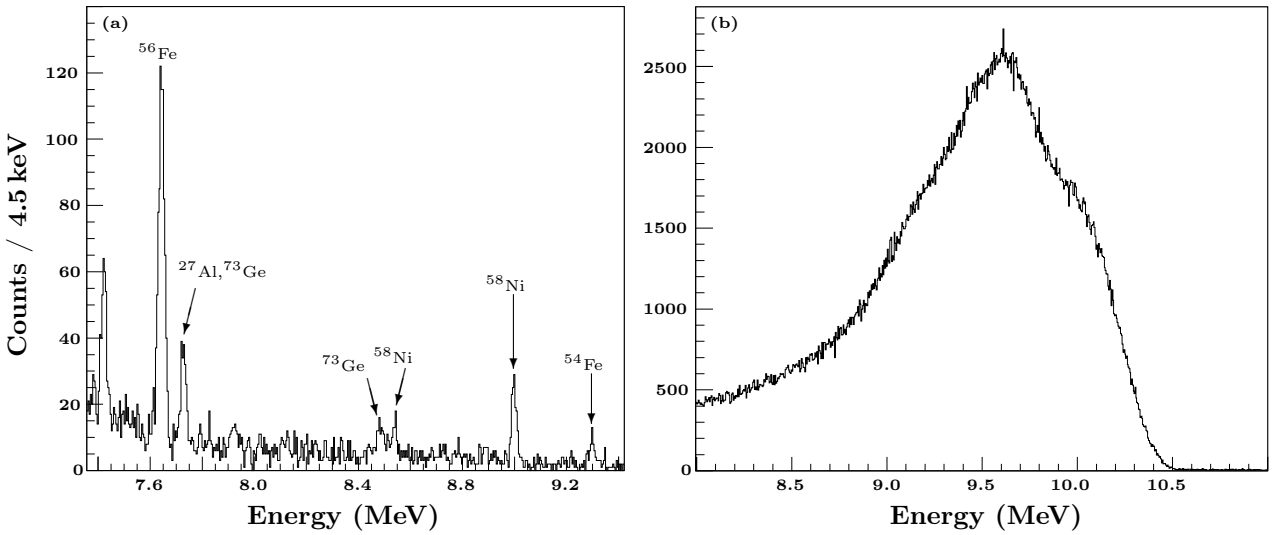

Figure 4.3: (a) Calibration HPGe spectrum using γ-ray lines from thermal neutron capture with a ^{58}Ni target. (b) HPGe spectrum taken with the detector directly in the attenuated beam. The photoabsorption peak overlaps with the first and second escape peaks and their respective Compton edges.

As described in Section 3.2.2, the energy distribution of the γ-ray beam was measured using a HPGe detector placed directly in the attenuated beam. The detector has an energy resolution of approximately 4 keV and was calibrated using the γ-ray lines from thermal neutron capture on a ^{58}Ni target as shown in Figure 4.3a. The γ-ray lines used for calibration are listed in Table 4.1 and include the lines from the ^{58}Ni target as well as from other nuclei present in the target room.

Table 4.1: Published thermal neutron capture lines [Cha06] used for calibration of the HPGe detector.

E_γ (keV)	X(n,γ)
9297.80	^{54}Fe
8998.63	^{58}Ni
8553.71	^{58}Ni
8498.64	^{73}Ge
7729.90	^{73}Ge
7724.03	^{27}Al
7645.58	^{56}Fe
7631.18	^{56}Fe

Monte Carlo Unfolding

At the γ-ray beam energies used in this experiment, the photoabsorption peak in the HPGe detector was completely overwhelmed by contributions from the escape peaks and Compton scattering (see Figure 4.4). An algorithm developed by Sun *et al.* [Sun09b] was used to unfold the HPGe spectra and extract the γ-ray beam energy distributions.

In Sun's algorithm, the spectrum $m(E)$ recorded by the HPGe detector is described by

$$m(E) = \int_0^\infty dE_\gamma \; H(E, E_\gamma) f(E_\gamma), \tag{4.1}$$

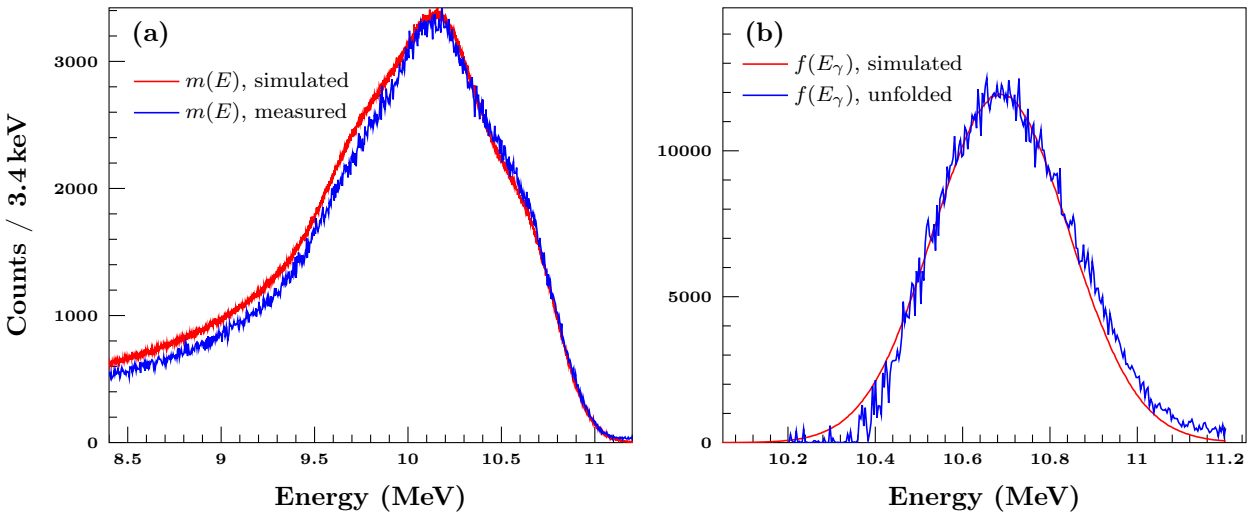

Figure 4.4: Unfolding of HPGe spectrum using the algorithm developed by Sun *et al.* [Sun09b]. (a) HPGe spectrum measured at a γ-ray beam energy of 10.7 MeV, along with the simulated HPGe spectrum. (b) Simulated γ-ray beam energy distribution along with the energy distribution measured by the HPGe detector and unfolded using Sun's algorithm.

where E_γ is the energy of the incident γ ray, E is the energy recorded by the HPGe detector, $f(E_\gamma)$ is the beam energy distribution and $H(E, E_\gamma)$ is the detector response function, which dependent on the spatial distribution of the γ-ray beam and detector. Equation 4.1 can be discretized:

$$\vec{m} = \mathbf{H}\vec{f}, \tag{4.2}$$

where $\mathbf{H}$ is the detector response matrix. For each HPGe spectrum, $\mathbf{H}$ was calculated using a Monte Carlo simulation of the Compton backscattering γ-ray beam production and interaction with the HPGe detector [Sun09a, Sun09b]. The calculation is based on the Gold iteration method [Ban97] which involves recursively simulating γ-ray spectra and detector response matrices until the simulated spectrum matches the one measured with the HPGe detector. Once the detector response matrix is calculated, it is inverted and used to unfold the measured spectrum. Figure 4.4 shows an

example of a measured and an unfolded HPGe spectrum. This Monte Carlo method for unfolding HPGe spectra was used only for the OTPC runs from November 2010, after which a NaI(Tl) annulus was installed around the HPGe detector in order to simplify the analysis.

NaI(Tl) Annulus

During runs taken in August of 2012, a 3 in thick NaI(Tl) annulus was mounted around the HPGe detector. The annulus greatly simplified the extraction of the γ-ray beam energy distribution by detecting photons escaping from the HPGe detector due to pair production and Compton scattering.

Figure 4.5 shows the same energy spectrum from the HPGe detector, using the annulus to help extract the γ-ray beam energy distribution. Three different methods were used: (i) summing the total energy deposited in the HPGe detector and annulus (Figure 4.5b), (ii) requiring that no energy was deposited in the annulus (Figure 4.5c), and (iii) requiring that 511 keV was deposited in the annulus (Figure 4.5d). In each case, the γ-ray beam energy distribution was extracted by fitting a Gaussian function to the high-energy side of each spectrum. The spectrum shown in Figure 4.5d represents the first escape peak only, so it was shifted by 511 keV in order to obtain the beam energy distribution.

4.2 Background Rejection

The HIγS OTPC recorded 10–100 background events for every ^{12}C(γ,α_0)^{8}Be event, depending on γ-ray beam energy and drift chamber gas pressure. These background events must be rejected in order to accurately determine the cross sections and angular distributions. The unique design of the HIγS OTPC allows for the re-

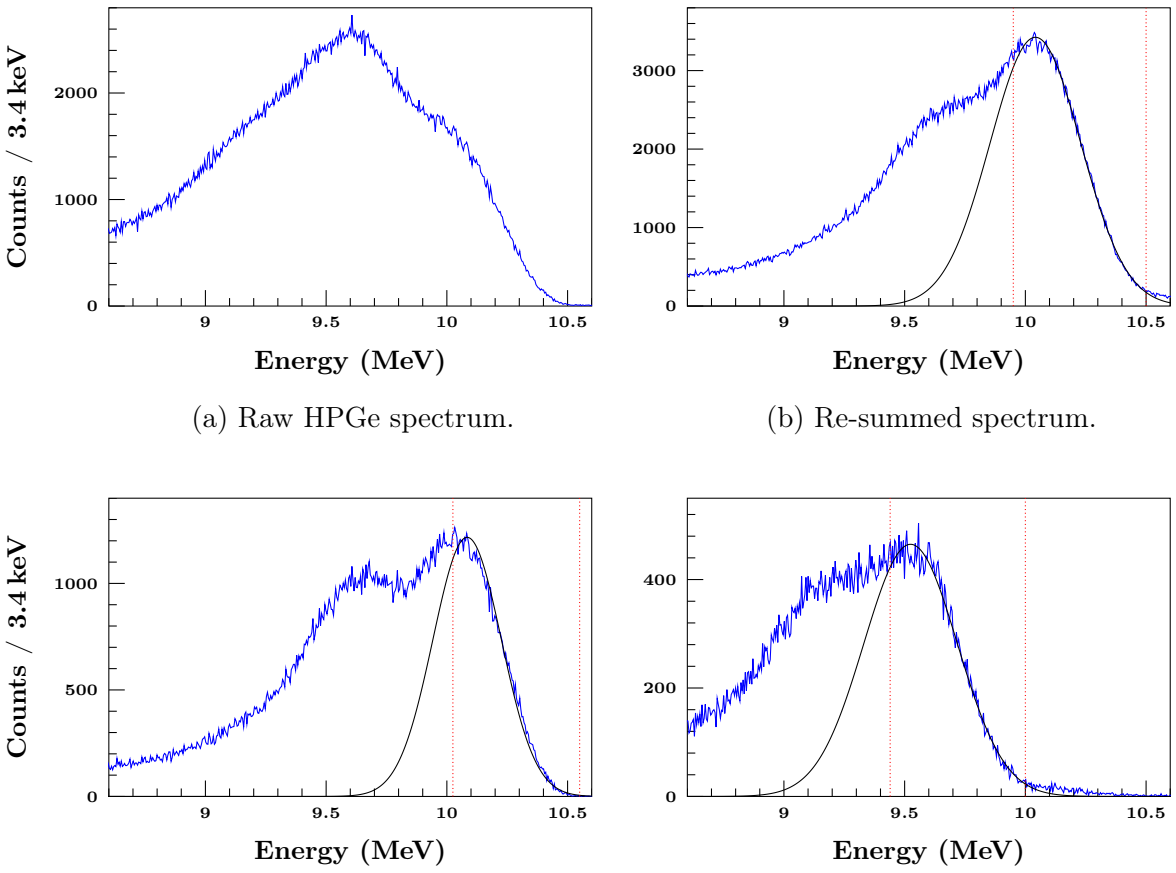

(a) Raw HPGe spectrum.

(b) Re-summed spectrum.

(c) Anti-coincidence spectrum.

(d) 511 keV coincidence spectrum.

Figure 4.5: HPGe spectra taken at a γ-ray beam energy of 10.1 MeV with the NaI(Tl) annulus. In each case, the γ-ray beam energy distribution was extracted by fitting a Gaussian function (solid black curves) to the high-energy side of each spectrum in the region defined by the dotted red lines.

jection of nearly all background events, leaving only ^{12}C(γ,α_0)^{8}Be events. This was accomplished in two stages: (i) separation of the raw events into (γ, α) events and non-(γ, α) background events (described in this section), and (ii) classification of the (γ, α) events into ^{12}C(γ,α_0)^{8}Be, ^{12}C(γ,α_1)^{8}Be*, ^{16}O(γ,α)^{12}C, and ^{18}O(γ,α)^{14}C events (described in Section 4.3.4).

An overview of the scheme for rejecting non-(γ, α) background events from the (γ, α) events is shown in Figure 4.7. The raw events are first filtered by the offline level-2 (L2) trigger (described in Section 4.2.2) which automatically rejects a majority

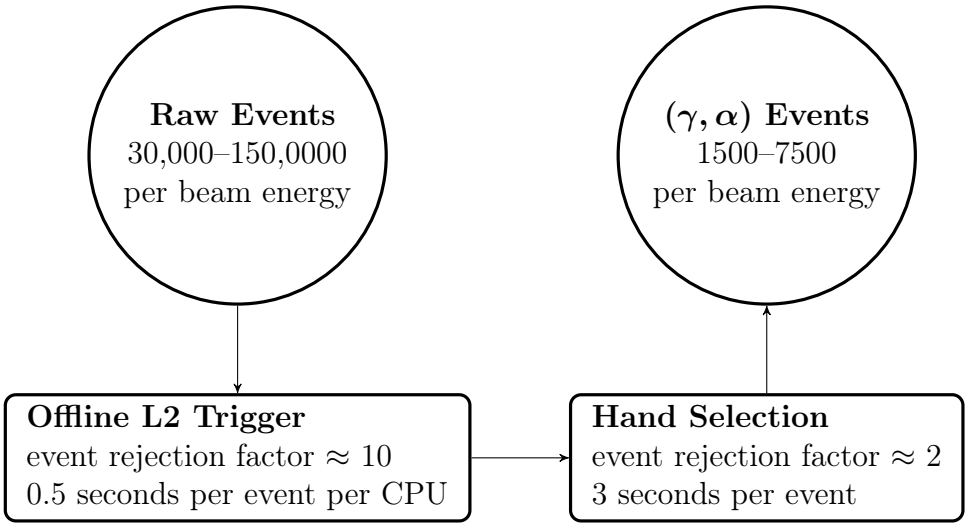

Figure 4.6: Background rejection schema. (γ, α) events are selected from the raw events by the offline L2 trigger and hand selection processes.

of the background events. The output events from the offline L2 trigger are sorted manually according to a process described in Section 4.2.3.

4.2.1 Event Types

Non-(γ, α) Background Events

Examples of photographs of tracks from background events are shown in Figure 4.7. Each type of background event is described below.

Cosmic Events: High energy cosmic rays can induce charged-particle tracks (Figure 4.7a) by interacting with the gas inside the drift chamber or with the components of the drift chamber. Cosmic events can be identified by the position and direction of the tracks (they do not originate from the beam), as well as from the length and stopping power of the tracks and the total charge deposited on the high voltage grids due to the high energy of the events. Cosmic events occur at a constant rate of $\approx 0.02\,\text{Hz}$, making up one event out every 50–250

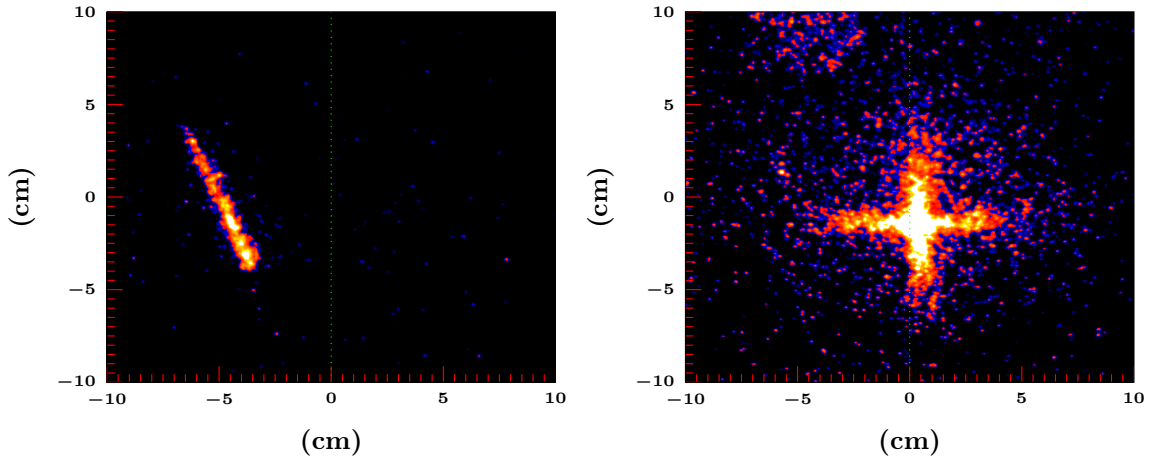

(a) Cosmic-ray induced charged particle event.

(b) Spark between high voltage grids. The cross shape is due to reflections off of the wire mesh of the high voltage grids.

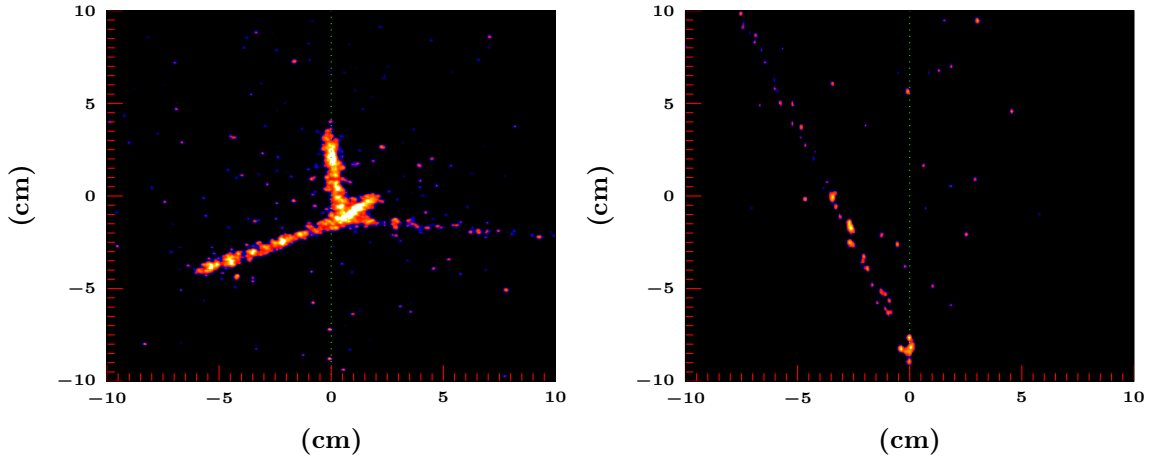

(c) Event induced by a bremsstrahlung γ ray.

(d) $^{14}\mathrm{N}(\gamma,p)^{13}\mathrm{C}$ event.

Figure 4.7: Background events recorded by the optics chain. The colors in the images represent the intensity of the light. The position of the beam is shown by the dotted green lines.

events recorded.

Sparks: Sparks between the high voltage grids inside the drift chamber can occur when the charge density on the avalanche grids is greater than the Raether limit [Rae64], causing a breakdown in the gas which allows current to flow

between the high-voltage grids. Sparks cause large amounts of scintillation light (Figure 4.7b). Some sparks may be caused by the electron avalanches resulting from (γ, α) events, but in this case all information from the event is lost. The sparking rate is highly dependent on the voltage between the grids and the gas pressure, and sparks make up 0.1–10 % of all events. Corrections made due to sparking are discussed in Section 4.4.3.

Bremsstrahlung γ Rays: A very small amount of bremsstrahlung γ rays are produced when the electron beam ($\approx 500\,\mathrm{MeV}$) interacts with residual gas inside the storage ring, and some of the bremsstrahlung photons have significantly higher energy than the primary γ-ray beam. When these high-energy photons interact with gas inside the OTPC they can cause photodisintegration reactions (Figure 4.7c) with much more energy than those caused by the primary γ-ray beam. These bremsstrahlung events are likely due to photons with energies near the giant dipole resonance of the nuclei in the target, where the photodisintegration cross section is large. These events induced by high-energy bremsstrahlung γ rays can be identified by the large amount of charge deposited on the high voltage grids and by the multiplicity and length of the tracks. High-energy bremsstrahlung events are very rare; there is only one high-energy bremsstrahlung event recorded for every several thousand total events. The effect of the low-energy portion of the bremsstrahlung spectrum is likely to be extremely small. Previous measurements of the HIγS bremsstrahlung spectrum [Sch00] gave an upper limit of one bremsstrahlung photon for every 10^5 photons in the primary beam. Furthermore, the measured beam energy spectra (see Section 4.1.2) do not show any bremsstrahlung component in the energy region of the primary γ-ray beam.

^{14}N(γ,p)^{13}C: Protons from the ^{14}N(γ,p)^{13}C reaction are produced when the beam interacts with the N_2 scintillation gas (Figure 4.7d). These events can be identified by the long tracks with low scintillation light density from the small stopping power characteristic of protons. The γ-ray beam energies used in this experiment correspond to proton energies of 2–3 MeV. Frequently, the proton leaves the active volume of the detector before depositing its full energy. For the runs at most beam energies, these comprise 60–95 % of the events recorded by the HIγS OTPC.

(γ, α) Events

Examples of photographs of tracks from (γ, α) events are shown in Figure 4.8. Each type of (γ, α) event is described below.

^{12}C(γ,α_0)^{8}Be: Photodisintegration events in which a ^{12}C nucleus is broken into an α particle and a ground-state ^{8}Be nucleus are the main events of interest for this experiment. The ^{8}Be nucleus decays into two α particles with a mean lifetime of 6.7×10^{-17} s. Because the reaction proceeds through the ground state of ^{8}Be, the energy of the first outgoing α particle (1.2–2.5 MeV) is completely determined by the energy of the beam. The ^{8}Be nucleus subsequently decays in flight into two α particles (0.6–1.4 MeV combined energy), both colinear with the third α particle (see Figure 4.8a).

^{12}C(γ,α_1)^{8}Be*: ^{12}C photodisintegration events can also proceed through the broad first excited state of ^{8}Be. This $J^{\pi} = 2^{+}$ state has an excitation energy of 3.03 MeV with a width of 1.513 MeV. The breadth of this state leads to three outgoing α particles which can take a range of energies and angles, similar to a three-body decay. The recorded ^{12}C(γ,α)^{8}Be events are made up of 1–6 % of

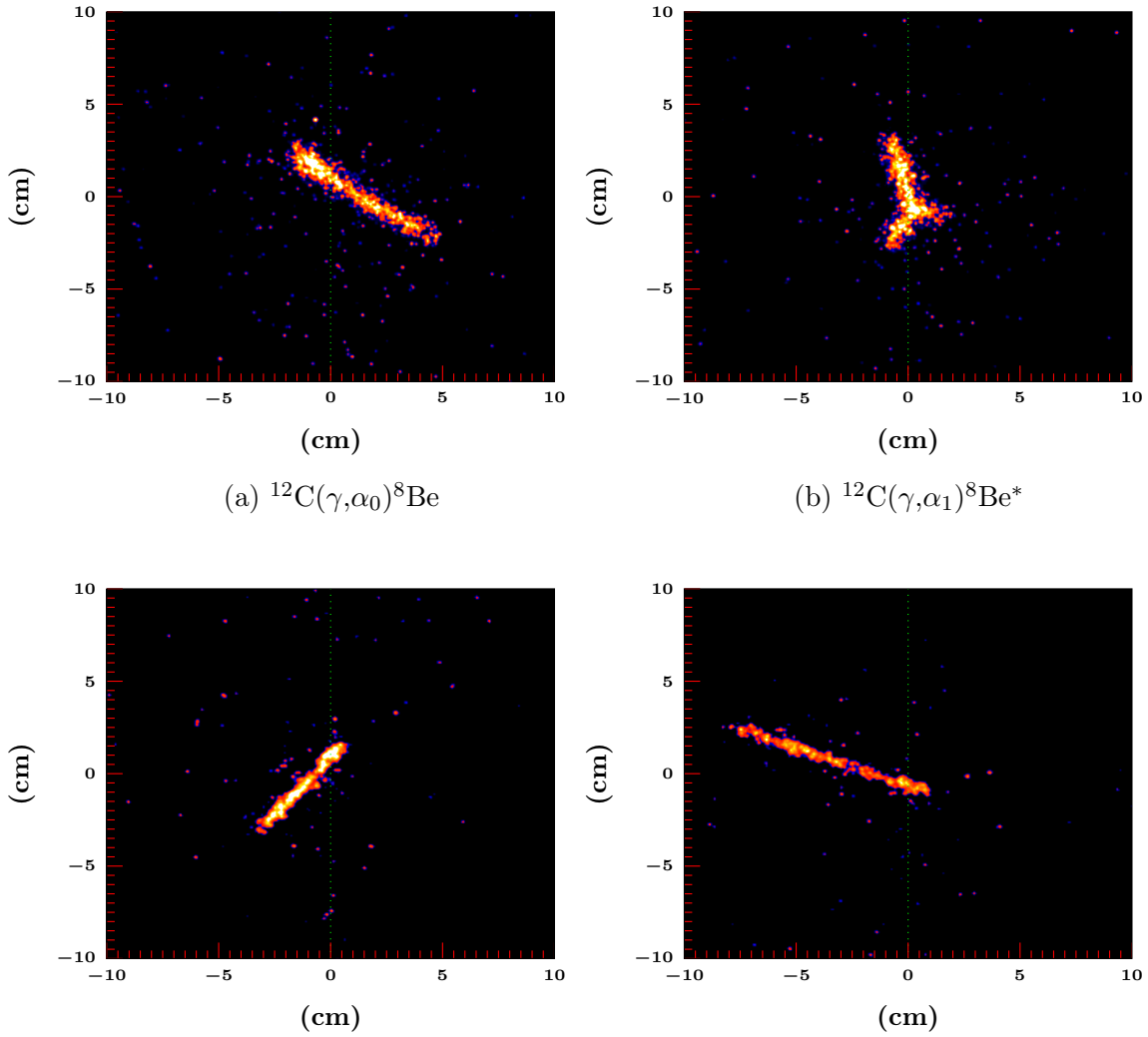

(a) $^{12}C(\gamma,\alpha_0)^8Be$

(b) $^{12}C(\gamma,\alpha_1)^8Be^*$

(c) $^{16}O(\gamma,\alpha)^{12}C$

(d) $^{18}O(\gamma,\alpha)^{14}C$

Figure 4.8: (γ, α) events recorded by the optics chain. The colors in the images represent the intensity of the light. The position of the beam is show by the dotted green lines.

$^{12}C(\gamma,\alpha_1)^8Be^*$ events, depending on beam energy. $^{12}C(\gamma,\alpha_1)^8Be^*$ events were excluded from angular distributions and calculations of total cross sections. A typical $^{12}C(\gamma,\alpha_1)^8Be^*$ event is shown in Figure 4.8b.

$^{16}O(\gamma,\alpha)^{12}C$: Photodisintegration of ^{16}O nuclei in the CO_2 target gas causes co-linear tracks from the recoiling ^{12}C nucleus and α particle. The tracks from

^{16}O(γ,α)^{12}C events (Figure 4.8c) are very similar to tracks from ^{12}C(γ,α_0)^{8}Be events. Furthermore, the difference in Q-values between ^{12}C(γ,α)^{8}Be events and ^{16}O(γ,α)^{12}C events (113 keV) is less than the typical γ-ray beam energy spread (350 keV), so the events cannot be identified based on energy. Discrimination between ^{16}O(γ,α)^{12}C events and ^{12}C(γ,α_0)^{8}Be events is based on fitting the time-projection signals and is discussed in Section 4.3.4.

^{18}O(γ,α)^{14}C: A small fraction (2.05×10^{-3}) of the oxygen nuclei in the CO_2 target gas are ^{18}O nuclei, which can be photodisintegrated into a ^{14}C nucleus and an α particle (Figure 4.8d). The Q-value for the ^{18}O(γ,α)^{14}C reaction (6.2270 MeV) is significantly smaller than the Q-value for both the ^{16}O(γ,α)^{12}C reaction (7.1620 MeV) and the ^{12}C(γ,α)^{8}Be(2α) reaction (7.3666 MeV), so ^{18}O(γ,α)^{14}C events are easily identified based on the deposited total energy.

4.2.2 Offline Level-2 Trigger

The purpose of the offline level-2 (L2) trigger is to reject a majority of the non-(γ, α) background events, reducing the total events which must be sorted by hand. The L2 trigger works by recording a set of parameters describing each event, then comparing these to parameters recorded for known (γ, α) events. Events whose parameters are sufficiently different from the ones established for (γ, α) events are rejected, leaving approximately $\frac{1}{10}$ of the original events.

Event Parameters

The event parameters used by the offline L2 trigger are described below. Event parameters based on the track images are shown in Figure 4.9.

Collected Charge: The total charge collected on the last of the high voltage grids

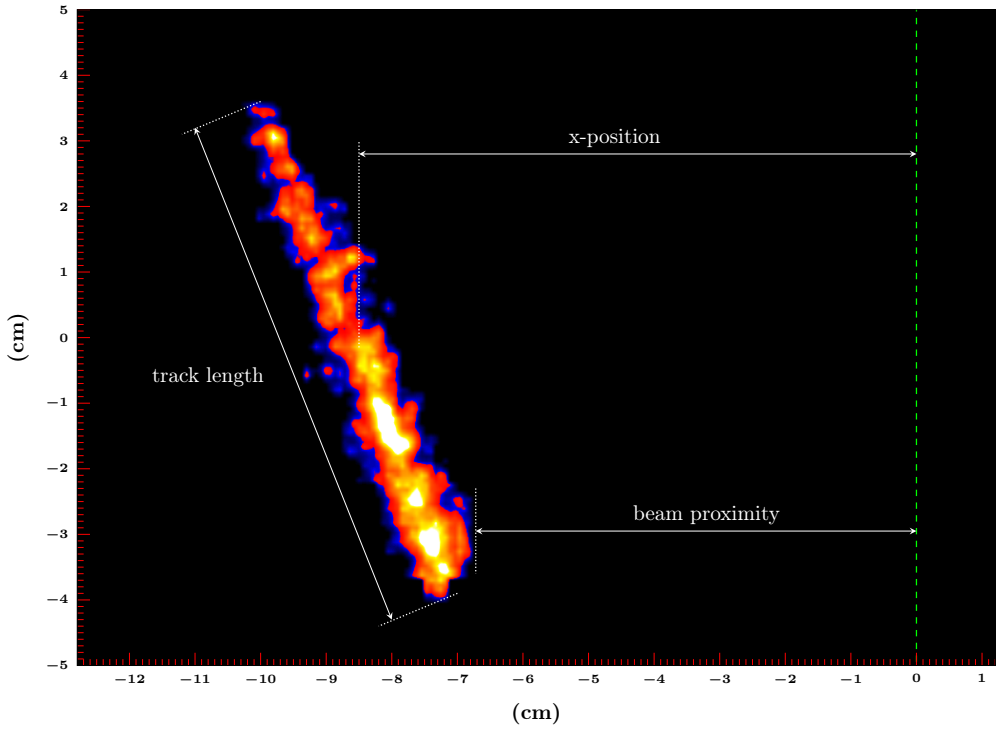

Figure 4.9: Offline L2 trigger event parameters related to the track image. The dashed green line shows the position of the γ-ray beam.

is recorded by the ADC (see Section 3.3). This is roughly proportional to the total energy deposited by the event, and cuts on the collected charge exclude most of the events which deposit too little energy (^{14}N(γ,p)^{13}C) or too much energy (sparks, cosmic-ray induced tracks) in the detector.

No Found Track: Events are excluded for which the track finding algorithm (Section 4.3.2) did not find any charged particle track in the image from the camera.

X-Position: The track fitting algorithm measures the perpendicular distance from the beam to the midpoint of the track (see Figure 4.9).

Beam Proximity: The beam proximity is the shortest distance from the beam to any part of the track (see Figure 4.9). If the track intersects the beam, this value is taken to be zero. Cuts on beam proximity exclude the events which

are not related to the beam.

Track Length: The track fitting algorithm measures the total length of the track (see Figure 4.9).

Calibration & Cuts

The threshold values for each of the event parameters used by the offline L2 trigger were set individually for each beam energy. (γ, α) events were hand-selected from the raw events, and the distributions of the event parameters for these known (γ, α) events were used to set the threshold values. The threshold values were set conservatively in order to not lose any (γ, α) events. Figure 4.10 shows the calibration of the offline L2 trigger for events taken at a beam energy of 10.25 MeV.

4.2.3 Hand Selection

Most of the non-(γ, α) background events were rejected by the offline L2 trigger. Even so, roughly half of the events accepted by the offline L2 trigger are (γ, α) events, which must be separated from the remaining background events by viewing each event individually. Figure 4.11 shows an example of two events—one background event and one (γ, α) event—which must be separated manually. The offline L2 trigger accepted both of the events due to their similar track lengths and positions. Identification of the (γ, α) event in Figure 4.11b is based on the time projection signal, which shows the characteristic stopping power of a recoiling nucleus and an α particle (see Section 4.3). The background event in Figure 4.11a has a time-projection signal showing the stopping power of a single particle. This background event is most likely a cosmic-ray induced charged particle.

The hand selection process is very effective at rejecting any remaining background

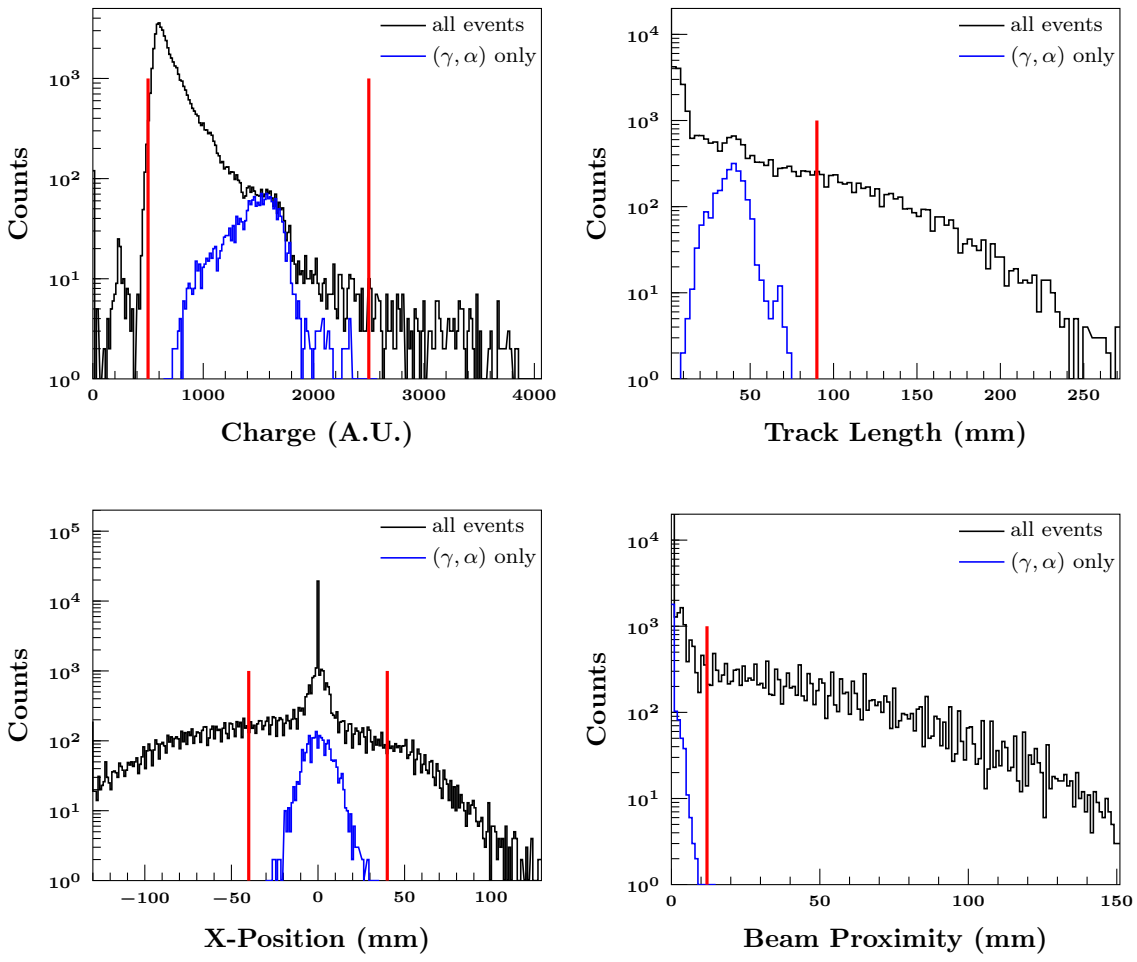

Figure 4.10: Calibration of the offline L2 trigger for events taken at a γ-ray beam energy of 10.25 MeV. The threshold values used for the offline L2 trigger (solid red lines) are shown for each of the event parameters.

events. It is, however, quite time consuming, requiring roughly 3 s for each of the 3,000–15,000 events accepted by the offline L2 trigger at each γ-ray beam energy.

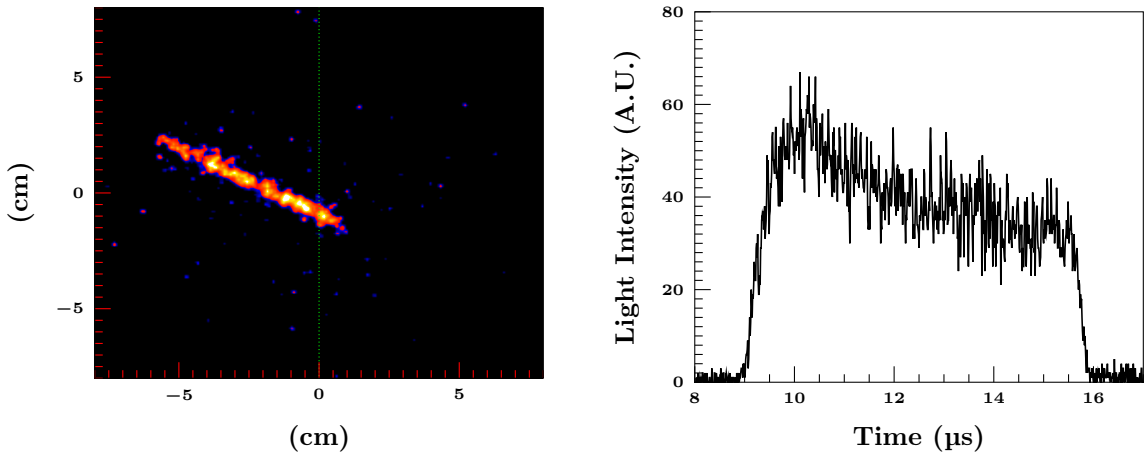

(a) Background event.

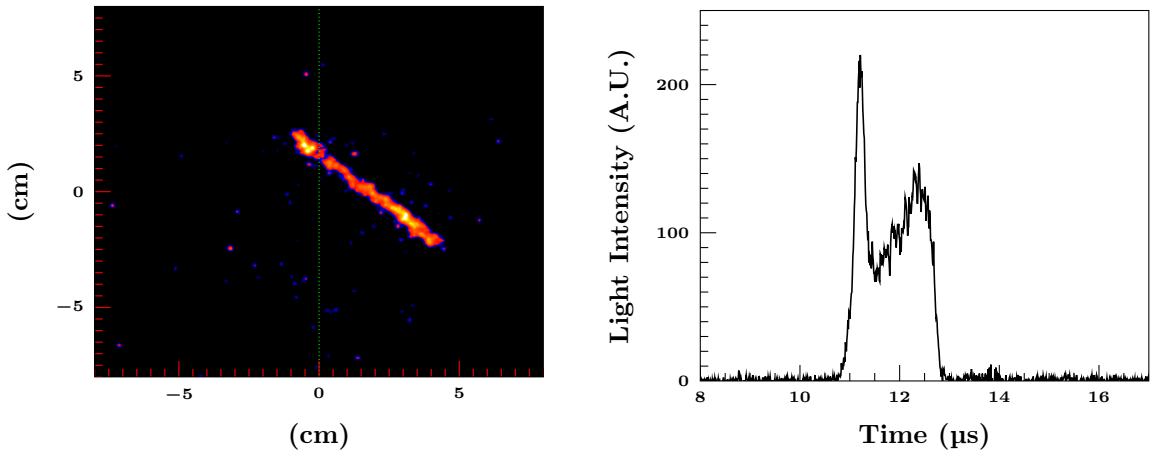

(b) (γ, α) event.

Figure 4.11: Hand selection of (γ, α) events. The photographs of the tracks are shown on the left, and the summed time-projection signals from the PMTs are shown on the right. The dotted green lines show the position of the γ-ray beam.

4.3 Event Reconstruction

4.3.1 Overview

Event reconstruction is the process of determining the event type, track length, energy, and spatial orientation of each (γ, α) event using the signals from the detector.

In particular, the photograph from the optics chain and the time projection signal from the PMTs provide the information needed to reconstruct each event.

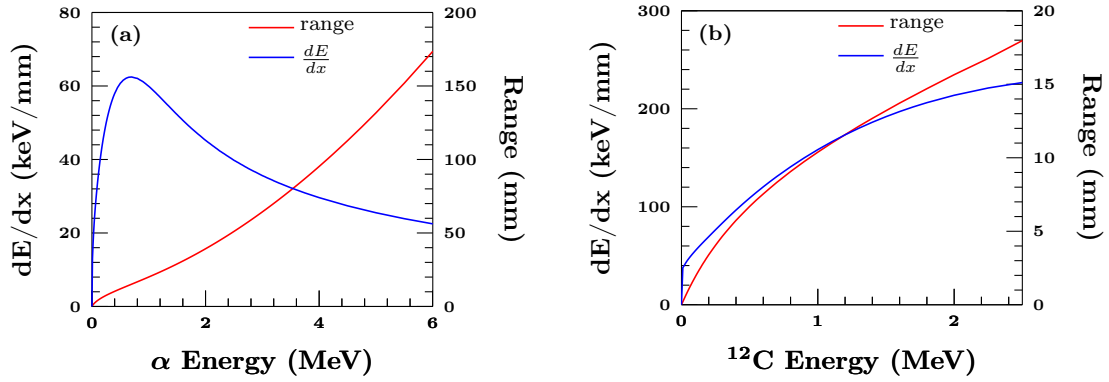

Figure 4.12: Stopping power (dE/dx) and ranges for (a) α particles and (b) ^{12}C nuclei in the 150 torr CO_2 and N_2 gas mixture used inside the drift chamber. The energy ranges shown are the typical ion energies in this experiment.

Both the optics chain and the PMTs measure the scintillation light produced along the length of the track once the ionization electrons reach the avalanche grids. The amount of ionization along each track is determined by the stopping power of the recoiling charged particle as it travels through the CO_2 and N_2 gas mixture used inside the drift chamber. The ranges and stopping powers were calculated using *Stopping and Range of Ions in Matter* (SRIM), software based on the binary collision approximation [Zie10]. Calculated stopping powers and ranges for α particles and ^{12}C nuclei in the gas mixture are shown in Figure 4.12.

Three-dimensional reconstructions of the events are made possible by projections of the the scintillation light as recorded in the photographs and time-projection signals (Figure 4.13). The photograph from the optics chain gives the projection of the tracks onto the plane defined by the last avalanche grid, while the time-projection signal from the PMTs give the projection of the tracks perpendicular to that plane.

Two angles are defined to simplify the reconstruction: the in-plane angle α and the out-of-plane angle β, shown in Figure 4.14. α is defined as the angle between

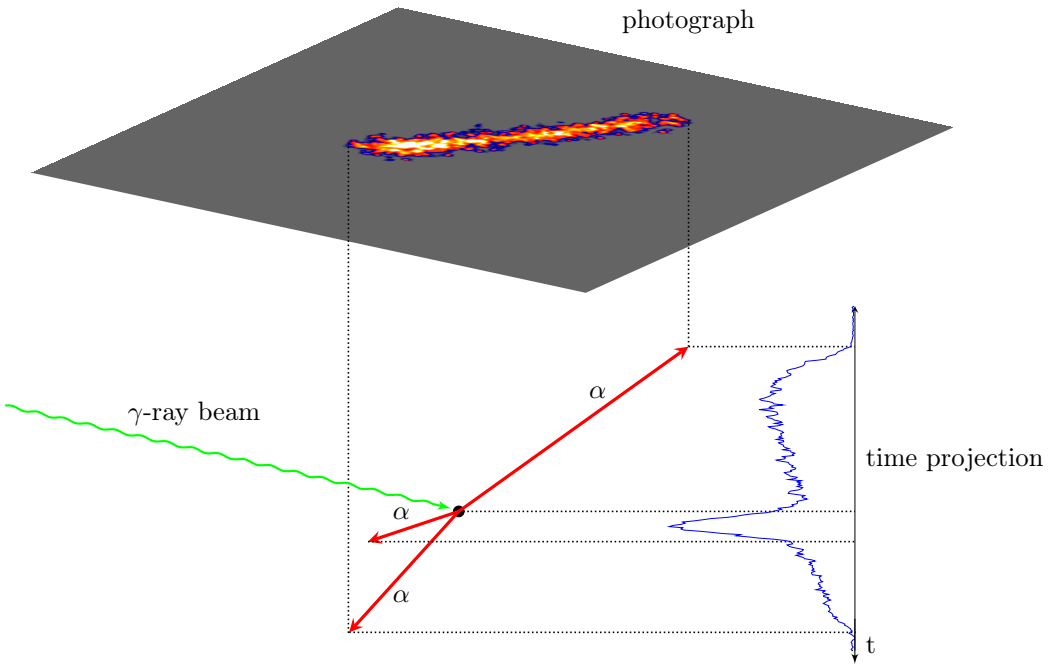

Figure 4.13: Projections of tracks from a typical $^{12}C(\gamma,\alpha_0)^8Be$ event used for event reconstruction. The photograph captures the two-dimensional projection of the α-particle tracks (red) onto the plane defined by the last avalanche grid (xz-plane). The projection onto the line perpendicular to that plane and parallel to the y-axis is captured in the time-projection signal.

the beam and the projection of the scattered particle onto the xz-plane (parallel to the last avalanche grid). β is defined as the angle between the scattered particle and the xz-plane. These angles are defined such that α can be extracted solely from the photograph of the tracks associated with the event, and β can be extracted solely from the time-projection signal.

The relation between the detector angles (α, β) and the spherical coordinate angles (θ, ϕ) is given by:

$$\begin{aligned} \sin\theta\ \cos\phi &= \sin\alpha\ \cos\beta \\ \sin\theta\ \sin\phi &= \sin\beta \\ \cos\theta &= \cos\alpha\ \cos\beta. \end{aligned} \tag{4.3}$$

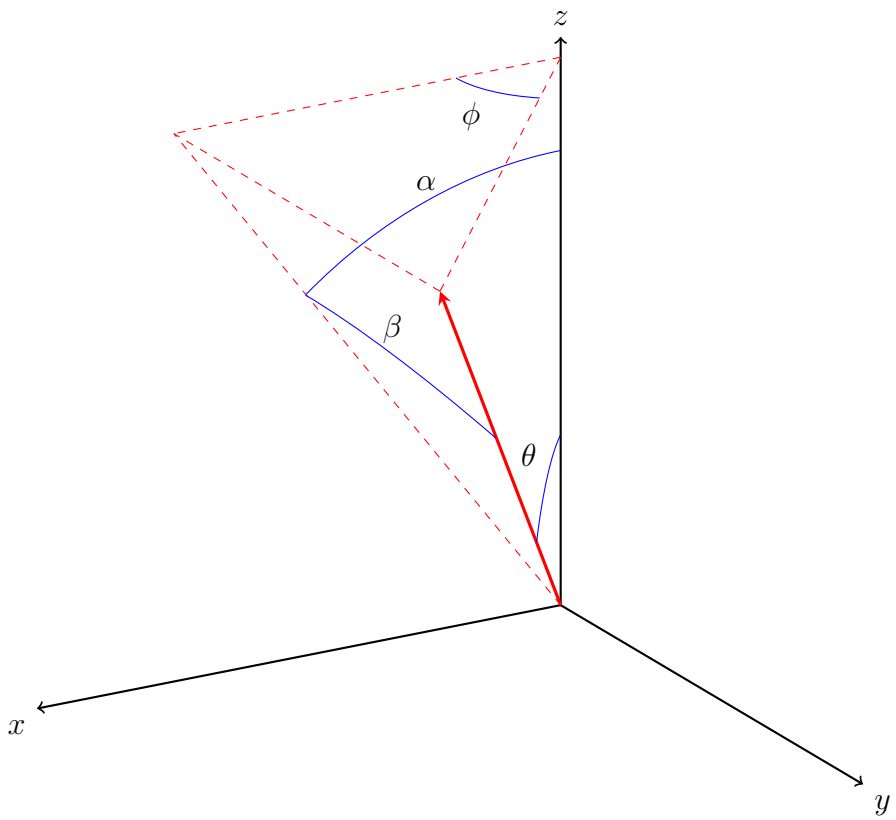

Figure 4.14: Detector coordinate system of the HIγS OTPC. The beam propagates along the z-axis, and the last avalanche grid is parallel to the xz-plane. The orientation of a scattered particle is described by the in-plane angle α and the out-of-plane angle β.

The volume element and differential solid angle can be written:

$$dV = r^2\, dr\, d\Omega = r^2 \cos\beta\, dr\, d\alpha\, d\beta. \tag{4.4}$$

The total length of each track is calculated by adding the in-plane and out-of-plane lengths in quadrature. The in-plane length is determined from the photograph (see Section 4.3.2), and the length-per-pixel was calibrated using an α-particle source inserted at known distances inside the drift chamber. The out-of-plane length is determined from the width of the time-projection signal multiplied by the velocity at which the ionization electrons drift through the gas in the applied electric field.

The drift velocity of the electrons was simulated using the *Magboltz* Monte Carlo simulation [Bia99], and is listed in Table 4.2. The diffusion of the electrons was also simulated to be a few µm, negligible compared to the track lengths.

Table 4.2: Drift velocities of ionization electrons in the gas target, simulated using the *Magboltz* Monte Carlo simulation [Bia99].

Gas Pressure (torr)	Electric Field (V/cm)	Drift Velocity (mm/µs)
100	168.3	11.43
150	216.4	9.702

The energy of each event is determined from the total track length using the tabulated ranges of ions in gas listed in SRIM [Zie10]. The energy resolution was measured to be 190 keV (FWHM) at an event energy of 2.7 MeV.

4.3.2 Track Fitting

The track fitting algorithm scans the photographs from each event for charged particle tracks. Once tracks have been found, the track length, orientation, and event energy are extracted from the photograph and from the time projection signal.

Image Processing

The camera inside the HIγS OTPC performs some on-board image processing, including analog gain and offset (contrast) enhancement. A photograph is recorded at the start of each run with the gated image intensifier deactivated, and this 'dark image' is subtracted from each of the event photographs. This reduces the background from any overactive pixels, dark current, or ambient light leaking into the optics chain.

In order to fit the track correctly the pixels in the photograph that are related to a charged particle track must be identified, and those that are not must be suppressed.

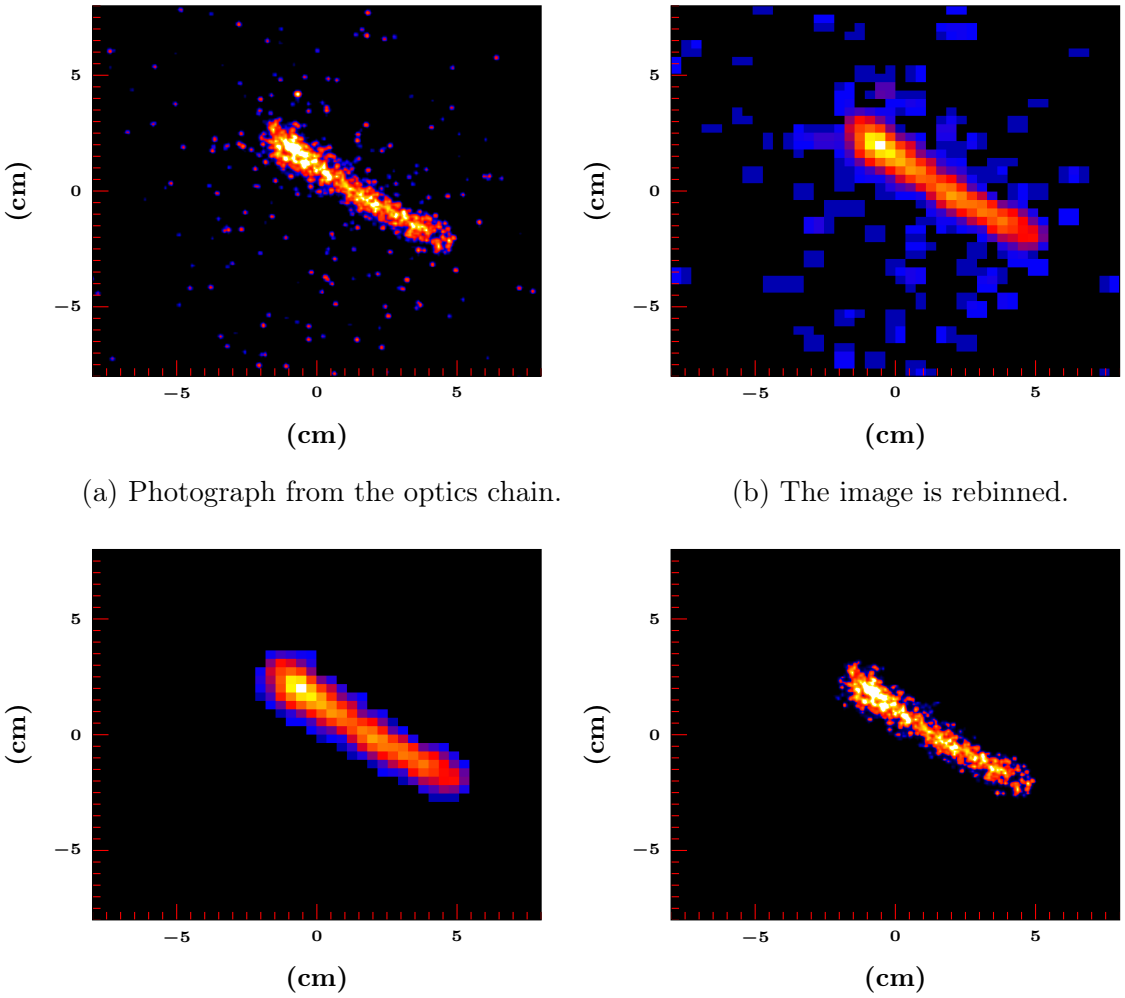

(a) Photograph from the optics chain.

(b) The image is rebinned.

(c) Pixels are suppressed.

(d) Clean image.

Figure 4.15: Images showing the progressive stages of the track image processing process.

This is accomplished using an algorithm based on the exposure level of neighboring pixels, shown in Figure 4.15. The original photograph (Figure 4.15a) is first re-binned 5×5, combining every 25 pixels into one (Figure 4.15b). The combined exposure level of each re-binned pixel is compared to an exposure threshold, set independently for each beam energy. Any re-binned pixel whose exposure level is less than the threshold is suppressed. Next, each re-binned pixel has eight neighboring pixels: immediately

above, below, to each side, and along the four diagonals. Any re-binned pixel that does not have at least five neighboring pixels with exposure levels above the threshold is suppressed. (Figure 4.15c). Finally, all of the pixels in the original photograph (not re-binned) which fall inside a suppressed re-binned pixel are also suppressed. This results in the suppression of all of the pixels that are not sufficiently grouped together with other exposed pixels, leaving only those associated with a charged particle track (Figure 4.15d).

Track Length, Orientation, & Energy

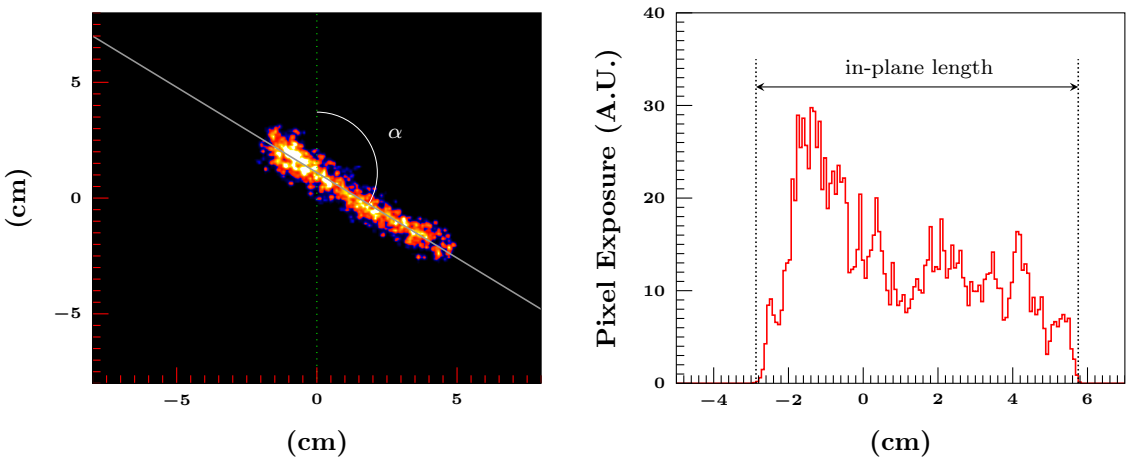

Figure 4.16: Left: The in-plane angle α is determined by fitting a line to the processed image of the track. Right: The in-plane length of the track is determined using the longitudinal projection of the image.

The in-plane angle α is determined by fitting a line to the processed track image, shown in Figure 4.16. The in-plane length of the track is determined using the longitudinal projection of the track image onto the fitted line. The length in pixels is calculated using the full-width at $\frac{1}{20}$ maximum, and the length-per-pixel was calibrated using an α-particle source inserted at known distances inside the drift chamber. This in-plane length measurement is accurate to $\pm 3\,\mathrm{mm}$.

4.3.3 Time Projection Fits

The time-projection signal from each identified (γ, α) event is fit twice: once using a line shape calculated for an $^{16}O(\gamma,\alpha)^{12}C$ event and once using a line shape calculated for a $^{12}C(\gamma,\alpha_0)^{8}Be$ event. This gives a measurement of the out-of-plane angle β which is accurate to $5^\circ \times \sin\beta$ (estimated from the uncertainty in the fits) and is essential for the classification of $^{16}O(\gamma,\alpha)^{12}C$ and $^{12}C(\gamma,\alpha_0)^{8}Be$ events (Section 4.3.4).

$^{16}O(\gamma,\alpha)^{12}C$ Event Time Projection Signals

The $^{16}O(\gamma,\alpha)^{12}C$ event time projection line shapes are calculated using $S_\alpha(x)$, the stopping power of an α particle at a position x along its track length, and $S_C(x)$, the stopping power for a ^{12}C nucleus. Both $S_\alpha(x)$ and $S_C(x)$ are calculated using the program SRIM [Zie10]. The time-projection signal is determined by the sum of $S_\alpha(x)$ and $S_C(x)$ projected onto the y-axis (Figure 4.17).

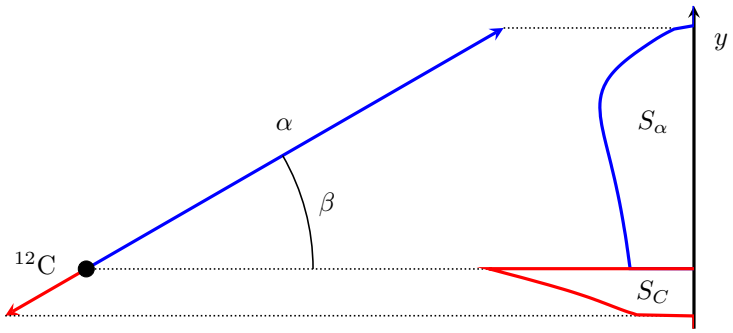

Figure 4.17: Illustration showing how the time-projection signal for an $^{16}O(\gamma,\alpha)^{12}C$ event is determined by the projection of the stopping power of the recoiling α particle and ^{12}C nucleus projected onto the y-axis.

As the electrons drift towards the avalanche grids, they diffuse slightly along the vertical axis. This diffusion, along with the finite rise time of the PMTs, causes a smearing of the time-projection signal. This effect is calculated by convolving a Gaussian of fixed width with the sum of $S_\alpha(x)$ and $S_C(x)$ projected onto the y-axis.

The resulting time-projection signal $T(t)$ is calculated using:

$$T(t) = \frac{N}{\sigma\sqrt{2\pi}} \int d\ell \left[S_\alpha(\ell) + S_C(\ell) \right] e^{\frac{-(v_d t - \ell \sin\beta)^2}{2\sigma^2}}, \tag{4.5}$$

where ℓ is the distance along the track, v_d is the drift velocity of the electrons, σ represents the level of smearing, and N is a normalization constant.

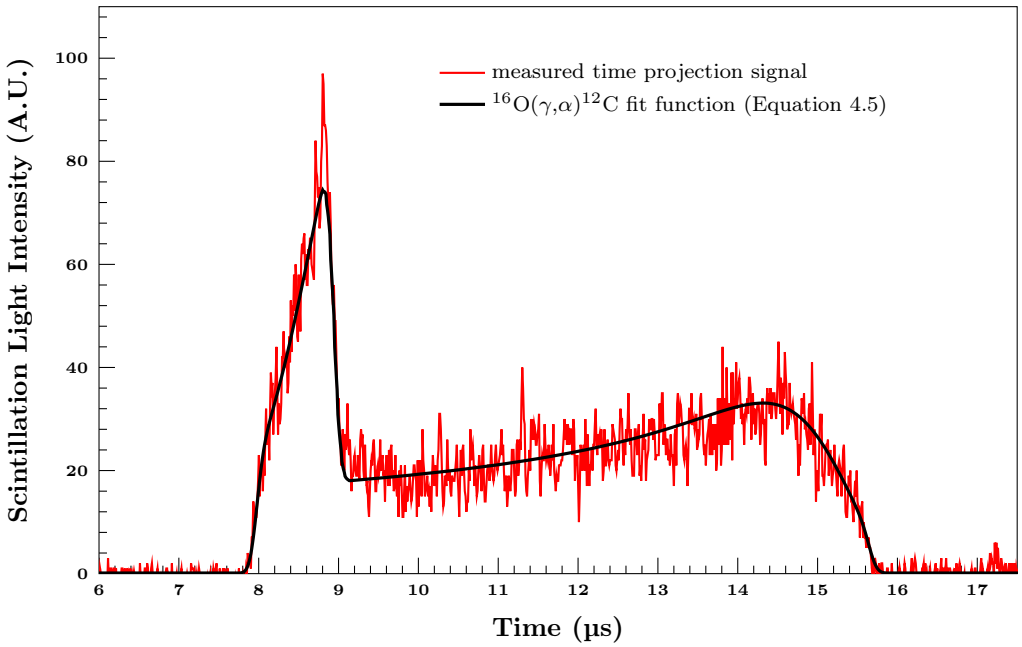

Figure 4.18: Time-projection signal from an ^{16}O$(\gamma,\alpha)^{12}$C event as a function of electron drift time (with an arbitrary offset), fit using the line shape $T(t)$ given in Equation 4.5.

Each (γ, α) event is fit using Equation 4.5. The energy is fixed using the value determined from the total track length, and N is fixed according to the integral of the measured time-projection signal. This leaves just one parameter for the fit, the out-of-plane angle β. An example fit to a time-projection signal from an ^{16}O$(\gamma,\alpha)^{12}$C event is shown in Figure 4.18.

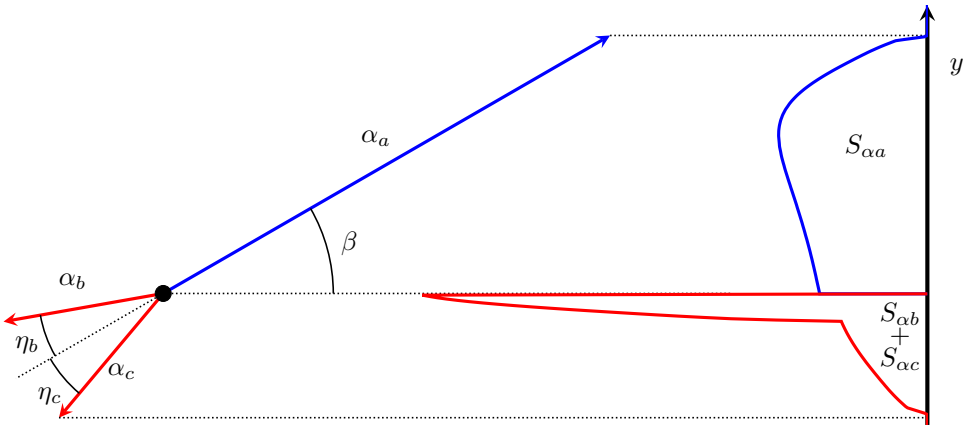

Figure 4.19: Illustration showing how the time-projection signal for an ^{12}C(γ,α_0)^{8}Be event is determined by the projection of the stopping power of the three recoiling α particles projected onto the y-axis. α_a is the α particle emitted from the decay of the ^{12}C nucleus; α_b and α_c are from the subsequent ^{8}Be decay.

^{12}C(γ,α_0)^{8}Be Event Time Projection Signals

The ^{12}C(γ,α_0)^{8}Be event time projection line shapes are calculated using the stopping powers of the three recoiling α particles: $S_{\alpha a}(x)$, $S_{\alpha b}(x)$, and $S_{\alpha c}(x)$. $S_{\alpha a}(x)$ represents the stopping power of the α particle produced from the initial decay of the ^{12}C nucleus. $S_{\alpha b}(x)$ and $S_{\alpha c}(x)$ represent the stopping powers of the two α particles produced in the subsequent decay of the ^{8}Be nucleus, projected onto the plane which contains the y-axis and the track of the first α particle (α_a). The time-projection signal is determined by the sum of the stopping power of the three α particles projected onto the y-axis (Figure 4.19), convolved with a Gaussian:

$$T(t) = \frac{N}{\sigma\sqrt{2\pi}} \int d\ell \left[S_{\alpha a}(\ell) e^{\frac{-(v_d t - \ell \sin\beta)^2}{2\sigma^2}} + S_{\alpha b}(\ell) e^{\frac{-(v_d t - \ell \sin(\beta+\eta_b))^2}{2\sigma^2}} + S_{\alpha c}(\ell) e^{\frac{-(v_d t - \ell \sin(\beta-\eta_c))^2}{2\sigma^2}} \right], \tag{4.6}$$

where η_b and η_c are the angles between the track of α_a and the tracks of α_b and α_c, projected onto the plane which contains the y-axis and the track of the first α particle (α_a). Since α_a and α_b are emitted with equal energy in the rest frame of the

^{8}Be nucleus, the angles η_b and η_c are determined kinematically from the energy of the recoiling ^{8}Be nucleus when it decays in flight and the angles (θ_{Be}, ϕ_{Be}) describing the orientation of the outgoing α particles in the rest frame of the ^{8}Be nucleus.

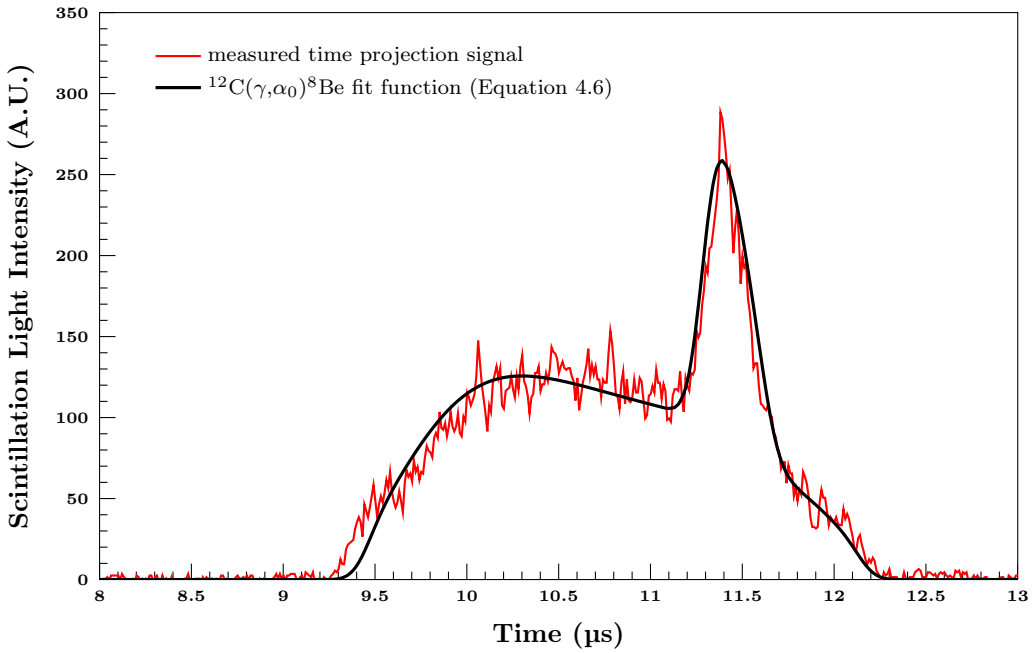

Figure 4.20: Time-projection signal from an ^{12}C(γ,α_0)^{8}Be event as a function of electron drift time (with an arbitrary offset), fit using the line shape $T(t)$ given in Equation 4.6.

Each (γ, α) event is fit using Equation 4.6. Like the ^{16}O(γ,α)^{12}C time projection fit, the energy is fixed using the value determined from the total track length, and N is fixed according to the integral of the measured time-projection signal. There are three remaining free parameters: the out-of-plane angle β, and the angles (θ_{Be},ϕ_{Be}).

Equation 4.6 is much slower to calculate numerically than Equation 4.5 and has more parameters. This makes the ordinary minimization routine used for fitting the ^{16}O(γ,α)^{12}C time-projection signals impractical. Instead, the function was calculated and tabulated for center-of-mass energies from 1–6 MeV in 100 keV steps, out-of-plane angles from -90 to 90° in 1° steps, and 20 unique configurations of (θ_{Be},ϕ_{Be}). An

event of a given energy is fit using all 3620 functions, and the fit yielding the lowest value of χ^2 is selected.

Cluster Computing

Fitting time-projection signals using Equations 4.5 and 4.6 is numerically intensive, requiring 100–150 seconds per CPU per event. The fitting was performed using the Duke Shared Resource Cluster (DSCR), a 5300-CPU parallel computing environment. Each fitting job allocates one event at a time to any available CPU, which performs the fits independently and records the results.

4.3.4 Classification of (γ, α) Events

After the raw events have been separated into (γ, α) events and background events (described in Section 4.2), the (γ, α) events are classified into the ^{12}C(γ,α_0)^{8}Be signal events and the ^{12}C(γ,α_1)^{8}Be*, ^{16}O(γ,α)^{12}C, and ^{18}O(γ,α)^{14}C background events, respectively.

^{12}C(γ,α_1)^{8}Be*

^{12}C(γ,α_1)^{8}Be* events are easily recognizable from the large opening angle of the α particles (see Figure 4.8b). During the hand analysis, all of the ^{12}C(γ,α_1)^{8}Be* events are flagged. Because ^{12}C(γ,α_1)^{8}Be* events decay through the broad first excited state in ^{8}Be, it is not possible to discern which of the three α particles was produced in the initial decay of the ^{12}C nucleus, and ^{12}C(γ,α_1)^{8}Be* events are indistinguishable from direct three-body decays. This makes angular distributions impossible to determine and the efficiency of fiducial angular cuts (Section 4.4.3) impossible to calculate. The very small number of recorded ^{12}C(γ,α_1)^{8}Be* events were therefore excluded from

further analysis and results.

^{18}O(γ,α)^{14}C

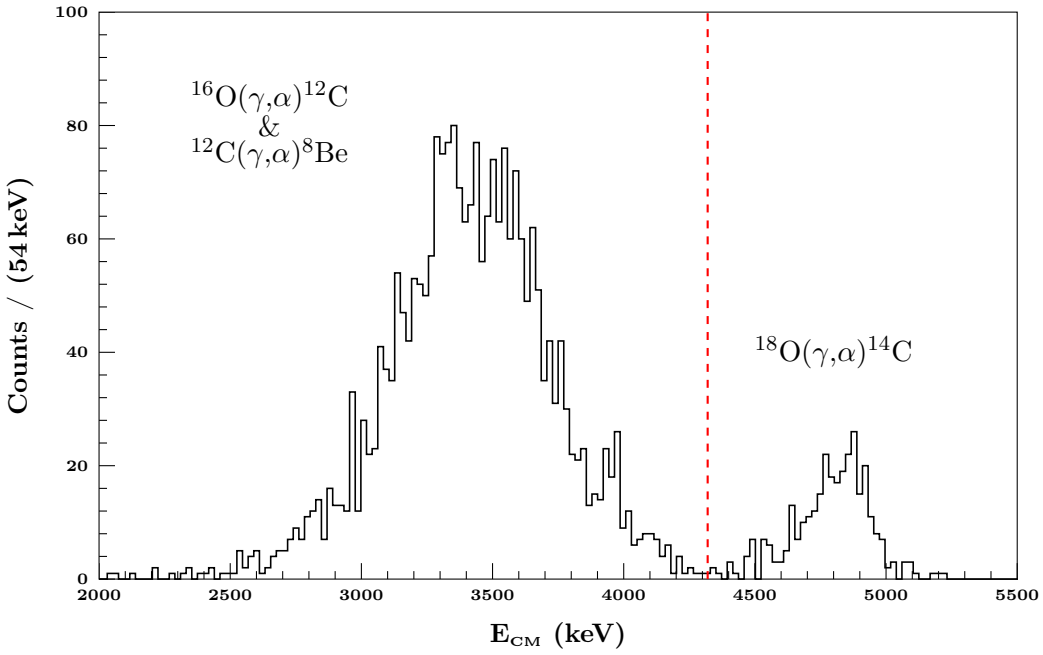

Figure 4.21: The number of events plotted as a function of the total center-of-mass energy as determined from the track lengths.

Because the Q-value for the (γ, α) reaction is significantly lower in ^{18}O (6.2270 MeV) than in either ^{16}O (7.1620 MeV) or ^{12}C (7.3666 MeV), ^{18}O(γ,α)^{14}C events can be easily identified based on the energy of the event, as determined from the total track length. Figure 4.21 shows removal of ^{18}O(γ,α)^{14}C events using a cut in energy.

^{12}C(γ,α_0)^{8}Be & ^{16}O(γ,α)^{12}C

Both ^{12}C(γ,α_0)^{8}Be events and ^{16}O(γ,α)^{12}C events deposit a similar amount of energy, and the tracks from the two different events are indistinguishable (see Figures 4.8a and 4.8c). Discrimination between the two types of events is based on

the goodness-of-fit values obtained by fitting the time-projection signals. The time-projection signal from each remaining unclassified (γ, α) event is fit using line shapes from both ^{12}C(γ,α_0)^{8}Be and ^{16}O(γ,α)^{12}C event types (Equations 4.6 and 4.5), and χ^2 from each fit is recorded. Figure 4.22a shows the results of fitting the time-projection signals from a combination of ^{12}C(γ,α_0)^{8}Be events and ^{16}O(γ,α)^{12}C events using both Equation 4.6 ($\chi^2_{\rm C}$) and Equation 4.5 ($\chi^2_{\rm O}$).

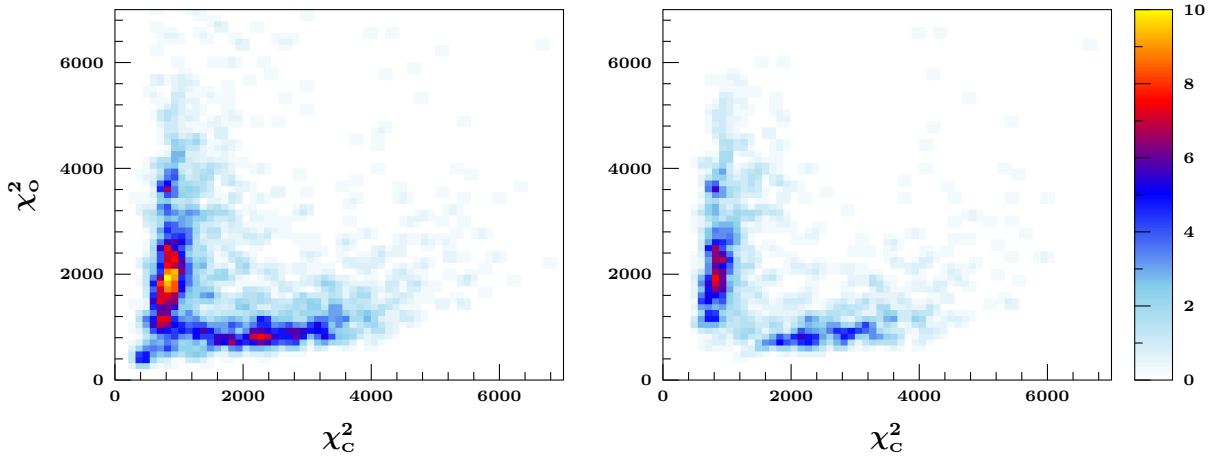

(a) (b)

Figure 4.22: Plot of the χ^2 values from the fits to the time-projection signals assuming an ^{16}O(γ,α)^{12}C line shape ($\chi^2_{\rm O}$) versus those assuming a ^{12}C(γ,α_0)^{8}Be line shape ($\chi^2_{\rm C}$) at a γ-ray beam energy of 9.4 MeV; (a): before any cut in the out-of-plane angle β, (b): only events where $|\beta| > 20°$.

For events occurring strictly in the plane parallel to the high-voltage grids (xz-plane), the out of plane angle $\beta = 0$, and the function describing the line shape of the time projection signal from ^{16}O(γ,α)^{12}C events (Equation 4.5) reduces to:

$$\begin{aligned} T(t) &= \frac{N}{\sigma\sqrt{2\pi}} \int d\ell \left[S_\alpha(\ell) + S_C(\ell) \right] e^{\frac{-(v_d t)^2}{2\sigma^2}} \\ &= \frac{1}{\sigma\sqrt{2\pi}} e^{\frac{-(v_d t)^2}{2\sigma^2}} \times L, \end{aligned} \tag{4.7}$$

where L is a constant proportional to the total amount of detected scintillation light.

Similarly, the function describing the line shape of the time projection signal from ^{12}C(γ,α_0)^{8}Be events (Equation 4.6) reduces to:

$$T(t) = \frac{N}{\sigma\sqrt{2\pi}} \int d\ell \ \left[S_{\alpha a}(\ell) e^{\frac{-(v_d t)^2}{2\sigma^2}} + S_{\alpha b}(\ell) e^{\frac{-(v_d t - \ell \sin\eta_b)^2}{2\sigma^2}} + S_{\alpha c}(\ell) e^{\frac{-(v_d t + \ell \sin\eta_c)^2}{2\sigma^2}} \right]. \tag{4.8}$$

In ^{12}C(γ,α)^{8}Be events where the α particles from the decay of ^{8}Be are also emitted in the xz-plane, $\eta_b = 0$ and $\eta_c = 0$, and Equation 4.8 further reduces to:

$$\begin{aligned} T(t) &= \frac{N}{\sigma\sqrt{2\pi}} \int d\ell \ \left[S_{\alpha a}(\ell) + S_{\alpha b}(\ell) + S_{\alpha c}(\ell) \right] e^{\frac{-(v_d t)^2}{2\sigma^2}} \\ &= \frac{1}{\sigma\sqrt{2\pi}} e^{\frac{-(v_d t)^2}{2\sigma^2}} \times L. \end{aligned} \tag{4.9}$$

Equations 4.7 and 4.9 describe the time-projection signals from in-plane ^{16}O(γ,α)^{12}C and ^{12}C(γ,α_0)^{8}Be events, and they are equivalent. These events have indistinguishable time-projection signals, so no discrimination is possible between events of this type.

In order to exclude these events, a fiducial cut is made in the out-of-plane angle β. The cut requires $|\beta| > \beta_c$, where β_c was determined separately for each γ-ray beam energy and gas pressure. Figure 4.22b shows the effect of the fiducial cut in β on the distribution of χ^2 from the time projection fits.

The final discrimination between ^{16}O(γ,α)^{12}C and ^{12}C(γ,α_0)^{8}Be events is accomplished by calculating the asymmetry in χ^2 for each event:

$$A_{\chi^2} \equiv \frac{\chi^2_{\rm C} - \chi^2_{\rm O}}{\chi^2_{\rm C} + \chi^2_{\rm O}}, \tag{4.10}$$

and making a cut to separate the two types of events. Figure 4.23 shows the distribution of A_{χ^2} for a γ-ray beam energy of 9.8 MeV. The efficiency of the cut and

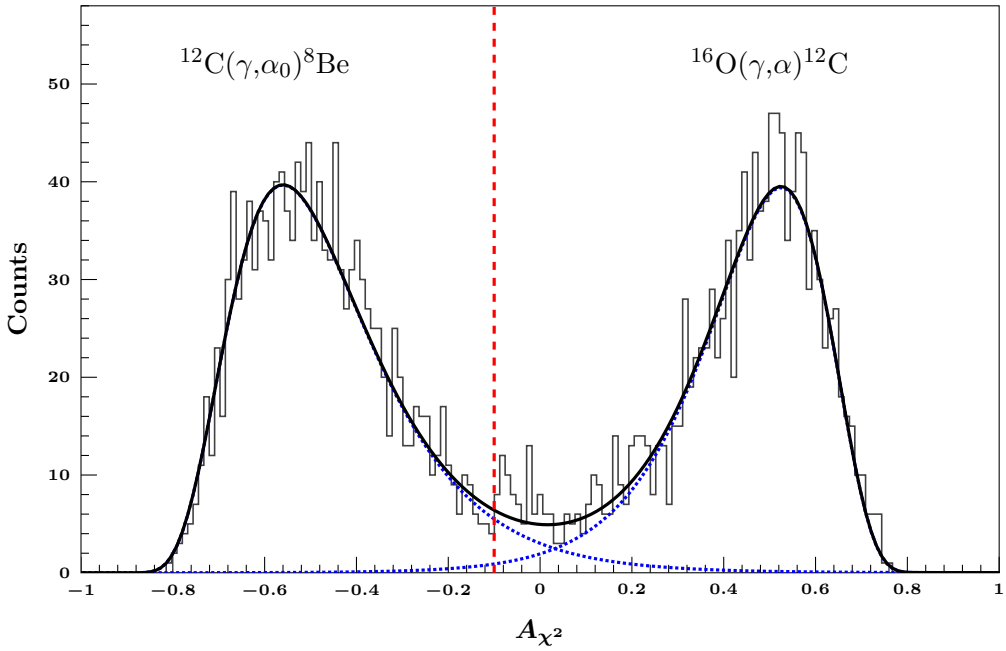

Figure 4.23: The number of events as a function of the χ^2 asymmetry parameter A_{χ^2} (Equation 4.10). The distribution is fit to the sum (solid black line) of two log-normal distributions (dotted blue lines). All of the events to the left of the cut (dotted red line) are identified as ^{12}C(γ,α_0)^{8}Be events.

the leakage of ^{16}O(γ,α)^{12}C events into those events identified as ^{12}C(γ,α_0)^{8}Be are estimated by fitting the A_{χ^2} distribution to the sum of two log-normal distributions and integrating the respective ^{16}O(γ,α)^{12}C and ^{12}C(γ,α_0)^{8}Be contributions. The cuts in A_{χ^2} were performed separately for each beam energy such that the leakage of ^{16}O(γ,α)^{12}C events integrated over all angles was less than 0.5 %.

4.4 Angular Distributions

4.4.1 Unbinned Maximum Likelihood Fits

Because angular information was available for each ^{12}C(γ,α_0)^{8}Be event individually, unbinned maximum likelihood (UML) fits were used to extract parameters from the angular distributions. Unlike a χ^2 fit, the results of an UML fit are not affected

by a choice in binning. In a UML fit, the parameters are varied in order to maximize the likelihood $\mathcal{L}$:

$$\mathcal{L} = \prod_i f(x_i|\theta), \tag{4.11}$$

where $f(x_i|\theta)$ is a probability distribution function (PDF) evaluated at each measured value x_i with parameters θ. The fit function must be a valid PDF, with a total integral equal to unity. Because $\mathcal{L}$ is difficult to calculate using floating-point numbers, the log-likelihood is normally used instead:

$$\ell = \ln \mathcal{L} = \sum_i \ln f(x_i|\theta). \tag{4.12}$$

Once the parameters have been found which maximize ℓ, the uncertainty in each of the parameters is calculated using deviations in ℓ from its maximum value [Lyo86]:

$$\begin{aligned} \ell_{\text{MAX}} - \ell &= \frac{1}{2}, \quad 1\sigma \\ \ell_{\text{MAX}} - \ell &= 2, \quad 2\sigma \end{aligned} \tag{4.13}$$

4.4.2 Angular Fit Function

The angular distribution for the photodisintegration of ^{12}C into spinless particles with $E1$ and $E2$ radiation is [Dye74, Assu06]:

$$\begin{aligned} W(\theta) =& \Big(3|E1|^2 + 5|E2|^2\Big) P_0(\cos\theta) + \Big(\frac{25}{7}|E2|^2 - 3|E1|^2\Big) P_2(\cos\theta) \\ &- \frac{60}{7}|E2|^2 P_4(\cos\theta) + 6\sqrt{3}|E1||E2|\cos\phi_{12}\Big(P_1(\cos\theta) - P_3(\cos\theta)\Big), \end{aligned} \tag{4.14}$$

where $E1$ and $E2$ are the electric dipole and quadrupole amplitudes, and ϕ_{12} is the phase difference between them. Put more simply:

$$W(\theta) = \frac{3}{2}\sin^2\theta\left(3|E1|^2 + 25|E2|^2\cos^2\theta + 10\sqrt{3}|E1||E2|\cos\phi_{12}\cos\theta\right). \quad (4.15)$$

Since maximum likelihood fit functions are necessarily normalized to unity, an equivalent angular distribution can be written using the ratio of amplitudes:

$$W(\theta) = \frac{3\,\sin^2\theta}{2|E1|^2}\left(3 + 25\left(\frac{|E2|}{|E1|}\right)^2\cos^2\theta + 10\sqrt{3}\frac{|E2|}{|E1|}\cos\phi_{12}\cos\theta\right). \quad (4.16)$$

Substituting the detector angles (α, β) for the scattering angle θ (Equation 4.3), Equation 4.16 becomes:

$$\begin{aligned} W(\alpha,\beta) =& \frac{3}{2|E1|^2}\left(1 - \cos^2\alpha\cos^2\beta\right) \\ &\times\left(3 + 25\left(\frac{|E2|}{|E1|}\right)^2\cos^2\alpha\cos^2\beta + 10\sqrt{3}\frac{|E2|}{|E1|}\cos\phi_{12}\cos\alpha\cos\beta\right). \end{aligned} \quad (4.17)$$

Convolution in α and β

The HIγS OTPC measures α and β separately for each event, so the angular fit function must be a convolution of the angular distribution with the detector response functions for both α and β. Assuming the detector response function in α follows a Gaussian distribution with standard deviation σ_α, the α-convolved angular distribution is:

$$\begin{aligned} W_{\otimes\alpha}(\alpha,\beta) =& W(\alpha,\beta)\otimes\frac{1}{\sqrt{2\pi}\sigma_\alpha}e^{-\frac{\alpha^2}{2\sigma_\alpha^2}} \\ =& \frac{1}{\sqrt{2\pi}\sigma_\alpha}\int_{-\infty}^{\infty} d\alpha'\; W(\alpha',\beta)e^{-\frac{(\alpha-\alpha')^2}{2\sigma_\alpha^2}}. \end{aligned} \quad (4.18)$$

Solving the Gaussian integral analytically, the $E1$, $E2$, and mixing components of the α-convolved angular distribution are:

$$
\begin{aligned}
W_{E1}(\alpha,\beta) &= 48\left(3-\cos 2\beta - 2e^{-2\sigma_\alpha^2}\cos 2\alpha\cos^2\beta\right) \\
W_{E2}(\alpha,\beta) &= 25\left(\frac{|E2|}{|E1|}\right)^2 \\
&\quad\times\left(7+32e^{-2\sigma_\alpha^2}\cos 2\alpha\cos^2\beta\sin^2\beta - 8e^{8\sigma_\alpha^2}\cos 4\alpha\cos^4\beta + 4\cos 2\beta - 3\cos 4\beta\right) \\
W_{\text{MIX}}(\alpha,\beta) &= 40\sqrt{3}\frac{|E2|}{|E1|}\cos\phi_{12} \\
&\quad\times\left(e^{-\sigma_\alpha^2/2}\cos\alpha\big(7\cos\beta - 3\cos 3\beta\big) + 4e^{-\frac{9}{2}\sigma_\alpha^2}\cos 3\alpha\cos^3\beta\right),
\end{aligned}
\tag{4.19}
$$

and the full α-convolved angular distribution is:

$$
W_{\otimes\alpha}(\alpha,\beta) = N\Big[W_{E1}(\alpha,\beta) + W_{E2}(\alpha,\beta) + W_{\text{MIX}}(\alpha,\beta)\Big], \tag{4.20}
$$

where N is a normalization constant such that $W_{\otimes\alpha}(\alpha,\beta)$ is a valid PDF with a total integral equal to unity.

Similarly, by assuming that the detector response function in β follows a Gaussian distribution with standard deviation σ_β, the α- and β-convolved angular distribution is:

$$
\begin{aligned}
W_{\otimes\alpha\beta}(\alpha,\beta) =& W_{\otimes\alpha}(\alpha,\beta)\otimes\frac{1}{\sqrt{2\pi}\sigma_\alpha}e^{-\frac{\alpha^2}{2\sigma_\alpha^2}} \\
=& \frac{1}{\sqrt{2\pi}\sigma_\alpha}\int_{-\infty}^{\infty} d\alpha'\, W_{\otimes\alpha}(\alpha',\beta)e^{-\frac{(\alpha-\alpha')^2}{2\sigma_\alpha^2}}.
\end{aligned}
\tag{4.21}
$$

Solving the Gaussian integral analytically once again, the $E1$, $E2$, and mixing com-

ponents of the α- and β-convolved angular distribution are:

$$W_{E1}(\alpha,\beta) = 48\Big(3 - e^{-2\sigma_\beta^2}\cos 2\beta - e^{-2(\sigma_\alpha^2+\sigma_\beta^2)}\cos 2\alpha\big(\cos 2\beta + e^{2\sigma_\beta^2}\big)\Big) \tag{4.22}$$

$$\begin{aligned} W_{E2}(\alpha,\beta) &= 25\left(\frac{|E2|}{|E1|}\right)^2 e^{-8(\sigma_\alpha^2+\sigma_\beta^2)} \\ &\times\Big(e^{8\sigma_\alpha^2}\big(7e^{8\sigma_\beta^2} + 4e^{6\sigma_\beta^2}\cos 2\beta - 3\cos 4\beta\big) + 4e^{6\sigma_\alpha^2}\cos 2\alpha\big(e^{8\sigma_\beta^2} - \cos 4\beta\big) \\ &\quad - \cos 4\alpha\big(3e^{8\sigma_\beta^2} + 4e^{6\sigma_\beta^2}\cos 2\beta + \cos 4\beta\big)\Big) \\ W_{\text{MIX}}(\alpha,\beta) &= -40\sqrt{3}\frac{|E2|}{|E1|}\cos\phi_{12}e^{-\frac{9}{2}(\sigma_\alpha^2+\sigma_\beta^2)}\cos\alpha\cos\beta \\ &\times\Big(4e^{4\sigma_\beta^2}\big(6\cos 2\alpha - 7e^{4\sigma_\alpha^2} - 3\big) + \big(2\cos 2\beta - 1\big)\big(3e^{4\sigma_\alpha^2} - 2\cos 2\alpha - 1\big)\Big), \end{aligned}$$

and the full α- and β-convolved angular distribution is:

$$W_{\otimes\alpha\beta}(\alpha,\beta) = N\Big[W_{E1}(\alpha,\beta) + W_{E2}(\alpha,\beta) + W_{\text{MIX}}(\alpha,\beta)\Big]. \tag{4.23}$$

The normalization constant N is calculated numerically such that $W_{\otimes\alpha\beta}(\alpha,\beta)$ is a valid PDF with a total integral equal to unity.

Extracting Parameters from Angular Fits

The angular data recorded at each γ-ray beam energy were fit using Equation 4.23 with two free parameters: $\frac{|E2|}{|E1|}$ and $\cos\phi_{12}$. Figure 4.24 shows a fit to the angular data performed to determine the angular parameters. Correlations and anti-correlations in the parameters were propagated into extracted values of the fit parameters by mapping the complete 1σ and 2σ contours in the log-likelihood space (Equation 4.13), and using the extreme 1σ values as the definition of the uncertainty of each parameter.

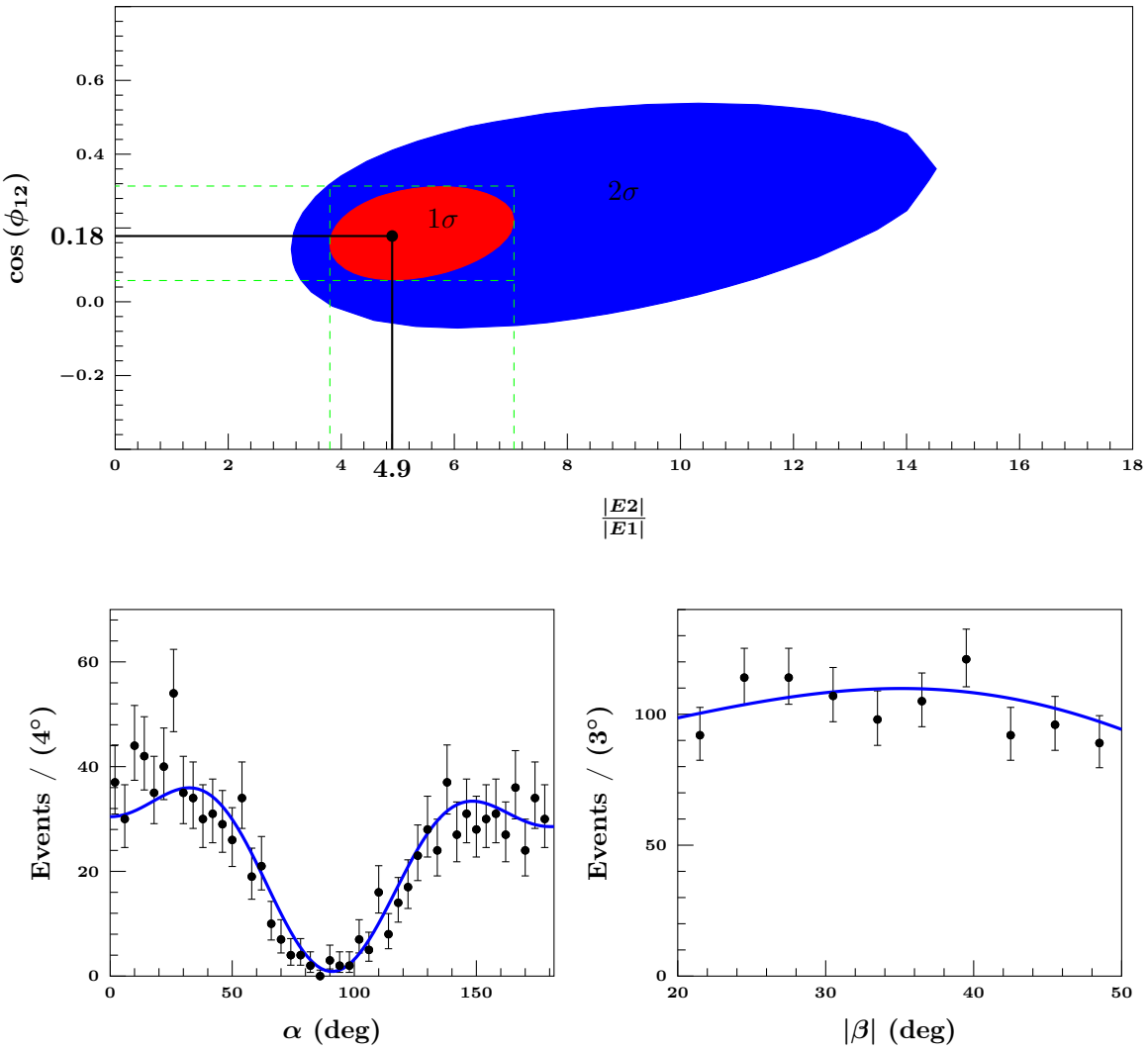

Figure 4.24: Fit to angular data taken at a beam energy of 9.6 MeV using Equation 4.23. Top: Plot of $\cos(\phi_{12})$ versus $\frac{|E2|}{|E1|}$ showing the 1σ and 2σ range in values. The dashed green lines show the adopted uncertainties. Bottom: Measured angular data along with the angular fit function for detector angles α and β. In each case the distributions are integrated over the unseen angle. The error bars represent the statistical uncertainty associated with each data point.

4.4.3 Fiducial Cuts in β

As discussed in Section 4.3.4, (γ, α) events which occurred in the xz-plane ($\beta = 0°$) could not be effectively identified, and a fiducial cut was applied in order to reject

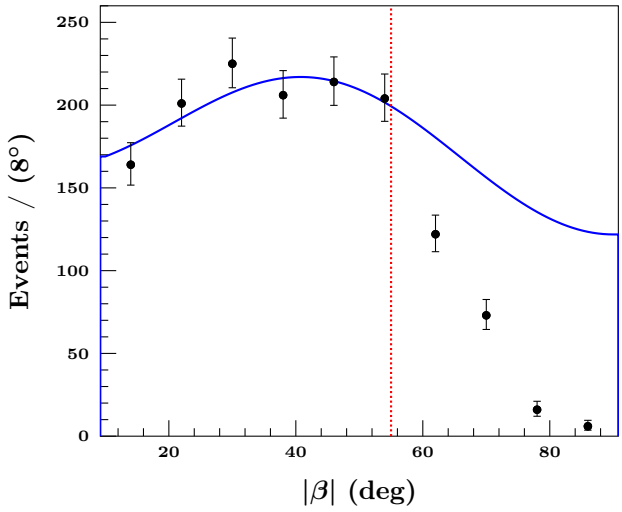

Figure 4.25: Fiducial cut in the out-of-plane angle β due to sparking for events taken at a beam energy of 10.8 MeV. The blue curve represents the distribution in $|\beta|$ using Equation 4.23, normalized to the data to the left of the cut. The dotted red line shows the cut; all events to the right were discarded.

all in-plane events. Additionally, any (γ, α) event in which the α particle travels perpendicular to the xz-plane is likely to cause a charge density on the avalanche grids greater than the Raether limit [Rae64], leading to a spark in the drift chamber. In order to remove the contribution from events that resulted in a spark, a fiducial cut was made in β, requiring $|\beta| \leq \beta_{\text{SPARK}}$, where β_{SPARK} was determined separately for each γ-ray beam energy and drift chamber gas pressure. Figure 4.25 shows the effect of sparking on the distribution in β and the fiducial cut.

The efficiency of the fiducial cuts in β depends strongly on the angular distribution as well as the values of the fiducial cuts. For each angular fit, pseudo-data were created by randomly generating events with outgoing angles distributed according to the measured angular distribution, and the same fiducial cuts were applied to the pseudo-data as to the measured data. The efficiency of the cuts was determined by comparing the number of generated events that survived the cuts to the total number of generated events. Enough events were generated such that the Monte

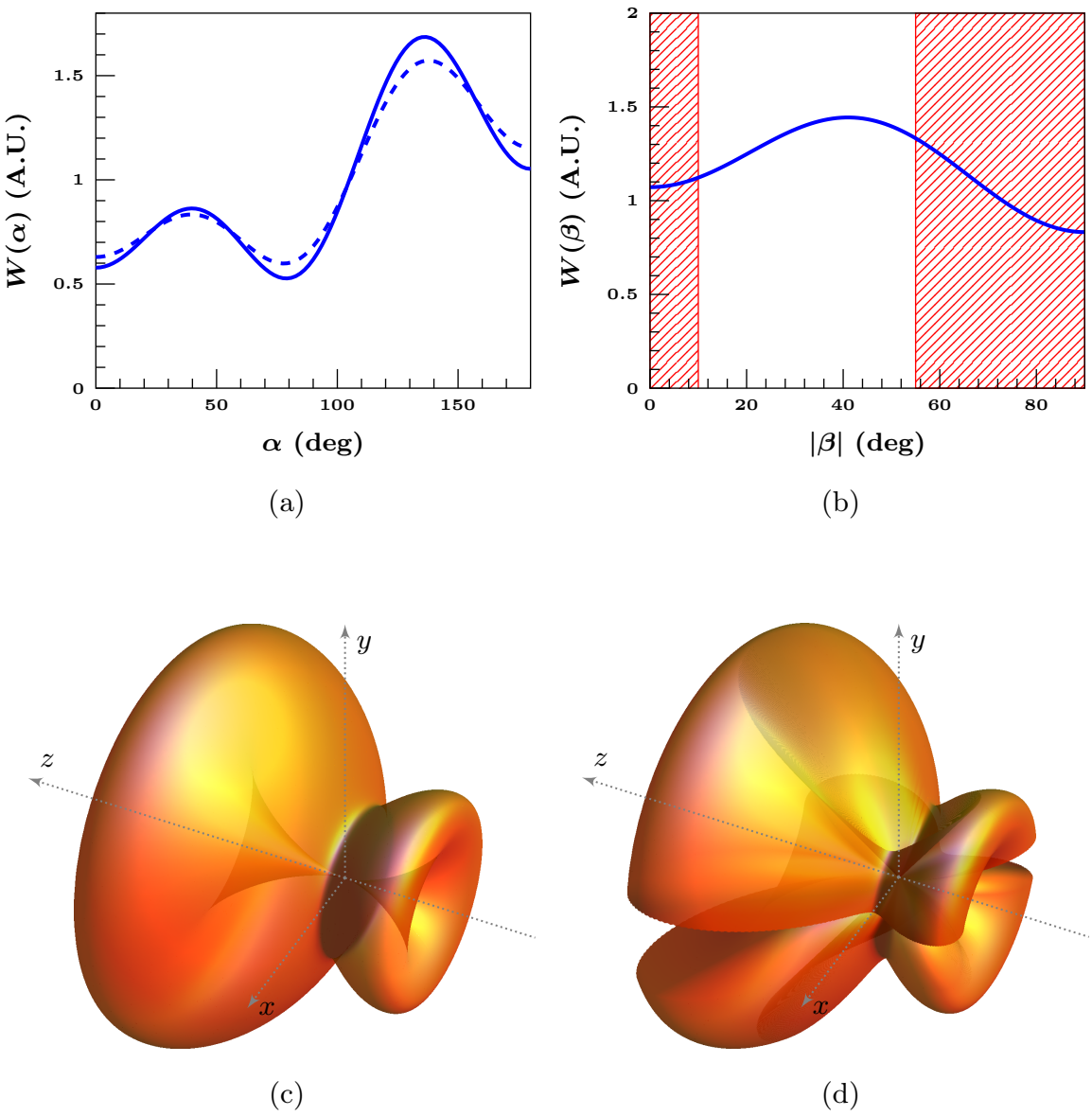

Figure 4.26: (a) Distribution of the in-plane angle α before (dashed blue curve) and after (solid blue curve) the fiducial cuts in β. (b) Distribution of β. The fiducial cuts are shown by the hashed red regions. (c) Three-dimensional surface representing the angular distribution before the fiducial cuts in β. (d) Three-dimensional surface representing the angular distribution after the fiducial cuts in β.

Carlo statistical uncertainty was negligible. This efficiency was used along with the total number of recorded ^{12}C(γ,α_0)^{8}Be events to determine the total cross section at each γ-ray beam energy.

Figure 4.26 shows the effect of the fiducial cuts in the out-of-plane angle β based on the angular distribution measured at a beam energy of 10.8 MeV. The cuts require $10^\circ \leq |\beta| \leq 55^\circ$, and the calculated efficiency of these cuts is 56.4 %. Figures 4.26c and 4.26d show three-dimensional surfaces representing the angular distribution before and after the cuts in β. The probability for an outgoing α particle to be emitted at an angle is proportional to the distance between the origin and the surface at that angle. The condition requiring $|\beta| \leq 55^\circ$ excludes a cone around the y-axis, and the condition requiring $|\beta| \geq 10^\circ$ excludes a slice around the xz-plane.

Chapter 5

Results & Discussion

5.1 Experimental Results

5.1.1 Absolute Cross Sections

In order to extract the parameters from the 1^-_1 and 2^+_2 states in ^{12}C, the absolute cross sections must be calculated as well as their $E1$ and $E2$ components at each γ-ray beam energy. This was accomplished using the beam intensity results described in Section 4.1.1, events identified as ^{12}C(γ,α_0)^{8}Be using the technique discussed in Section 4.3.4, and the results from the fits to the angular distributions described in Section 4.4.

Integrated Luminosity

The overall normalization of the cross section data was obtained by calculating the time-integrated effective luminosity:

$$\mathscr{L}_{\text{eff}} = N_\gamma \, T_{\text{tgt}} \, \frac{t_{\text{live}}}{t}, \tag{5.1}$$

where N_γ is the total number of photons incident on the target, T_{tgt} is the target thickness, and $\frac{t_{\text{live}}}{t}$ is live-time fraction of the detector. As discussed in Sections 3.2.1 and 4.1.1, the beam intensity was determined with relative and absolute measurements using several detectors. N_γ was determined separately for each run using the scaler signal from the relative intensity monitors. The live-time fraction was calcu-

lated by comparing the scaler counts of the random pulser with the vetoed counts of the same pulser (Section 3.4).

σ_{E1} & σ_{E2}

The $E1$ and $E2$ components of the angle-integrated cross section were calculated for each γ-ray beam energy from the total ^{12}C(γ,α_0)^{8}Be cross section at each energy:

$$\sigma_{\text{TOT}} = \frac{N_{^{12}\text{C}}\,(1 - f_{^{16}\text{O}})}{\mathscr{L}_{\text{eff}}\ \epsilon_{\text{fid}}\ \epsilon_{\chi^2}}, \tag{5.2}$$

where $N_{^{12}\text{C}}$ is the total number of ^{12}C(γ,α_0)^{8}Be events which were not excluded by any of the cuts, $f_{^{16}\text{O}}$ is the fractional leakage of ^{16}O(γ,α)^{12}C events past the cut in A_{χ^2} (Section 4.3.4), $\mathscr{L}_{\text{eff}}$ is the time-integrated effective luminosity, and ϵ_{fid} and ϵ_{χ^2} are the efficiencies of the fiducial cut in β and in A_{χ^2}, described in Sections 4.4.3 and 4.3.4, respectively. Apart from these cut efficiencies and the detector live time, it is assumed that all ^{12}C(γ,α_0)^{8}Be events which occurred inside the active volume of the detector were recorded.

The individual $E1$ and $E2$ components of the total cross section were calculated using the ratio of the amplitudes $\frac{|E2|}{|E1|}$ which was extracted from the fits to the angular distributions (Section 4.4):

$$\sigma_{E1} = \sigma_{\text{TOT}} \frac{1}{\frac{5}{3}\left(\frac{|E2|}{|E1|}\right)^2 + 1} \qquad \sigma_{E2} = \sigma_{\text{TOT}} \frac{\frac{5}{3}\left(\frac{|E2|}{|E1|}\right)^2}{\frac{5}{3}\left(\frac{|E2|}{|E1|}\right)^2 + 1} \tag{5.3}$$

5.1.2 Propagation of Uncertainties

The uncertainties shown in the experimental results include contributions from both statistical and systematic uncertainties. Uncertainties affecting ϕ_{12}, the total

cross section, and the $E1$ and $E2$ components are described below.

Statistical

$N_{^{12}C}$: The statistical uncertainty in the number of recorded $^{12}C(\gamma,\alpha_0)^8Be$ events was taken to be equal to $\sqrt{N_{^{12}C}}$. This uncertainty follows a symmetric Gaussian distribution.

$\frac{|E2|}{|E1|}$, ϕ_{12}: The uncertainties in $\frac{|E2|}{|E1|}$ and ϕ_{12} are purely statistical and were calculated using the change in the log-likelihood in the fits to the angular distributions according to Equation 4.13. These uncertainties are generally asymmetric and were approximated as two Gaussian distributions of different widths: one for the positive error and one for the negative error (Figure 5.1).

Systematic

Each of the following sources of systematic uncertainties affects each data point individually.

ϵ_{fid} (2–4 %): The uncertainties in the efficiencies of the fiducial cuts in the out-of-plane angle β (see Section 4.4.3) were estimated using the uncertainties in the angular distribution fit parameter $\frac{|E2|}{|E1|}$. ϕ_{12}, the second angular distribution fit parameter, affects only the fore-aft asymmetry of the angular distributions and has no effect on ϵ_{fid}. Uncertainties in ϵ_{fid} were estimated for each beam energy by calculating ϵ_{fid} using the $\pm1\sigma$ values of $\frac{|E2|}{|E1|}$ taken from the fits to the angular distributions. These uncertainties were generally 2–4 %. Changes to the fiducial cuts in β resulted in calculated total cross sections which varied within these uncertainties.

ϵ_{χ^2} (5 %): The relative uncertainties in the efficiencies of the cuts in A_{χ^2} (see Section 4.3.4) were estimated to be 5 % by varying the position of the cut and calculating the resulting total cross section.

$f_{^{16}\mathrm{O}}$ (5 %): The uncertainties in the ^{16}O leakage (see Section 4.3.4) were essentially the same as those for ϵ_{χ^2}. They were estimated to be 5 % by varying the position of the cut in A_{χ^2}, but since $f_{^{16}\mathrm{O}}$ was always less than 0.005, the resulting uncertainties in the cross section due to the uncertainty in $f_{^{16}\mathrm{O}}$ were negligible.

N_γ (5 %): The beam intensity was measured using several relative measurements (run concurrently with the experiment) calibrated against absolute measurements performed several times during each beam energy (see Section 4.1.1). The uncertainty in the calibration of of the relative measurements was estimated to be 3 % using the variations in the calibrations across each beam energy, and by comparing the agreement of the different relative measurements. The uncertainty in the absolute measurements was estimated to be 4 %. This was dominated by the uncertainties in the attenuation factors of the copper attenuators, which were estimated by comparing the published values [Ber98] with those calculated by comparing beam intensities measured with different combinations of the copper attenuators reducing the beam. The total uncertainty in the beam intensity was calculated to be 5 % by combining the uncertainties from the relative and absolute measurements in quadrature.

T_{tgt} (0.6 %): The uncertainties in the target thickness include contributions from: (i) The concentration of CO_2 in the target gas. This was measured by the manufacturer using gas chromatography with an uncertainty of 0.05 %. (ii) The temperature of the target gas, which was assumed to be same as the ambient room temperature. This was measured throughout the experiment; the average

variation was 1 °C, which corresponds to a variation in target thickness of 0.3 %. (iii) The abundance of ^{12}C in natural carbon. The published value for the natural abundance of ^{12}C is 98.945(92) % [Böh05], with uncertainties given by the natural variations in the isotope ratios. (iv) Fiducial target length. Events were only accepted which occurred inside of a region defined by this length, 200 mm and 180 mm for the 100 torr and 150 torr runs, respectively. The length calibration of the camera is accurate to 1 mm, leading to a 0.5 % uncertainty in the target thickness. These uncertainties were added in quadrature to give a 0.6 % uncertainty in target thickness.

$\frac{t_{live}}{t}$ (< 0.01 %): The live time was measured using a 1 kHz random pulser whose signal was either recorded as a live pulse if the DAQ was live or as a dead pulse if it was not (see Section 3.4). The live time is the ratio of live pulses to total pulses, and the uncertainty in the live time was calculated at each beam energy from the total number of live and total pulses. The rate of the random pulser was chosen such that the uncertainty in the live time was negligible.

$\mathscr{L}_{\mathrm{eff}}$: The errors in N_γ, $\frac{t_{\mathrm{live}}}{t}$, and T_{tgt} were combined in quadrature to generate the uncertainty in $\mathscr{L}_{\mathrm{eff}}$ which was used to calculate σ_{TOT} and its corresponding error.

Beam Energy (20 keV): The uncertainties in the beam energy distribution centroids were estimated by comparing the results from the various methods of extracting the centroids from the HPGe spectra (see Section 4.1.2), and including a 10 keV uncertainty due to the calibration of the HPGe detector. These uncertainties were added in quadrature to give 20 keV.

Total ^{12}C(γ,α_0)^{8}Be Cross Section

The uncertainties in the total ^{12}C(γ,α_0)^{8}Be cross sections were calculated by summing all of the known statistical and systematic uncertainties in quadrature. The uncertainties are asymmetric; the negative and positive errors were calculated separately. The total ^{12}C(γ,α_0)^{8}Be cross sections and the corresponding uncertainties for each γ-ray beam energy are shown in Figure 5.3b and listed in Table 5.1.

Propagation of Uncertainties to σ_{E1} & σ_{E2}

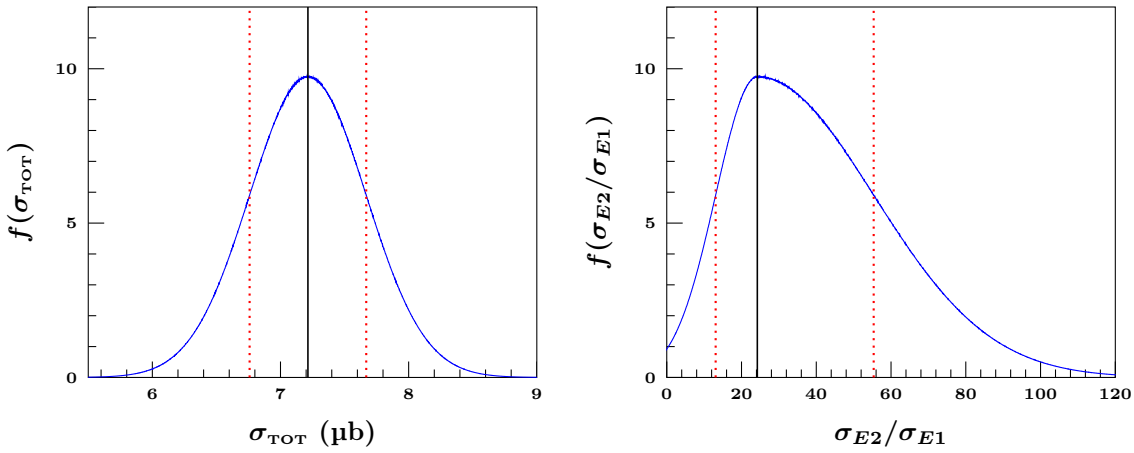

Figure 5.1: Generated probability distributions for $\sigma_{\rm TOT}$ and σ_{E2}/σ_{E1} at a beam energy of 10.05 MeV based on the asymmetric uncertainties from the fit to the angular distributions. The black solid lines show the most likely value, and the dotted red lines show the 68.3 % confidence level values.

The $E1$ and $E2$ cross section components are related non-linearly to $\sigma_{\rm TOT}$ and $\frac{|E2|}{|E1|}$ (Equation 5.3), so the propagation of the asymmetric uncertainties is non-trivial. As shown in Figure 5.1, the probability distributions of $\sigma_{\rm TOT}$ and $\frac{|E2|}{|E1|}$ were taken to be Gaussian functions with separate widths on either side of the peak corresponding to the measured negative and positive uncertainties.

In general, if a parameter $y = Y(x_1, x_2, \ldots)$ is a function of the independent random variables $x_1, x_2, \ldots$, then the probability distribution of y is related to the

the distributions of $x_1, x_2, \ldots$:

$$f(y) = \int dx_1\, dx_2 \ldots\ \delta\Big(y - Y(x_1, x_2, \ldots)\Big) f(x_1)\, f(x_2) \ldots, \tag{5.4}$$

where $f()$ represents the probability distribution of each of the parameters [Ago03]. Using Equation 5.3 in Equation 5.4, the distributions of the $E1$ and $E2$ cross section components are given by:

$$\begin{aligned} f(\sigma_{E1}) &= \int dR\, d\sigma_{\text{TOT}}\ \delta\Big(\sigma_{E1} - \frac{\sigma_{\text{TOT}}}{R+1}\Big)\ f_\sigma\big(\sigma_{\text{TOT}}\big)\ f_R\big(R\big) \\ &= \int dR\ \big(R+1\big)\ f_\sigma\Big(\sigma_{E1}\,(R+1)\Big)\ f_R\big(R\big) \end{aligned} \tag{5.5}$$

$$\begin{aligned} f(\sigma_{E2}) &= \int dR\, d\sigma_{\text{TOT}}\ \delta\Big(\sigma_{E2} - \frac{R\,\sigma_{\text{TOT}}}{R+1}\Big)\ f_\sigma\big(\sigma_{\text{TOT}}\big)\ f_R\big(R\big) \\ &= \int dR\ \left(\frac{R+1}{R}\right)\ f_\sigma\left(\sigma_{E2}\frac{R+1}{R}\right)\ f_R\big(R\big), \end{aligned} \tag{5.6}$$

where $R = \frac{5}{3}\left(\frac{|E2|}{|E1|}\right)^2$ is the ratio of σ_{E2} to σ_{E1}.

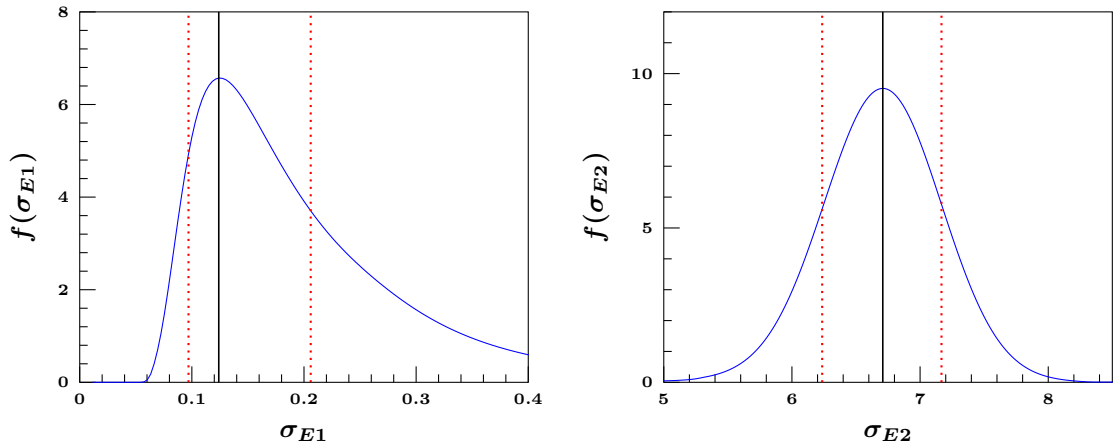

Figure 5.2: Propagation of asymmetric uncertainties to σ_{E1} and σ_{E2} at a beam energy of 10.05 MeV obtained by numerically integrating Equations 5.5 and 5.6 using the distributions shown in Figure 5.1. The black solid lines show the most likely value, and the dotted red lines show the 68.3 % confidence level values.

For each γ-ray beam energy, σ_{E1}, σ_{E2}, and their corresponding uncertainties were calculated by numerically integrating Equations 5.5 and 5.6. The resulting distributions in σ_{E1} and σ_{E2} were asymmetric and non-Gaussian, so the adopted values were defined to be the peaks of the distributions, and the uncertainties were defined to include 68.3 % of the total distributions. Figure 5.2 shows an example of the uncertainties in σ_{E1} and σ_{E2} propagated through numerical integration. σ_{E1}, σ_{E2} and the corresponding uncertainties for each γ-ray beam energy are shown in Figure 5.3b and listed in Table 5.1.

5.1.3 Results

The total cross sections, the $E1$ and $E2$ cross section components, the $E1-E2$ phase differences, and the ratios of $E2$ to $E1$ amplitudes for the ^{12}C(γ,α_0)^{8}Be reaction are shown in Figure 5.3 and listed in tabular form in Table 5.1. The calculation of the total cross section as well as its $E1$ and $E2$ components was described in Section 5.1.1. The $E1-E2$ phase differences were extracted directly from the fits to the angular distributions as discussed in Section 4.4.

The γ-ray beam energy E_γ in Figure 5.3 and Table 5.1 refers to the centroid of the γ-ray beam energy distributions, and the results are averaged over that distribution. The convolution of the results with the beam energy distribution is accounted for in the resonance fit functions, discussed in Sections 5.2.1 and 5.2.2.

5.2 Resonance Fit

The resonance parameters from the 1^-_1 and 2^+_2 states were extracted by fitting the experimental results listed in Table 5.2. For each resonance, there are three free parameters: the resonance energy $E_{\rm RES}$, the α-decay partial width on resonance

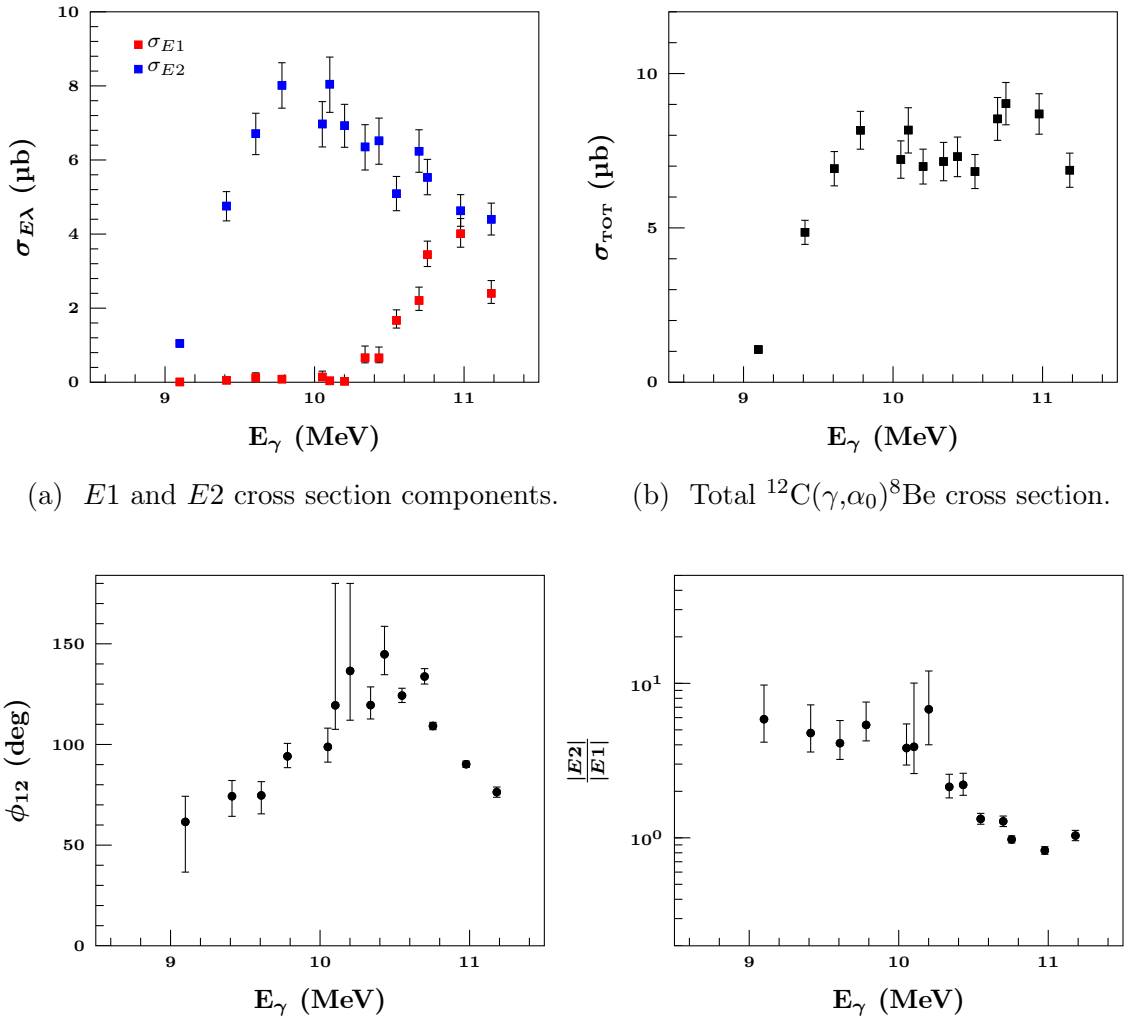

(a) $E1$ and $E2$ cross section components.

(b) Total $^{12}C(\gamma,\alpha_0)^8Be$ cross section.

(c) $E1-E2$ phase.

(d) Ratio of $E2$ to $E1$ amplitudes.

Figure 5.3: Measured cross sections and $E1-E2$ phase differences and amplitude ratios. E_γ refers to to the centroid of the γ-ray beam energy distribution, and the results shown are averaged over that distribution. The error bars associated with each data point represent the total uncertainty, both statistical and systematic.

$\Gamma_\alpha(E_{\rm RES})$, and the γ-decay partial width on resonance $\Gamma_\gamma(E_{\rm RES})$.

Table 5.1: Measured cross sections and $E1-E2$ phase differences and amplitude ratios. E_γ refers to to the centroid of the γ-ray beam energy distribution, and the results shown are averaged over that distribution. The listed uncertainties represent the total uncertainty, both statistical and systematic.

E_γ (keV)	σ_{E1} (μb)	σ_{E2} (μb)	σ_{TOT} (μb)	ϕ_{12} (deg)	$\frac{\lvert E2\rvert}{\lvert E1\rvert}$
9.099(20)	$0.008^{+0.009}_{-0.003}$	$1.048^{+0.085}_{-0.092}$	$1.061^{+0.087}_{-0.088}$	$61.5^{+12.7}_{-24.9}$	$5.859^{+5.786}_{-1.698}$
9.411(20)	$0.053^{+0.070}_{-0.015}$	$4.756^{+0.391}_{-0.400}$	$4.858^{+0.389}_{-0.391}$	$74.3^{+7.8}_{-10.0}$	$4.769^{+3.752}_{-1.175}$
9.607(20)	$0.124^{+0.131}_{-0.031}$	$6.709^{+0.552}_{-0.565}$	$6.919^{+0.554}_{-0.556}$	$74.7^{+6.8}_{-9.1}$	$4.101^{+2.519}_{-0.883}$
9.782(20)	$0.084^{+0.092}_{-0.021}$	$8.015^{+0.610}_{-0.616}$	$8.163^{+0.612}_{-0.613}$	$94.1^{+6.4}_{-5.6}$	$5.379^{+3.345}_{-1.138}$
10.052(20)	$0.142^{+0.159}_{-0.037}$	$6.972^{+0.604}_{-0.620}$	$7.214^{+0.606}_{-0.606}$	$98.8^{+9.3}_{-7.6}$	$3.813^{+2.512}_{-0.854}$
10.102(20)	$0.038^{+0.092}_{-0.012}$	$8.046^{+0.732}_{-0.760}$	$8.169^{+0.723}_{-0.742}$	$119.4^{+60.6}_{-11.9}$	$3.884^{+8.688}_{-1.277}$
10.201(20)	$0.026^{+0.049}_{-0.009}$	$6.926^{+0.577}_{-0.583}$	$6.988^{+0.563}_{-0.567}$	$136.5^{+43.5}_{-24.5}$	$6.790^{+7.706}_{-2.788}$
10.338(20)	$0.661^{+0.317}_{-0.137}$	$6.352^{+0.601}_{-0.623}$	$7.150^{+0.620}_{-0.623}$	$119.6^{+9.1}_{-6.9}$	$2.137^{+0.698}_{-0.323}$
10.431(20)	$0.658^{+0.293}_{-0.131}$	$6.517^{+0.613}_{-0.632}$	$7.308^{+0.635}_{-0.647}$	$144.8^{+13.9}_{-10.1}$	$2.204^{+0.657}_{-0.319}$
10.548(20)	$1.671^{+0.284}_{-0.208}$	$5.089^{+0.467}_{-0.458}$	$6.826^{+0.551}_{-0.551}$	$124.3^{+3.6}_{-3.4}$	$1.326^{+0.185}_{-0.102}$
10.699(20)	$2.208^{+0.360}_{-0.269}$	$6.236^{+0.580}_{-0.568}$	$8.531^{+0.693}_{-0.696}$	$133.7^{+3.9}_{-3.7}$	$1.279^{+0.171}_{-0.095}$
10.755(20)	$3.444^{+0.366}_{-0.320}$	$5.531^{+0.485}_{-0.470}$	$9.025^{+0.685}_{-0.685}$	$109.2^{+1.8}_{-1.8}$	$0.976^{+0.086}_{-0.050}$
10.977(20)	$4.008^{+0.412}_{-0.363}$	$4.628^{+0.436}_{-0.418}$	$8.691^{+0.656}_{-0.655}$	$90.2^{+1.6}_{-1.6}$	$0.828^{+0.078}_{-0.045}$
11.182(20)	$2.400^{+0.345}_{-0.272}$	$4.399^{+0.436}_{-0.424}$	$6.869^{+0.553}_{-0.553}$	$76.3^{+2.5}_{-2.6}$	$1.034^{+0.135}_{-0.076}$

5.2.1 Cross Sections

In general, the resonance cross section for a (γ, α_0) reaction on a $J^\pi = 0^+$ nucleus is given by [Lan58, Des10]:

$$\sigma(E_\gamma) = \frac{\pi}{k^2} \, \frac{2J+1}{2} \, \frac{\Gamma_\alpha \Gamma_\gamma}{\left(E_{\mathrm{RES}} - E_\gamma\right)^2 + \frac{1}{4}\Gamma^2} \tag{5.7}$$

for a resonance at energy E_{RES} with angular momentum J, total width Γ, and partial widths Γ_α and Γ_γ. Equivalent expressions were used to extract the parameters of the 2_2^+ state in ^{12}C in previous inelastic scattering experiments [Fre09, Zim11, Fre12b]. In the present case only the α and γ channels are open. Since $\Gamma_\gamma \ll \Gamma_\alpha$, Γ is taken to be equal to Γ_α in this case. The energy dependence of the partial widths is [Bla52]:

$$\frac{\Gamma_\alpha(E_\gamma)}{\Gamma_\alpha(E_{\mathrm{RES}})} = \frac{P_\ell(E_\gamma - Q)}{P_\ell(E_{\mathrm{RES}} - Q)} \qquad\qquad \frac{\Gamma_\gamma(E_\gamma)}{\Gamma_\gamma(E_{\mathrm{RES}})} = \left(\frac{E_\gamma}{E_{\mathrm{RES}}}\right)^{2J+1} \tag{5.8}$$

The penetrability P_ℓ is defined as [Lan58]:

$$P_\ell = \frac{kR}{F_\ell^2 + G_\ell^2}, \tag{5.9}$$

where R is the channel radius, taken to be $r_0(4^{\frac{1}{3}} + 8^{\frac{1}{3}})$ with r_0 fixed at 1.4 fm, and ℓ is the orbital angular momentum in the $\alpha + {}^8$Be system. F_ℓ and G_ℓ are the regular and irregular Coulomb wave functions, solutions to the Coulomb wave equation [Abr64]. F_ℓ and G_ℓ were calculated using the continued-fraction expansion method [Bar74].

Convolution

The cross sections measured in this experiment include the influence from the energy spread of the γ-ray beam. This effect must be included in the fit function

describing the resonance cross section in order for accurate resonance parameters to be extracted. The effect of the energy spread can be calculated by convolving the underlying cross section with the energy distribution of the beam. The beam was measured (Section 3.2) to follow a Gaussian distribution, so the fit function describing the measured cross sections becomes:

$$\Big[\sigma(E_\gamma)\Big]_{\text{measured}} = \int dE'\ \sigma(E')\ \frac{1}{\sqrt{2\pi}\sigma_\gamma}\ e^{-\frac{(E'-E_\gamma)^2}{2\sigma_\gamma^2}}, \tag{5.10}$$

where $\sigma(E')$ is the underlying cross section given in Equation 5.7, and σ_γ describes the energy spread of the γ-ray beam.

5.2.2 Phase Difference

The phase difference ϕ_{12} for interacting $E1$ and $E2$ radiation and spinless particles is given by [Dye74]:

$$\phi_{12} = \delta_2 - \delta_1 + \tan^{-1}\left(\frac{\eta}{2}\right), \tag{5.11}$$

where δ_1 and δ_2 are the $E1$ and $E2$ phases, and η is the Sommerfeld parameter defined as:

$$\eta = \frac{\alpha}{\hbar c}\ \frac{Z_1 Z_2 \mu}{k}. \tag{5.12}$$

Using the single-level approximation [Lan58], the individual $E1$ and $E2$ phases can be written as:

$$\delta_\ell = \tan^{-1}\left(\frac{\Gamma}{2\left(E_{\text{RES}} - E_\gamma\right)}\right) - \tan^{-1}\left(\frac{F_\ell}{G_\ell}\right) \tag{5.13}$$

The first term in Equation 5.13 is the phase of a Breit-Wigner term, and the second term is the hard-sphere scattering contribution.

Convolution

Like the fit function for the cross section, the function for ϕ_{12} must include the effect of a finite beam width. For a given γ-ray beam energy, the measured value of $\cos\phi_{12}$ is convolved with the beam energy distribution weighted by the total cross section:

$$\Big[\cos\phi(E_\gamma)\Big]_{\text{measured}} = \frac{\int dE'\ \cos\phi_{12}(E')\,\sigma_{\text{TOT}}(E')\,\frac{1}{\sqrt{2\pi}\sigma_\gamma}\,e^{-\frac{(E_\gamma-E')^2}{2\sigma_\gamma^2}}}{\int dE'\ \sigma_{\text{TOT}}(E')\,\frac{1}{\sqrt{2\pi}\sigma_\gamma}\,e^{-\frac{(E_\gamma-E')^2}{2\sigma_\gamma^2}}} \tag{5.14}$$

5.2.3 Fitting Process

Fits to σ_{E1} & σ_{E2}

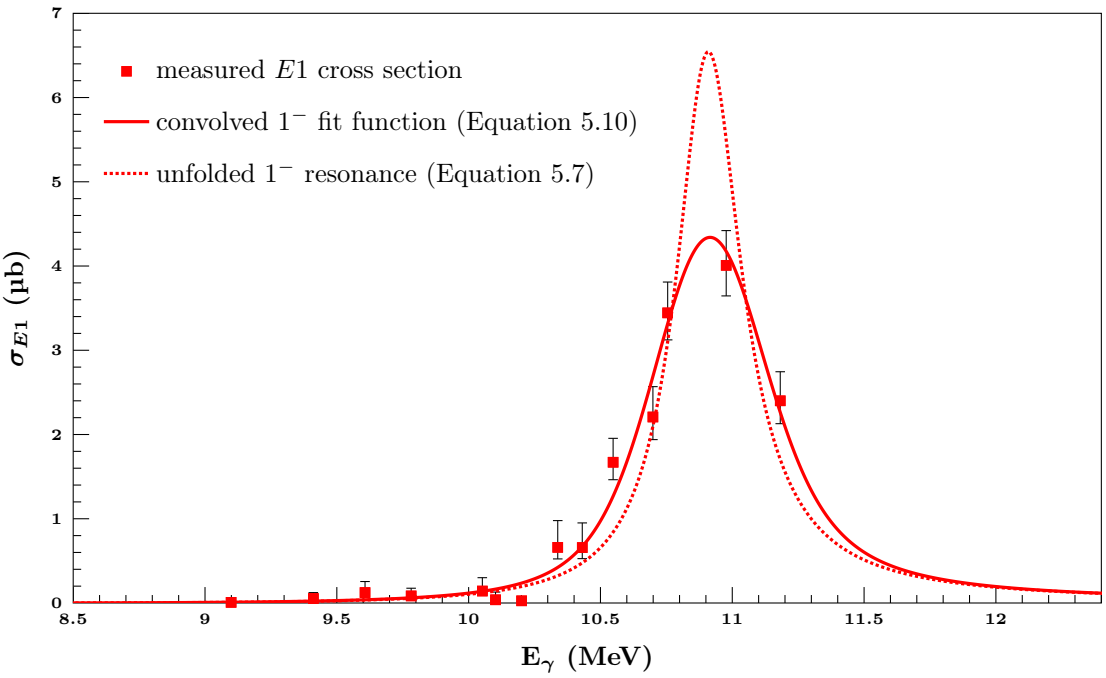

Figure 5.4: The $E1$ cross section data as a function of beam energy are shown along with the fit to to σ_{E1} data used to extract the 1_1^- resonance parameters. Both the convolved and unfolded cross section line shapes are shown. The results of the fit are listed in Table 5.2.

Parameters for the 1^-_1 and 2^+_2 resonances were extracted by fitting the $E1$ and $E2$ cross section components using Equation 5.10. In both cases, the resonance energy $E_{\rm RES}$, the α-decay width on resonance $\Gamma_\alpha(E_{\rm RES})$, and the γ-decay width on resonance $\Gamma_\gamma(E_{\rm RES})$ were varied to minimize χ^2. Figures 5.4 and 5.5 show the fits to the σ_{E1} and σ_{E2} data, respectively. The results of the fits are listed in Table 5.2.

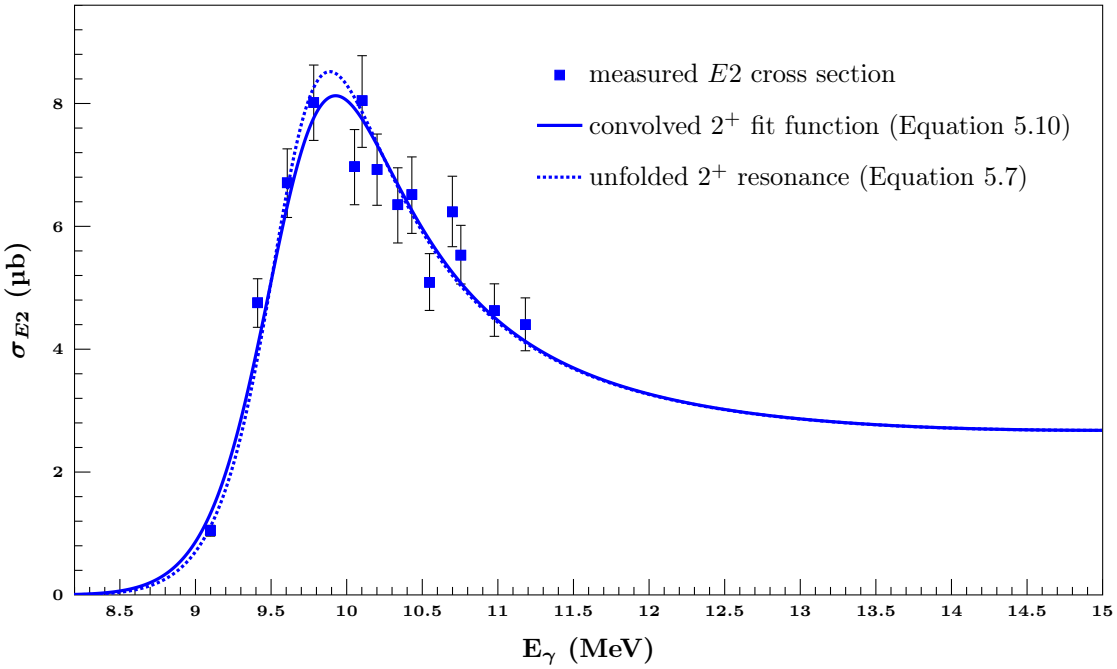

Figure 5.5: The $E2$ cross section data as a function of beam energy are shown along with the fit to to σ_{E2} data used to extract the 2^+_2 resonance parameters. Both the convolved and unfolded cross section line shapes are shown. The results of the fit are listed in Table 5.2.

The $E1$–$E2$ phase angle ϕ_{12} was calculated as a function of energy using Equation 5.14 and the resonance parameters from the fits to the $E1$ and $E2$ cross section components. Figure 5.6 shows the results of the calculation along with the measured values of ϕ_{12}. The calculated values of ϕ_{12} assumes the existence of the 1^-_1 and 2^+_2 states with parameters listed in Table 5.2, and the agreement between the calculated and measured values of ϕ_{12} firmly establishes the resonance nature of the 2^+ strength measured in this experiment.

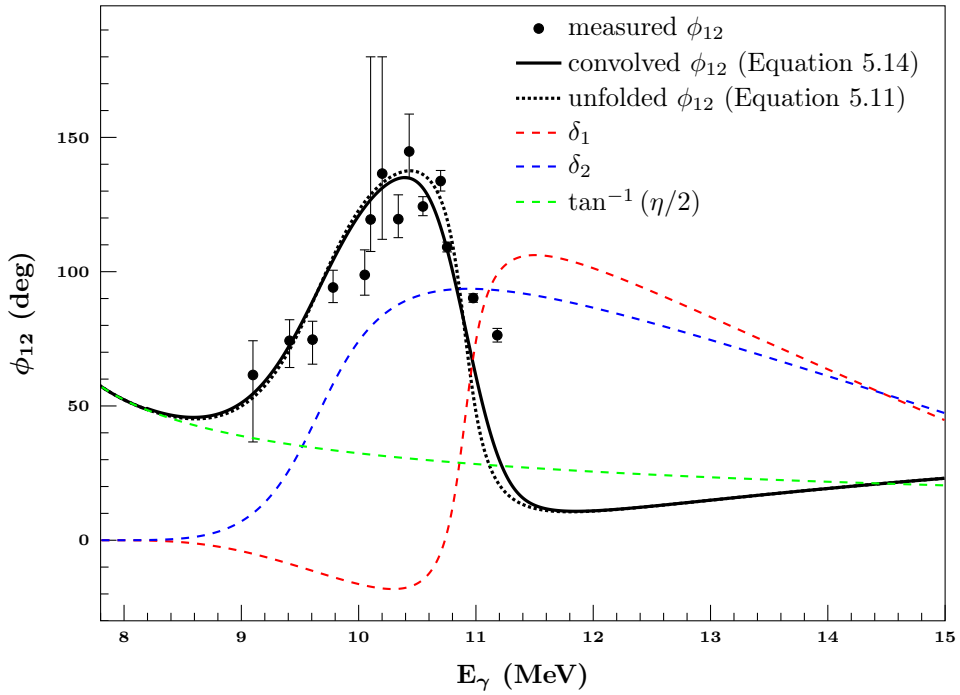

Figure 5.6: Measured values of the $E1$–$E2$ phase angle ϕ_{12} along with a calculation of ϕ_{12} according to the resonance parameters listed in Table 5.2.

The function used to calculate ϕ_{12} (Equation 5.14) does not take into account any $E2$ amplitudes other than the 2_2^+ resonance. This may be the reason for the discrepancy between the two highest energy ϕ_{12} data points and the calculated curve; the last two data points are farthest from the 2_2^+ resonance and are the most susceptible to influences from distant $E2$ amplitudes.

5.2.4 Results

Reduced α-Decay Widths

The reduced α-decay width γ_α^2 is defined as [Bla52]:

$$\gamma_\alpha^2 = \frac{\Gamma_\alpha}{2P_\ell}, \tag{5.15}$$

which is a function of both the α-decay width and the resonance energy. γ_α^2 can be expressed either in units of energy, or as a ratio to the Wigner (single-particle) limit [Tei52]:

$$\gamma_{\rm w}^2 = \left(\frac{3}{2}\right) \frac{\hbar^2}{\mu R^2}. \tag{5.16}$$

The reduced α-decay width of the 1_1^- state was calculated to be $82.4^{+10.5}_{-9.5}$ keV or $8.8^{+1.2}_{-1.1}$ % of the Wigner limit, while the reduced α-decay width of the 2_2^+ state was calculated to be 1470^{+160}_{-120} keV or 157(15) % of the Wigner limit. The significance of these results are discussed in detail in Section 5.4.2. Complete results are summarized in Table 5.2, and the determination of the uncertainties is discussed in Section 5.2.5.

Reduced Electromagnetic Transition Probabilities

The γ-decay widths to the ground state can be expressed in terms of the reduced transition probabilities $B(\lambda)$ [Ald56]:

$$(2J_f + 1)\,\Gamma_\gamma = \frac{8\pi(\lambda+1)}{\lambda\Big[(2\lambda+1)!!\Big]^2}\; k^{2\lambda+1}\; B(\lambda) \tag{5.17}$$

for electromagnetic transitions of multipolarity λ to a final state with total angular momentum J_f. The reduced transition probabilities are functions of both the γ-decay width and the resonance energy. The reduced probabilities for the transitions from the 1_1^- and 2_2^+ resonances to the 0^+ ground state in ^{12}C can be expressed either in units of $\mathrm{e^2fm^{2\lambda}}$ or in Weisskopf units [Bla52]:

$$B_{\rm w}(E\lambda) = \frac{(1.2)^{2\lambda}}{4\pi}\; \left(\frac{3}{\lambda+3}\right)^2\; A^{2\lambda/3}\; \mathrm{e^2fm^{2\lambda}}. \tag{5.18}$$

$\mathrm{B}(E1 : 1_1^- \rightarrow 0_1^+)$ was measured to be $4.84(30) \times 10^{-5}\,\mathrm{e^2\ fm^2}$ or $1.43(9) \times 10^{-4}\,\mathrm{W\,u}$, and $\mathrm{B}(E2 : 2_2^+ \rightarrow 0_1^+)$ was measured to be $1.57^{+0.14}_{-0.11}\,\mathrm{e^2\ fm^4}$ or $0.963^{+0.083}_{-0.069}\,\mathrm{W\,u}$. The

complete results from the fits to the $E1$ and $E2$ cross sections are summarized in Table 5.2. The determination of the uncertainties listed in Table 5.2 is discussed in Section 5.2.5.

Table 5.2: Measured 1^-_1 and 2^+_2 resonance parameters from the fits described in Section 5.2.3.

	$E_{\rm RES}$	Γ_α	Γ_γ	γ^2_α		$\mathrm{B}(E\lambda \rightarrow 0^+_1)$	
	(MeV)	(keV)	(meV)	(keV)	$(\gamma^2_\alpha/\gamma^2_{\rm w})$	(e^2 $\mathrm{fm}^{2\lambda}$)	(W.u.)
1^-_1	$10.913^{+0.020}_{-0.018}$	305^{+40}_{-36}	$32.4^{+2.1}_{-2.0}$	$82.4^{+10.5}_{-9.5}$	$0.088^{+0.012}_{-0.011}$	$4.84(30) \times 10^{-5}$	$1.43(9) \times 10^{-4}$
2^+_2	$10.13^{+0.06}_{-0.05}$	2080^{+330}_{-260}	135^{+16}_{-12}	1470^{+160}_{-120}	$1.57^{+0.17}_{-0.13}$	$1.57^{+0.14}_{-0.11}$	$0.963^{+0.083}_{-0.069}$

The value of $E_{\rm RES}$ for the 2^+_2 state listed in Table 5.2 is slightly different from the γ-ray energy associated with the peak in the $E2$ component of the cross section (9.93 MeV). The resonance energy used here is defined [Lan58] as the energy for which the resonance contribution to the phase (first term in Equation 5.13) passes through 90°, and the cross section is defined by the Breit-Wigner formula (Equation 5.7). The peak in the cross section is different from the value of $E_{\rm RES}$ obtained from this formula primarily as a result of the energy dependence of the widths Γ_α and Γ_γ.

A fit of the 2^+_2 state was also attempted using the 'level shift' specified in R-matrix theory [Lan58]. In this approach the term $(E_{\rm RES} - E_\gamma)$ in Equations 5.7 and 5.13 is replaced with $(E_{\rm RES} - E_\gamma + \Delta_\ell)$, where the level shift Δ_ℓ is defined as [Lan58]:

$$\Delta_\ell = -\gamma^2_\alpha \left(S_\ell - B\right), \tag{5.19}$$

and the shift function is given by [Lan58]:

$$S_\ell = P_\ell \left(F_\ell F'_\ell + G_\ell G'_\ell\right), \tag{5.20}$$

where F'_ℓ and G'_ℓ are the derivatives of the Coulomb wavefunctions, and the constant term B is chosen such that Δ_ℓ vanishes when $E_\gamma = E_{\text{RES}}$. R-matrix theory models nuclear resonances using a square-well potential, and the level shift ensures that the internal and external wavefunctions match at the channel radius [Vog62]. This matching—and therefore the internal energy eigenvalues—depend on the energy of the bombarding particle, and that energy dependence is expressed in the level shift.

The effect of the level shift on Equation 5.7 is to narrow the line shape which describes the 2_2^+ resonance cross section by an amount proportional to the reduced width γ_α^2. The larger the reduced width, the stronger the narrowing effect of the level shift, requiring an even larger width in order to fit the data. This results in non-physical fit results ($\Gamma_\alpha \approx 1\,\text{GeV}$; $\text{B}(E2) \approx 500\,\text{W.u.}$) for the parameters of the 2_2^+ state. The level shift was therefore dropped from Equations 5.7 and 5.13, and the results listed in Table 5.2 do not include the effect of the level shift.

R-matrix theory assumes that at most two product nuclei are formed in a reaction, and that all of the final state nuclei are bound [Lan58]. The $^{12}\text{C}(\gamma,\alpha_0)^8\text{Be}$ reaction studied in this experiment results in an unbound ^{8}Be nucleus, contradicting a fundamental assumption used in the formulation of R-matrix theory. This is probably the cause of the failure of the fit to the 2_2^+ state using the level shift.

The energy dependence of Γ_α used to fit the cross section data (Equation 5.8) was also taken from R-matrix theory and matches the experimental data very well; it is responsible for the asymmetric shape of the 2_2^+ state (see Figure 5.5). The agreement between the data and the predicted energy dependence of Γ_α on the one hand, and the failure of the fit using the level shift on the other, may be due to the nature of the final state ^{8}Be nucleus. The ground state of ^{8}Be is unbound, but with a small width of $\Gamma = 5.6\,\text{eV}$ [Til04]. This 'approximately bound' final state is a possible reason for the failure of the fit with the level shift and the agreement of the predicted

energy-dependence of Γ_α.

Dropping the level shift while keeping the energy-dependent particle widths is supported in some recent formulations of R-matrix theory [Des10]. In any event, the resonance parameters presented in this work (Table 5.2) have values such that Equation 5.7 will reproduce the measured cross sections, and Equation 5.11 will reproduce the measured values of ϕ_{12}.

5.2.5 Propagation of Uncertainties

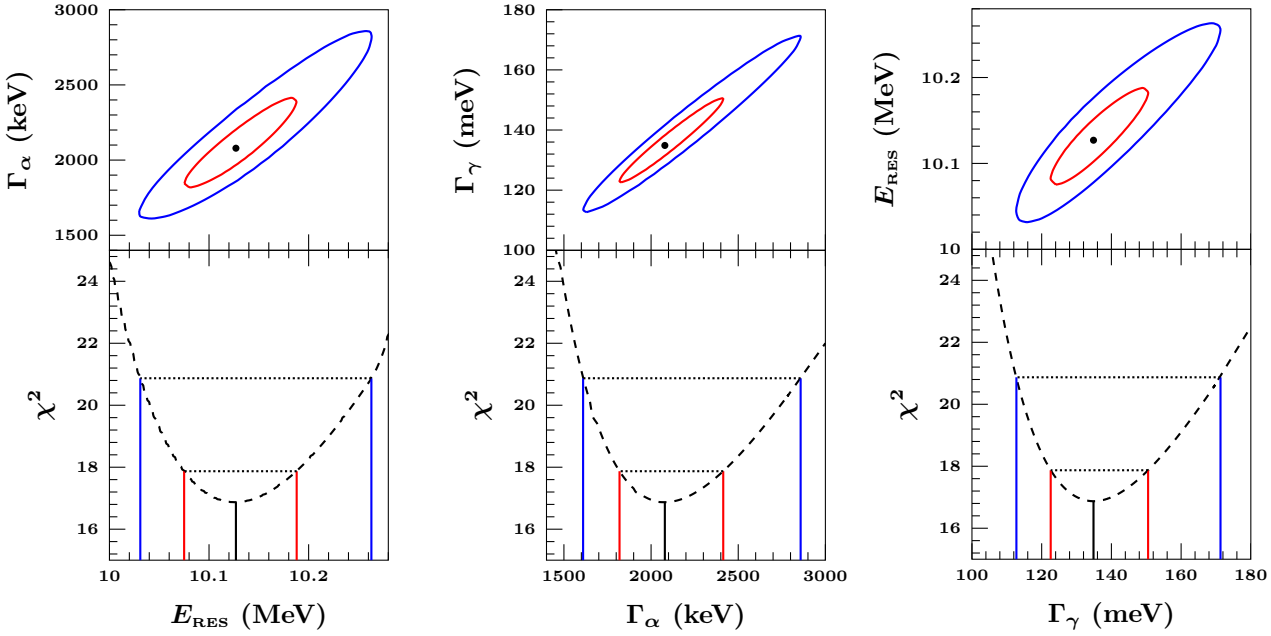

Figure 5.7: Uncertainties and correlations in the extracted 2_2^+ resonance parameters. Top: Correlations between each pair of resonance parameters. The black dots show the best fit values, and red and blue curves show the 68.3 % and 95.4 % confidence levels, respectively. Bottom: The distribution in χ^2 for each resonance parameter (dashed black curves). Each point along the curves is the minimum value of χ^2 calculated for a particular value of E_{RES}, Γ_α, or Γ_γ. The red and blue lines show the 68.3 % and 95.4 % confidence levels, respectively.

The shape of the 2_2^+ resonance (shown in Figure 5.5) is highly asymmetric, with a shape largely defined by the strongly energy-dependent widths (Equation 5.8) due

to the close proximity to the combined Coulomb and centrifugal barrier. This causes correlations in the extracted fit parameters: E_{RES}, Γ_α, and Γ_γ. The correlations were studied by calculating the distribution in χ^2 of the fit to the $E2$ cross section data as a function of the three parameters. E_{RES}, Γ_α, and Γ_γ were each independently varied to give 2×10^8 different combinations, and for each combination the line shape described by Equation 5.10 was calculated, compared with the measured $E2$ cross sections, and the resulting χ^2 was recorded. The 68.3 % and 95.4 % confidence levels for each parameter were calculated where the distributions in χ^2 were 1.0 and 4.0 above the minimum, corresponding to the 1σ and 2σ limits, respectively. This calculation required approximately 100,000 CPU-hours and was performed using the Duke Shared Resource Cluster (DSCR), a 5300-CPU parallel computing environment.

The uncertainties in E_{RES}, Γ_α, and Γ_γ were determined using the extreme values of each parameter for which the total χ^2 was equal to $\chi^2_{\text{MIN}} + 1$ and $\chi^2_{\text{MIN}} + 4$ for the 68.3 % and 95.4 % confidence levels, respectively. Figure 5.7 shows the calculations of the uncertainties in the 2^+_2 resonance parameters from the distribution of χ^2.

The uncertainties in the derived quantities B($E2$) and γ^2_α for the 2^+_2 resonance were also calculated using the complete distribution of χ^2 in order to take into account all correlations and anti-correlations in the resonance parameters. Figure 5.8 shows the calculations of the uncertainties in the derived resonance parameters.

The uncertainties in the 1^-_1 resonance fit parameters were calculated in the same way as those for the 2^+_2 resonance. The 1^-_1 resonance is not nearly as asymmetric or broad as the 2^+_2 resonance, and the fit parameters were not correlated to the same extent. Figure 5.9 shows the calculations of the uncertainties in the 1^-_1 resonance parameters from the distribution of χ^2.

The uncertainties in the derived quantities B($E1$) and γ^2_α for the 1^-_1 resonance were calculated identically as for the 2^+_2 resonance. Figure 5.10 shows the calculations

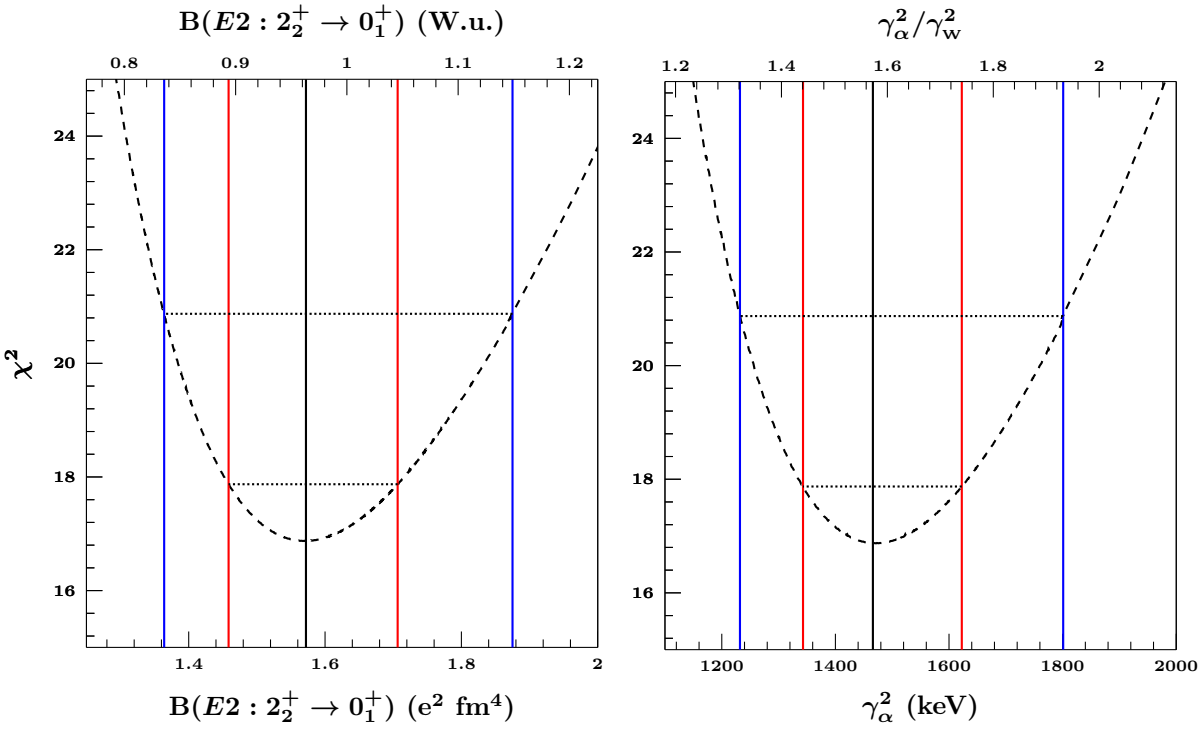

Figure 5.8: Uncertainties in the derived 2_2^+ resonance parameters. The dashed black curves show the distribution in χ^2 as a function of the reduced electromagnetic transition strength B($E2$) and the reduced α-decay width γ_α^2. Each point along the curves is the minimum value of χ^2 calculated for a particular value of B($E2$) and γ_α^2. The black lines show the minimum value of χ^2 and the best fit values. The red and blue lines show the 68.3 % and 95.4 % confidence levels, respectively, where χ^2 is 1.0 and 4.0 above the minimum.

of the uncertainties in the derived resonance parameters.

5.3 Thermonuclear Reaction Rates

5.3.1 Calculation

In general, the total thermonuclear reaction rate r for a two-body reaction is given by [Rol88]:

$$r = N_x N_y \langle \sigma v \rangle, \tag{5.21}$$

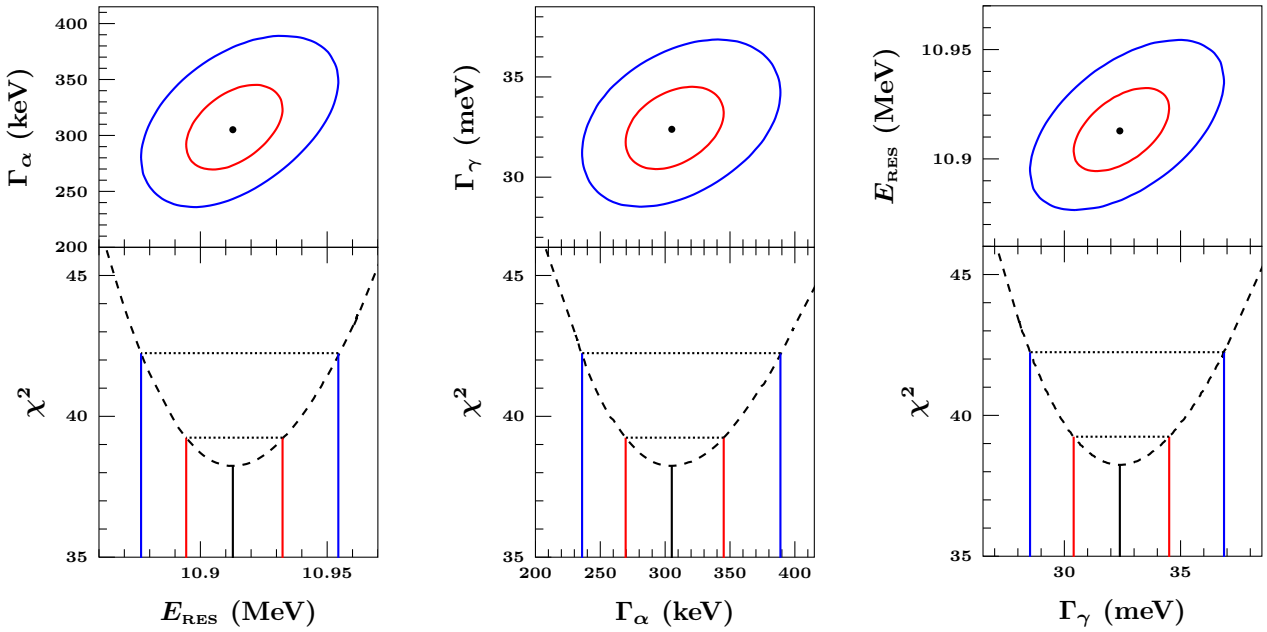

Figure 5.9: Uncertainties and correlations in the extracted 1^-_1 resonance parameters. Top: Correlations between each pair of resonance parameters. The black dots show the best fit values, and red and blue curves show the 68.3 % and 95.4 % confidence levels, respectively. Bottom: The distribution in χ^2 for each resonance parameter (dashed black curves). Each point along the curves is the minimum value of χ^2 calculated for a particular value of $E_{\rm RES}$, Γ_α, or Γ_γ. The red and blue lines show the 68.3 % and 95.4 % confidence levels, respectively.

where N_x and N_y are the densities of the two reacting particles, and $\langle \sigma v \rangle$ is the reaction rate per particle pair, given by the average value of the cross section for the reaction σ times the relative velocity between the particles v. $\langle \sigma v \rangle$ can be calculated in terms of center-of-mass energy by integrating the reaction cross section $\sigma(E)$ weighted by a Maxwell-Boltzmann distribution [Rol88]:

$$\langle \sigma v \rangle = \frac{1}{(kT)^{3/2}} \sqrt{\frac{8}{\mu\pi}} \int_0^\infty dE\, \sigma(E)\, E e^{-E/kT}, \tag{5.22}$$

where T is the temperature, k is the Boltzmann constant, μ is the reduced mass, and E is the energy in the center-of-mass frame. The two-body reaction rate is

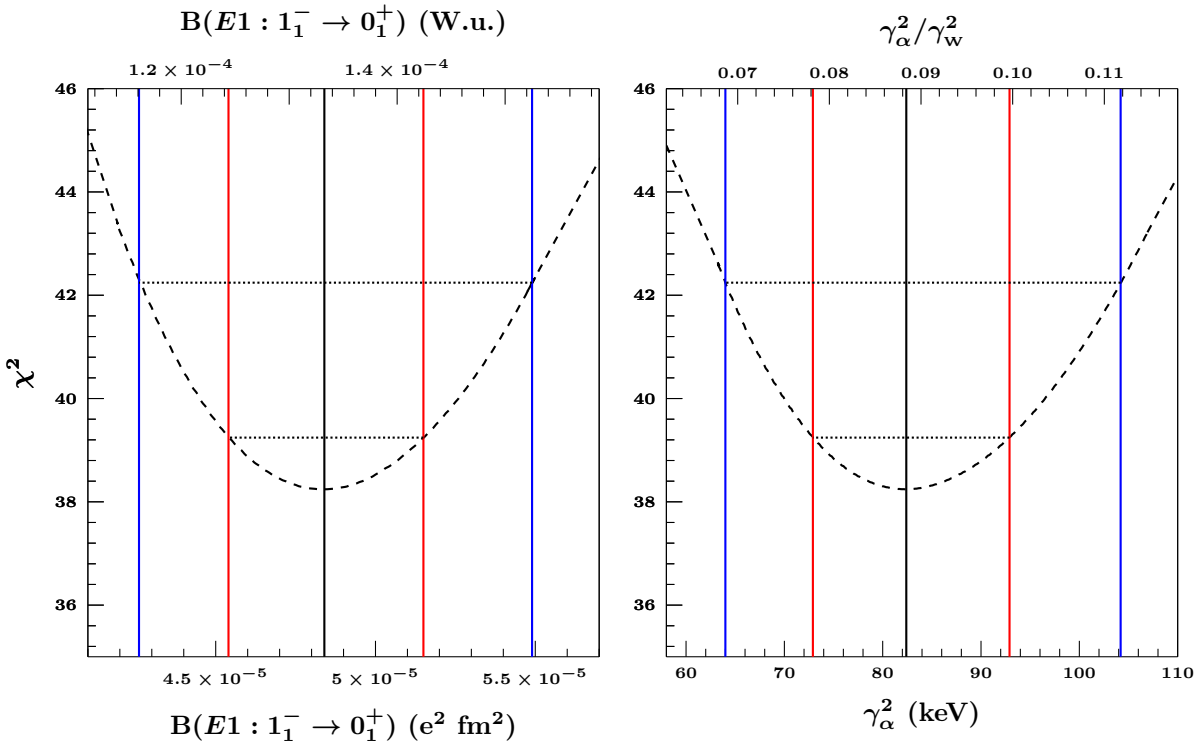

Figure 5.10: Uncertainties in the derived 1^-_1 resonance parameters. The dashed black curves show the distribution in χ^2 as a function of the reduced electromagnetic transition strength B($E1$) and the reduced α-decay width γ^2_α. Each point along the curves is the minimum value of χ^2 calculated for a particular value of B($E1$) and γ^2_α. The black lines show the minimum value of χ^2 and the best fit values. The red and blue lines show the 68.3 % and 95.4 % confidence levels, respectively, where χ^2 is 1.0 and 4.0 above the minimum.

often normalized to the Avogadro constant and written as $N_A\langle\sigma v\rangle$, with units of $\mathrm{cm^3\ mol^{-1}\ s^{-1}}$.

Triple-α reaction rates were calculated according to the formalism presented in the Nuclear Astrophysics Compilation of Reaction Rates (NACRE) [Ang99]. The reaction is assumed to proceed through two distinct steps: (i) two α particles form a ^{8}Be nucleus which (ii) fuses with a third α particle before it decays. The triple-α

reaction rate is given by:

$$N_A^2\langle\sigma v\rangle = 3N_A^2\left(\frac{8\pi\hbar}{\mu_{\alpha\alpha}^2}\right)\left(\frac{\mu_{\alpha\alpha}}{2\pi kT}\right)^{3/2}\int_0^\infty dE\ \frac{\sigma_{\alpha\alpha}(E)}{\Gamma_\alpha(^8\mathrm{Be},E)}Ee^{-E/kT}\langle\alpha^8\mathrm{Be}(E)\rangle, \qquad (5.23)$$

where E is the center-of-mass energy of the original two α particles and $\mu_{\alpha\alpha}$ is their reduced mass. The three-body reaction rate $N_A^2\langle\sigma v\rangle$ has units of $\mathrm{cm}^6\ \mathrm{mol}^{-2}\ \mathrm{s}^{-1}$. The elastic scattering cross section is given by:

$$\sigma_{\alpha\alpha}(E) = \frac{2\pi}{k(E)^2}\frac{\Gamma_\alpha(^8\mathrm{Be};E)^2}{(E-E_{^8\mathrm{Be}})^2+\frac{1}{4}\Gamma_\alpha(^8\mathrm{Be};E)^2}, \qquad (5.24)$$

where $E_{^8\mathrm{Be}}$ is the energy of the ground state of ^{8}Be with respect to the α+α threshold. The $\alpha + {}^8$Be reaction rate $\langle\alpha^8\mathrm{Be}\rangle$ is given by:

$$\langle\alpha^8\mathrm{Be}(E)\rangle = \left(\frac{8\pi\hbar}{\mu_{\alpha^8\mathrm{Be}}^2}\right)\left(\frac{\mu_{\alpha^8\mathrm{Be}}}{2\pi kT}\right)^{3/2}\int_0^\infty dE'\ \sigma_{\alpha^8\mathrm{Be}}(E',E)E'e^{-E'/kT}, \qquad (5.25)$$

where E' is the center-of-mass energy of the $\alpha + {}^8$Be system, $\mu_{\alpha^8\mathrm{Be}}$ is the reduced mass, and $\sigma_{\alpha^8\mathrm{Be}}$ is the ^{8}Be(α,γ)^{12}C cross section which depends on both E and E':

$$\sigma_{\alpha^8\mathrm{Be}}(E',E) = \sum_J \frac{\pi}{k(E')^2}\ \frac{2J+1}{2}\ \frac{\Gamma_\alpha(E')\Gamma_\gamma(E_\gamma)}{\left(E'-E_{\mathrm{R}}(E)\right)^2+\frac{1}{4}\Gamma(E')^2}. \qquad (5.26)$$

The energy-dependence of the widths Γ_α and Γ_γ is discussed in Section 5.2.1.

Figure 5.11 shows the definitions of the various energies used in this calculation. Since the original two α particles have center-of-mass energy E which may be different than the ground-state energy of ^{8}Be, the resonance energy in the α+^{8}Be system must

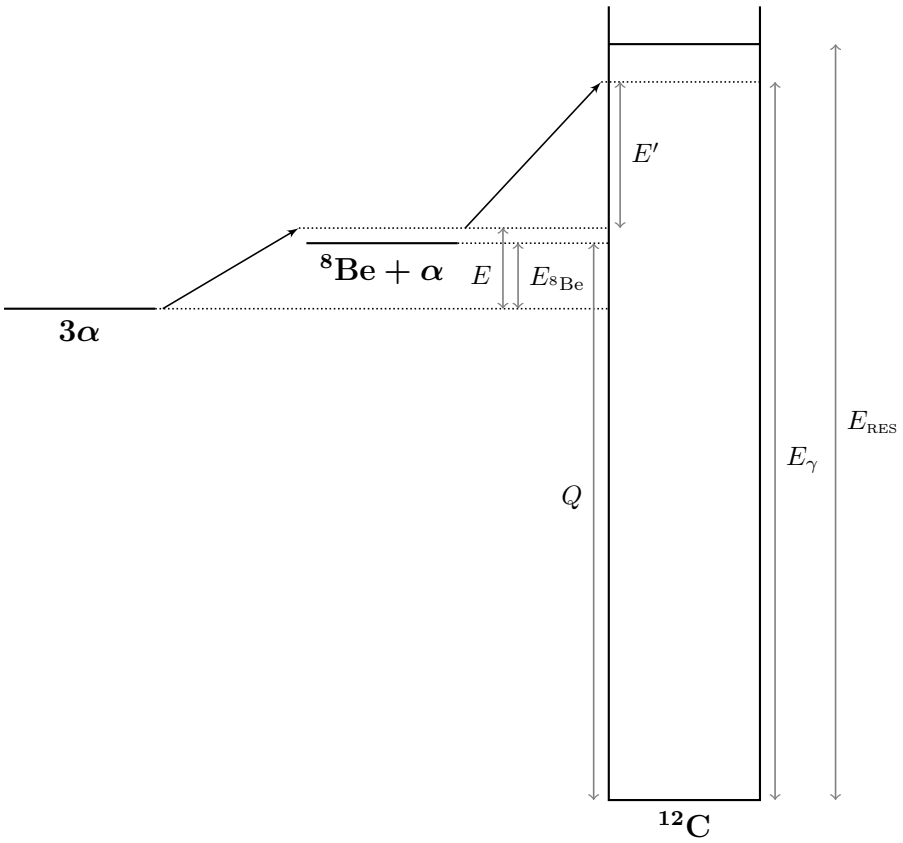

Figure 5.11: Illustration showing the definition of the various energies used in the calculation of the triple-α reaction rates. The figure is not drawn to scale; energy differences are exaggerated for clarity.

be adjusted. The effective resonance energy $E_{\mathrm{R}}(E)$ is defined as:

$$E_{\mathrm{R}}(E) = E_{\mathrm{RES}} - Q - (E - E_{^8\mathrm{Be}}), \tag{5.27}$$

where Q = 7.3666 MeV and E_{RES} is the excitation energy of the state in ^{12}C, listed in Table 5.2 for the 1_1^- and 2_2^+ states. Similarly, the γ-ray energy depends on both the $\alpha + \alpha$ energy E as well as the $\alpha + {}^8$Be energy E':

$$E_\gamma = E' + Q + (E - E_{^8\mathrm{Be}}). \tag{5.28}$$

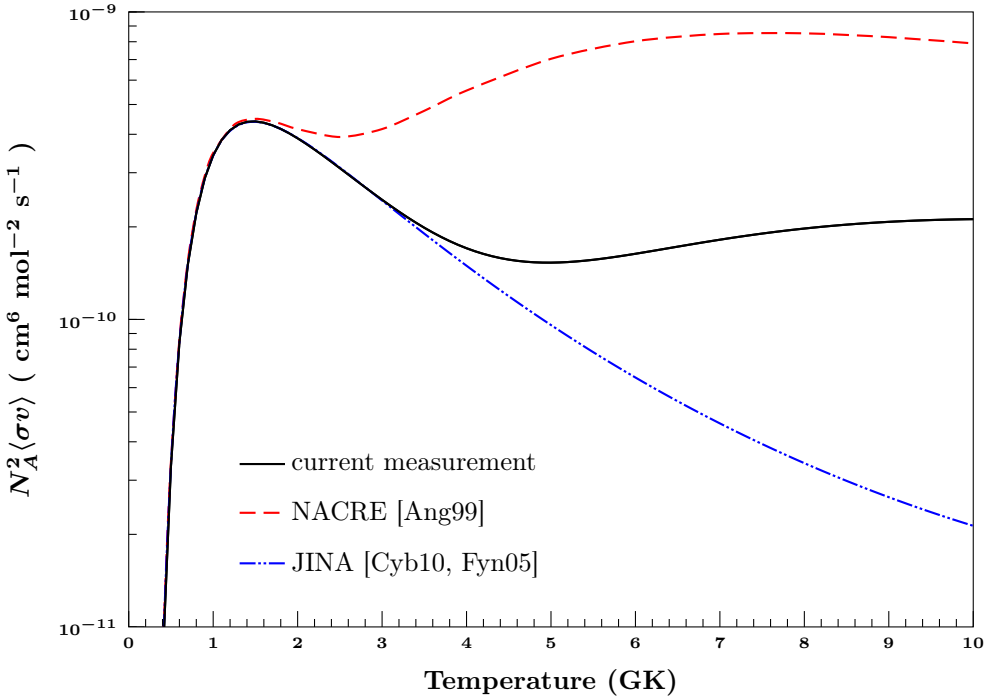

Figure 5.12: Triple-α reaction rates, calculated using Equation 5.23 and the resonances measured in this experiment compared with the rates published by NACRE [Ang99] and the JINA-REACLIB compilation [Cyb10] based on experimental results from Fynbo *et al.* [Fyn05]. Experimental uncertainties in the calculated reaction rates are discussed in Section 5.3.2.

Triple-α reaction rates were calculated by numerically integrating Equation 5.23 for temperatures between 0–10 GK. In addition to the 1_1^- and 2_2^+ states measured in this experiment, the calculated reaction rates also included contributions from the 0_2^+ Hoyle state at 7.6542 MeV and the 3_1^- state at 9.641 MeV. Figure 5.12 shows the calculated triple-α reaction rates along with the reaction rates published in several compilations [Ang99, Cyb10].

5.3.2 Propagation of Uncertainties

The uncertainties in the calculated triple-α reaction rates were calculated by summing in quadrature the uncertainties due to each of the four contributing states in

^{12}C (0_2^+, 1_1^-, 2_2^+, and 3_1^-). Figure 5.13 shows the calculation of the total uncertainty in the reaction rates.

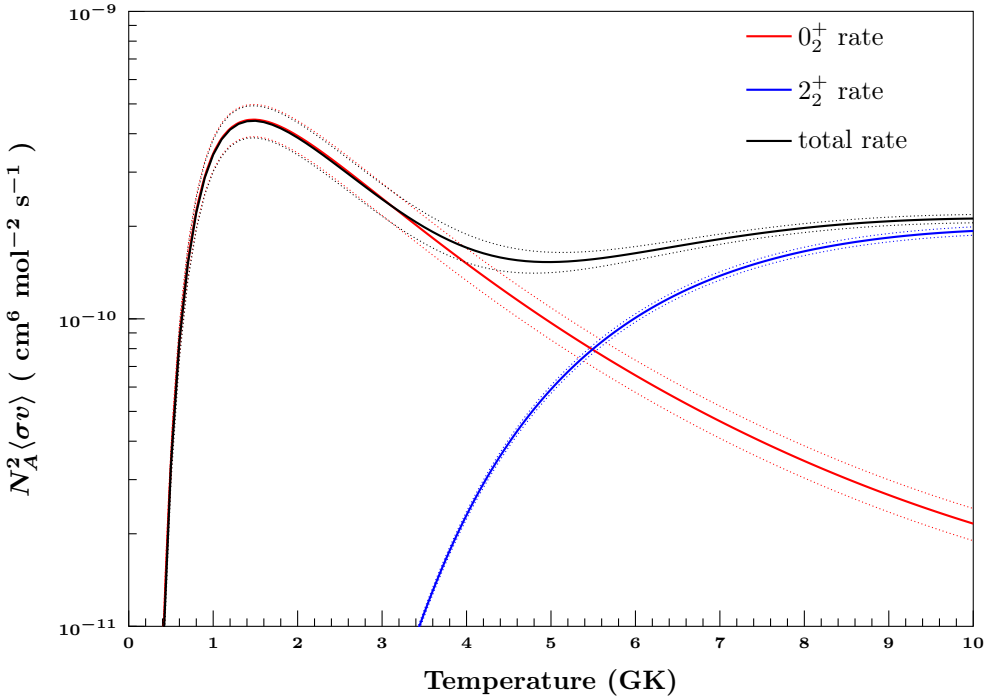

Figure 5.13: Uncertainties in the calculated triple-α reaction rates.

The contributions from the 1_1^- and 3_1^- states to the total reaction rates are very small ($< 10^{-11}$ cm^6 mol^{-2} s^{-1}) at all applicable temperatures, so the contribution of the uncertainties in these states to the uncertainties in the total reaction rates is negligible. There is a constant 12 % uncertainty in the contribution of the 0_2^+ Hoyle state to the total reaction rates due to the uncertainty in the total radiative decay width [Che10].

The experimental uncertainties in the measured 2_2^+ state were propagated to the reaction rates using the full set of combinations of resonance parameters and their associated values of χ^2 from the fit to the 2_2^+ resonance, described in Section 5.2.5. For each combination of 2_2^+ resonance parameters, reaction rates were calculated for the full temperature range between 0–10 GK. Each set of reaction rates was assigned

the χ^2 value from the set of resonance parameters that was used to generate it, and the uncertainty in the reaction rates at each temperature was calculated using the χ^2 values associated with each of the calculated reaction rates at that temperature. This takes into account all correlations and anti-correlations in E_{RES}, Γ_α, and Γ_γ from the fit to the 2_2^+ state.

Tabulated reaction rates are listed in Appendix A.

5.3.3 Effect on Explosive Nucleosynthesis

The 2_2^+ state in ^{12}C measured in this experiment results in high-temperature triple-α reaction rates which are higher than those listed in the JINA-REACLIB compilation [Cyb10], although lower than those listed by NACRE [Ang99] (see Figure 5.12).

The possible effects of these new reaction rates on the outcome of explosive nucleosynthesis during core-collapse supernovae were studied in simulations performed by Frölich [Frö13] according to the method described by Arcones *et al.* [Arc12]. These simulations included the νp-process (see Section 1.4), in which neutrino-driven winds contribute to the synthesis of heavy elements by allowing neutron-deficient nuclei to capture the neutrons which are produced when proton-rich matter interacts with a strong antineutrino flux [Frö06]. The simulations used a trajectory developed by Arcones *et al.* [Arc12] which assumes that the neutrino-driven wind terminates at a temperature of 2 GK, and that the duration of the constant temperature phase associated with the wind termination is 0.5 s.

The simulation was run using the triple-α reaction rates calculated in this work (Appendix A) as well as the triple-α reaction rates listed in the JINA-REACLIB compilation [Cyb10] based on the experimental results of Fynbo *et al.* [Fyn05].

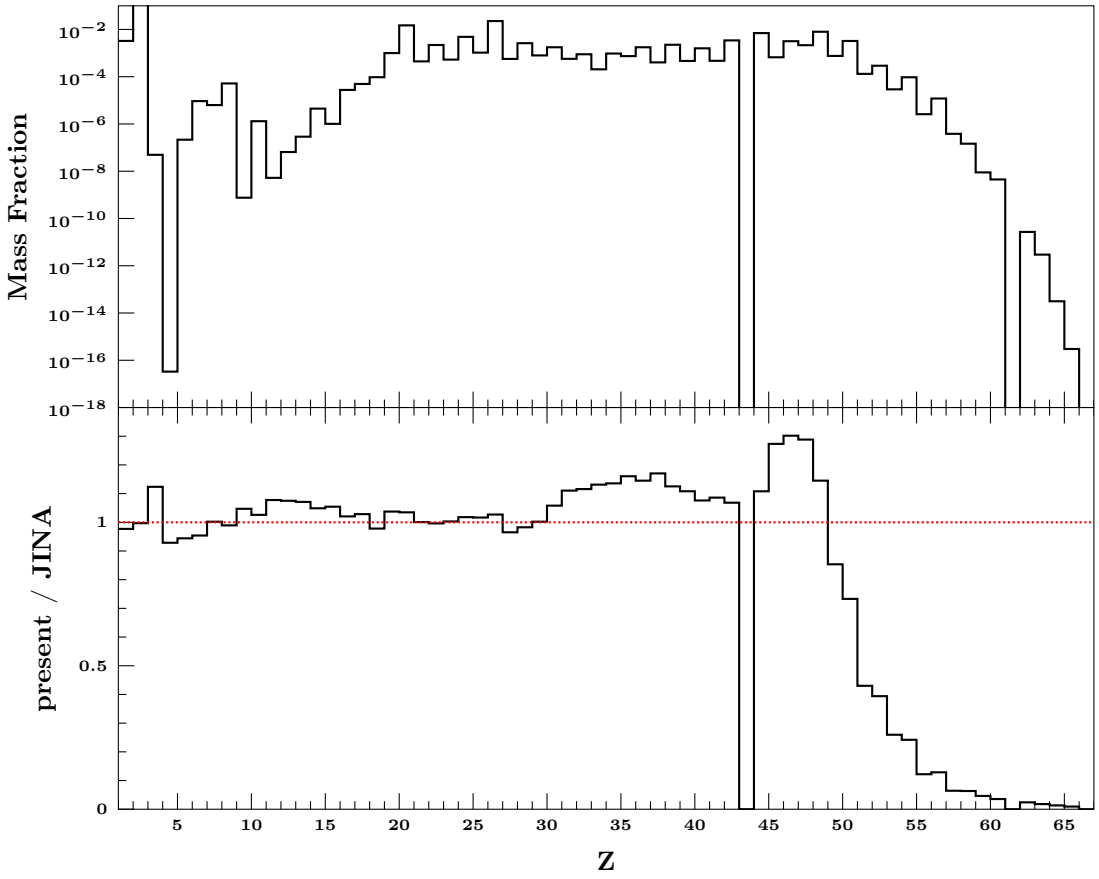

Figure 5.14: Top: Elemental mass fractions in supernova ejecta from simulations [Frö13] of νp-process explosive nucleosynthesis [Frö06, Arc12], using the triple-α reaction rates calculated in this work. The dips at Z = 43 and Z = 61 correspond to technetium and promethium, respectively. Bottom: Ratio of elemental abundances simulated using the current triple-α reaction rates to the abundances simulated using the rates published in the JINA-REACLIB compilation [Cyb10] based on the experimental results of Fynbo *et al.* [Fyn05].

Figure 5.14 shows the mass fraction of each element produced in the simulated explosive nucleosynthesis using the new triple-α reaction rates, and Figure 5.15 shows the mass fractions for each mass number A. Both figures show the results using the triple-α reaction rates calculated in this work compared with those listed in the JINA-REACLIB compilation [Cyb10].

The new triple-α reaction rates enhance the production of certain isotopes of elements between rhodium and cadmium (Z = 45–48 and A = 100–110) while severely

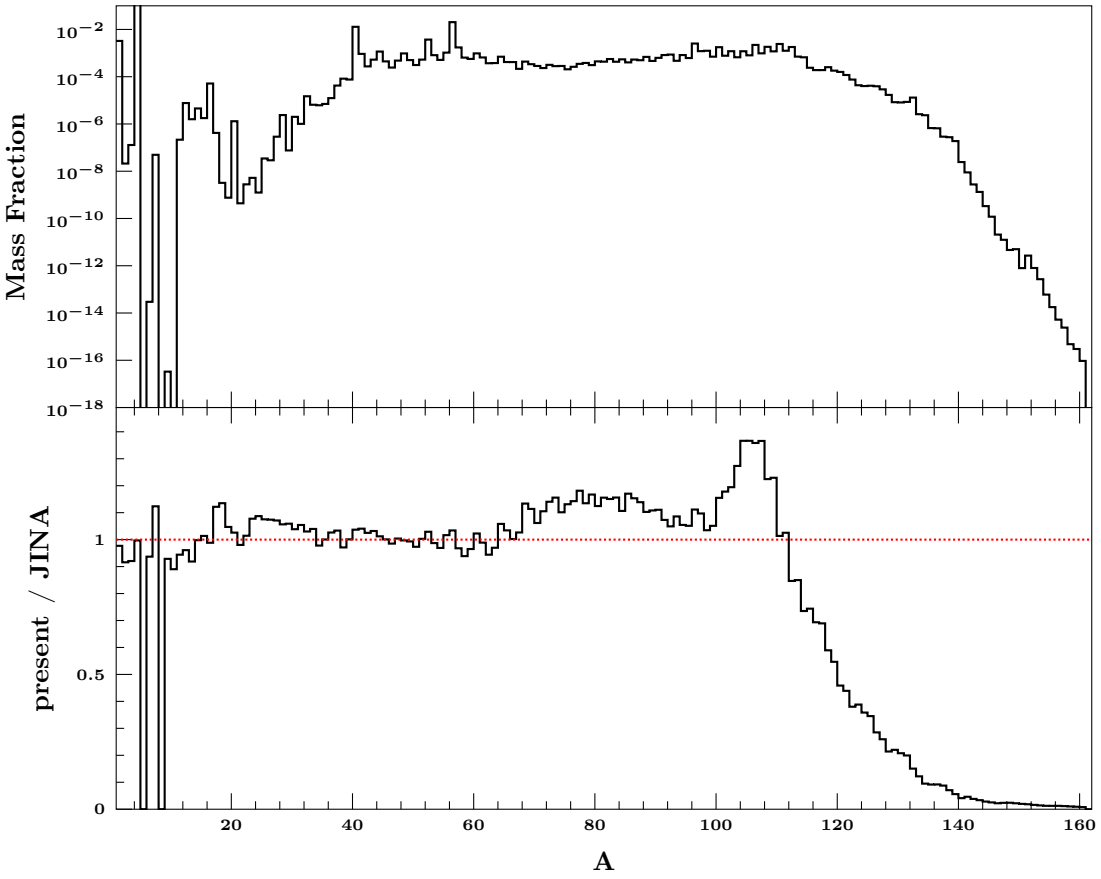

Figure 5.15: Same as Figure 5.14, except the simulated mass fractions are plotted as a function of mass number A.

suppressing the production of many heavier nuclei.

The abundances and mass fractions of each isotope produced in the simulated supernovae for both sets of reaction rates are listed in Appendix B.

5.4 Nuclear Structure

5.4.1 Isospin-Forbidden *E*1 Transition

In the ^{12}C(γ,α)^{8}Be reaction, the target nucleus as well as all of the reaction products are self-conjugate nuclei, so only $\Delta T = 0$ electromagnetic transitions can

contribute. The 1_1^- state is only accessible from the ground state through an $E1$ transition, but $\Delta T = 0$ $E1$ transitions are forbidden for self-conjugate nuclei [War69].

An estimate of the forbidden isoscalar contribution to an $E1$ radiative width can be calculated using corrections to the long-wavelength approximation. The matrix element for an isoscalar electromagnetic transition of multipolarity $E\lambda$ is proportional to a spherical Bessel function which may be expanded in powers of kr [War69]:

$$j_\lambda(kr) = \frac{(kr)^\lambda}{(2\lambda+1)!!} - \frac{(kr)^{\lambda+2}}{2(2\lambda+3)!!} + \mathcal{O}\left[(kr)^{\lambda+4}\right] \tag{5.29}$$

In the long-wavelength approximation kr is small, and the spherical Bessel function is approximately equal to the first term in Equation 5.29. In the case of a dipole transition, this gives a vanishing matrix element [War69] which leads to the selection rule which forbids isoscalar $E1$ transitions. An estimate can be made of the strength of the isospin-forbidden radiative width relative to the hypothetical isovector radiative width by comparing the first two terms in the Bessel function expansion. Using a channel radius of $r = 1.2\mathrm{A}^{1/3}$ fm, the isoscalar fraction is [War69]:

$$5.5 \times 10^{-8}\ E_\gamma^4 \left(\frac{A}{16}\right)^{\frac{4}{3}}, \tag{5.30}$$

where E_γ is in MeV.

Equation 5.30 predicts an isoscalar fraction of 5.3×10^{-4} for the $E1$ transition from the 1_1^- state in ^{12}C to the ground state. Assuming the full (isovector + isoscalar) radiative width to be the width for a pure single-particle state (1 W.u.), then the reduced isoscalar transition probability is $\mathrm{B}(E1 : 1_1^- \rightarrow 0_1^+) = 1.8 \times 10^{-4}\,\mathrm{e}^2\ \mathrm{fm}^2$. This predicted B($E1$) is a factor of 3.8 greater than the B($E1$) measured in this experiment ($4.84(30) \times 10^{-5}\,\mathrm{e}^2\ \mathrm{fm}^2$), indicating that the 1_1^- state in ^{12}C is not likely

to be a pure single-particle state.

The only other experiment to measure this $E1$ transition probability was performed by Campos *et al.* [Cam95] who used electron scattering on ^{12}C to measure $\mathrm{B}(E1) = 3.9(20) \times 10^{-6}\,\mathrm{e^2fm^2}$, an order of magnitude smaller than the results of the current experiment. However, it is not clear from their publication whether this value was given for the transition from the 1^-_1 state to the ground state (which is what is quoted above) or from the ground state to the 1^-_1 state (which would be three times larger), leading to a factor-of-three ambiguity in their reported value.

5.4.2 α-Particle Clustering

The Hoyle state has been established to be an α-cluster state [Fre12a] based on its proximity in energy to the three-α-particle threshold [Mor56]. The cluster nature of this state is further supported by the failure of shell model calculations to describe the state [Kar95, Nav00b] and the success of cluster models [Des87].

The reduced α-decay width of the 2^+_2 state measured in this experiment exhausts $157(15)\,\%$ of the Wigner limit. The Wigner single-particle limit is derived by assuming a square-well potential. When a diffuse Woods-Saxon potential is used the effective single-particle limit increases by a factor f given by [Vog62]:

$$f \approx 1 + 6.7\,a^2, \tag{5.31}$$

where a is the surface thickness of the potential in fm. Assuming that the measured value of γ^2_α corresponds to to the full single-particle limit gives $a = 0.29(4)\,\mathrm{fm}$, which is in good agreement with the surface thickness $a = 0.31(6)\,\mathrm{fm}$ obtained from an optical model analysis [Vog62] of neutron scattering data [Hug58].

The large reduced α-decay width of the 2^+_2 state also indicates a strong single-

α-particle component to the state, which indicates that like the Hoyle state, the 2_2^+ state is an α-cluster state [Des10]. This is consistent with the 2_2^+ state being an excitation of the Hoyle state.

The reduced α-decay width of the 1_1^- state; however, exhausts only $8.8^{+1.2}_{-1.1}\,\%$ of the Wigner limit. This indicates a very weak single-α-particle component of the state and a very low level of α-clustering.

5.4.3 Hoyle State Rotational Band

Following an argument introduced by Freer *et al.* [Fre12b], constraints can be made on the α-cluster structure of the Hoyle state by assuming that the 2_2^+ state is the first member its rotational band. There is also a rotational band built upon the 0^+ ground state of the α-cluster nucleus ^{8}Be, and the first 2^+ excited state in ^{8}Be is assumed to be the first member of that band with energy $\dfrac{3\hbar^2}{I}$ [Boh75], where I is the moment of inertia. The charge radius for an α particle has been measured to be 1.673(1) fm [Bor78], and the first 2^+ excited state of ^{8}Be has an excitation energy of 3.03 MeV [Til04]. Using a simple semi-classical model which treats the nuclear α-clusters as constant-density spherical α particles, then the moment of inertia is given by $I = 2\left(\frac{2}{5}M_\alpha r_\alpha^2 + \frac{1}{4}M_\alpha R^2\right)$, where R is the separation distance between the centers of two α particles with mass M_α and radius r_α. The excitation energy of the first 2^+ state in ^{8}Be can be reproduced when the centers of the two α particles that make up the ^{8}Be nucleus are separated by 2.4 times their charge radius [Fre12b].

Taking this to be the separation between the α particles in the Hoyle state, the excitation energy of the first member of its rotational band, assumed to be the 2_2^+ state, can be calculated for various arrangements of the three α particles. If, for example, the α particles are arranged in a linear chain [Mor56, Mor66, Suz72, Mer92],

then the 2_2^+ state would be 1.0 MeV above the Hoyle state at an excitation energy of 8.65 MeV. The results of the present experiment exclude this configuration.

If, however, the α particles are arranged in an equilateral triangle and rotated about an axis which passes through one of the α particles and halfway between the other two, then the 2_2^+ state would be 2.75 MeV above the Hoyle state at an excitation energy of 10.4 MeV. While the results of this experiment cannot exclude this equilateral triangle configuration, the measured excitation energy of the 2_2^+ state ($10.13^{+0.06}_{-0.05}$ MeV) can be exactly reproduced with an isosceles triangle formed by lengthening one side of the equilateral triangle to 2.58(3) times the α-particle charge radius.

This argument relies on the assumption that the Hoyle state and the 2_2^+ state are members of a rotational band, an assumption which is supported by the lattice EFT calculations [Epe12], but is contradicted by both the FMD model [Che07] and the BEC model [Yam05] (see Section 2). One way to test the rotational nature of the 2_2^+ state is to search for the next member of the hypothetical rotational band, i.e., a 4^+ excitation. If it is a member of this rotational band, this 4^+ state should be a broad, $T = 0$ state with 3.3 times the excitation energy of the 2_2^+ state relative to the Hoyle state [Boh75], or approximately 16 MeV above the ground state. There is no known 4^+ state in this region, although there is a broad state previously observed at 15.4 MeV with uncertain J^π and T assignment [Ajz90].

5.5 Comparison with Previous Work

5.5.1 Comparison with Previous Experiments

1_1^- State

The measured resonance energy of the 1_1^- state in this work ($E_{\text{RES}} = 10.913^{+0.020}_{-0.018}$ MeV) is slightly higher than the previously-measured value of 10.844(16) MeV [Ajz90]. One possible explanation for this discrepancy is that previous measurements may have been influenced by the high-energy tail of the overlapping 2_2^+ state (see Figures 5.4 and 5.5). A falling cross section from an unidentified 2_2^+ state would tend to shift the peak from the broad 1_1^- state to a slightly lower energy. Separating the $E1$ and $E2$ components of the cross section—as was done in this experiment—yields parameters of the 1_1^- state independent of the 2_2^+ state.

2_2^+ State

Table 5.3 compares the parameters of the 2_2^+ state measured in this experiment with those reported by the previous experiments discussed in Section 1.3.

The parameters of the 2_2^+ state measured in this experiment are generally consistent with those reported by the various scattering experiments, but the present results give a somewhat higher resonance energy and width. The results reported by the scattering experiments tend to be highly dependent on the subtraction of the background contributions from the 0_3^+ and 3_1^- states at 9.64 MeV and 10.3 MeV, respectively. The difference in the resonance energy and width of the 2_2^+ state in the present experiment may be due to the lack of the contributions from the 0_3^+ and 3_1^- states. Also, the present resonance energy of the 2_2^+ state was determined using a Breit-Wigner formula with energy-dependent widths (Equation 5.7). Not all other

Table 5.3: Parameters of the 2_2^+ state in ^{12}C measured in this experiment compared with the results from previous experiments.

Experiment	Ref.	E_x (MeV)	Γ (keV)
β-delayed α-decay	[Fyn05, Dig05]	(no state)	—
	[Hyl10]	11.1(3)	1400(400)
^{12}C(x,x′)^{12}C	[Fre12b]†	9.75(15)	750(150)
	[Fre09, Zim11]	9.6(1)	600(100)
	[Ito11, Ito04]	9.84(6)	1010(150)
$^{10/11}$B(^{3}He,p/d)^{12}C	[Smi12]	9.7	—
	[Alc12]	(no state)	—
current measurement		$10.13^{+0.06}_{-0.05}$	2080^{+330}_{-260}

†The results presented by Freer *et al.* [Fre12b] represent a re-analysis of previously published inelastic scattering data [Fre09, Ito11, Ito04]

experimental works did this. If instead E_{RES} were determined as the energy corresponding to the peak value of the $E2$ cross section (9.93 MeV), the 2_2^+ resonance energy measured in the current experiment would agree fairly well with the values determined from the inelastic scattering experiments.

It is not clear why no 2_2^+ state near 10 MeV was seen in the β-delayed α-decay experiments [Fyn05, Hyl10], although it was suggested by Khoa *et al.* [Kho11] that the strong α-cluster nature of the 2_2^+ state could lead to a very small overlap with the ground state wavefunctions of ^{12}B and ^{12}N. These are 1^+ states with $T = 1$ and are isobaric analog states of the first $T = 1$ state in ^{12}C at 15.1 MeV [Ajz90]. This state and its strong $M1$ transition to the ground state of ^{12}C is well described as a 1p-1h excitation of the ground state of ^{12}C [Coh65], which should have very little overlap with an α-cluster state.

5.5.2 Comparison with Theoretical Models

Table 5.4 compares the results from this experiment with the predictions made by the various theories discussed in Chapter 2.

Table 5.4: Results of this experiment compared with various theoretical predictions.

Theory	Ref.	State	E_x (MeV)	γ_α^2 (keV)	$B(E\lambda \to 0_1^+)$ (e^2 $fm^{2\lambda}$)
Microscopic Cluster	[Des87]	1_1^-	12.50	61.5	—
		2_2^+	9.27	356	4.1
BEC	[Yam05]	1_1^-	10.48	—	—
		2_2^+	9.7	1200	—
FMD	[Che07, Nef12]	2_2^+	10.06†	—	0.46
EFT	[Epe12]	2_2^+	9.65	—	2(1)
current measurement		1_1^-	$10.913^{+0.020}_{-0.018}$	$82.4^{+10.5}_{-9.5}$	$4.84(30) \times 10^{-5}$
		2_2^+	$10.13^{+0.06}_{-0.05}$	1470^{+160}_{-120}	$1.57^{+0.14}_{-0.11}$

†The FMD 2_2^+ energy was calculated from the predicted energy difference relative to the three-α threshold [Nef12].

The energy of the 2_2^+ state measured in this experiment is quite close to the prediction made by the FMD model [Che07, Nef12], and not unreasonably different from the predictions made by the BEC model [Yam05] and the lattice EFT calculations [Epe12]. The reduced α-decay width predicted by the BEC model is in fairly good agreement with the experimental value. The B($E2$) value predicted by the FMD model is significantly lower than the experimental value, while the B($E2$) predicted by the EFT calculations agrees well with the present value, albeit with a large uncertainty.

5.6 Summary & Conclusions

2_2^+ State in ^{12}C

The 2_2^+ state in ^{12}C has been unambiguously identified for the first time. This state was predicted over fifty years ago [Mor56] to exist as an excitation of the Hoyle state, and this experiment definitively confirms the existence of the state as well as the spin, parity and isospin assignments $J^\pi;T = 2^+;0$. The 2_2^+ state was directly observed at an energy of $E_{\rm RES} = 10.13^{+0.06}_{-0.05}\,$MeV with an α-decay width of $\Gamma_\alpha = 2080^{+330}_{-260}\,$keV, corresponding to a reduced α-decay width of $\gamma^2_\alpha = 1470^{+160}_{-120}\,$keV. This reduced α-decay width is $1.57^{+0.17}_{-0.13}$ times the Wigner limit, which strongly supports an α-cluster description of the state. The γ-decay width to the ground state was measured to be $\Gamma_\gamma = 135^{+16}_{-12}\,$meV, which corresponds to the first measurement of the reduced electromagnetic transition probability $\mathrm{B}(E2 : 2_2^+ \rightarrow 0_1^+) = 1.57^{+0.14}_{-0.11}\,\mathrm{e}^2\ \mathrm{fm}^4$ or $0.963^{+0.083}_{-0.069}\,\mathrm{W\,u}$.

1_1^- State in ^{12}C

The previously-measured 1_1^- state in ^{12}C [Ajz90] was identified at an energy of $E_{\rm RES} = 10.913^{+0.020}_{-0.018}\,$MeV with an α-decay width of $\Gamma_\alpha = 305^{+40}_{-36}\,$keV, and the previously assigned spin, parity and isospin assignments of $J^\pi;T = 1^-;0$ were confirmed. The reduced α-decay width was measured to be $82.4^{+10.5}_{-9.5}\,$keV or $0.088^{+0.012}_{-0.011}$ times the Wigner limit, which excludes an α-cluster description of the state. The isospin-forbidden $E1$ transition probability to the ground state was measured to be $\mathrm{B}(E1 : 1_1^- \rightarrow 0_1^+) = 4.84(30) \times 10^{-5}\,\mathrm{e}^2\ \mathrm{fm}^2$ or $1.43(9) \times 10^{-4}\,\mathrm{W\,u}$.

Theoretical Outlook

Currently, there are several *ab initio* theories being actively developed which attempt to describe the low-lying excited states in ^{12}C. In particular, lattice EFT calculations have progressed from descriptions of two- and three-nucleon systems [Epe10b] into frameworks which can accurately describe the twelve-nucleon ^{12}C system [Epe11], even using the Hoyle state to constrain quark masses and the fine structure constant [Epe13]. These lattice EFT calculations have managed to build a description of the ^{12}C nucleus in which α-clustering spontaneously arises, and observable parameters related to the Hoyle state and the 2_2^+ state in ^{12}C are accurately reproduced.

The results of this experiment represent observables which may help to elucidate the structure of low-lying states in ^{12}C. The parameters of the 1_1^- and 2_2^+ states measured here may serve to guide and constrain future *ab initio* lattice EFT calculations as well as any theory which attempts to describe the structure of ^{12}C and the α-clustering phenomenon in light nuclei.

Astrophysics

The 2_2^+ state in ^{12}C serves as a resonance in the ^{8}Be(α,γ)^{12}C reaction and increases the rate of thermonuclear helium burning at the high temperatures which are thought to occur during core-collapse supernovae and other astrophysical phenomena. Ambiguity in the existence of the 2_2^+ state in ^{12}C has lead to a long-standing disagreement in the triple-α reaction rates published by the NACRE [Ang99] and JINA-REACLIB [Cyb10] compilations, which has been resolved in the present work. New high-temperature triple-α reaction rates have been calculated using the results of this experiment, and the effect of these new rates was studied in supernova simulations [Frö13] with νp-process explosive nucleosynthesis. The triple-α reaction rates

calculated in this work were found to significantly alter the outcome of heavy element production as compared with the same simulations run using the previously published triple-α reaction rates [Cyb10].

While the mechanism and dynamics of astrophysical explosive nucleosynthesis remain uncertain, the new triple-α reaction rates presented in this work may help to guide and constrain different possible scenarios for the production of heavy elements in the universe.

Appendix A

Tabulated Triple-α Reaction Rates

Table A.1: Triple-α reaction rates calculated using Equation 5.23. The reaction rates below 1.5 GK are identical to the ones listed in the JINA-REACLIB compilation [Cyb10].

Tempurature (GK)	Rate (cm^6 mol^{-2} s^{-1})	$+1\sigma$	-1σ
0.1	2.040×10^{-24}	2.285×10^{-24}	1.795×10^{-24}
0.2	9.447×10^{-16}	1.058×10^{-15}	8.313×10^{-16}
0.3	4.384×10^{-13}	4.910×10^{-13}	3.858×10^{-13}
0.4	7.282×10^{-12}	8.156×10^{-12}	6.408×10^{-12}
0.5	3.366×10^{-11}	3.769×10^{-11}	2.962×10^{-11}
0.6	8.428×10^{-11}	9.440×10^{-11}	7.417×10^{-11}
0.7	1.510×10^{-10}	1.691×10^{-10}	1.329×10^{-10}
0.8	2.216×10^{-10}	2.482×10^{-10}	1.950×10^{-10}
0.9	2.865×10^{-10}	3.209×10^{-10}	2.521×10^{-10}
1.0	3.404×10^{-10}	3.813×10^{-10}	2.996×10^{-10}
1.1	3.816×10^{-10}	4.274×10^{-10}	3.358×10^{-10}
1.2	4.104×10^{-10}	4.597×10^{-10}	3.612×10^{-10}
1.3	4.284×10^{-10}	4.798×10^{-10}	3.770×10^{-10}
1.4	4.374×10^{-10}	4.898×10^{-10}	3.849×10^{-10}
1.5	4.391×10^{-10}	4.918×10^{-10}	3.864×10^{-10}
1.6	4.353×10^{-10}	4.875×10^{-10}	3.831×10^{-10}
1.7	4.274×10^{-10}	4.786×10^{-10}	3.761×10^{-10}
1.8	4.164×10^{-10}	4.664×10^{-10}	3.665×10^{-10}
1.9	4.034×10^{-10}	4.518×10^{-10}	3.550×10^{-10}
2.0	3.882×10^{-10}	4.348×10^{-10}	3.415×10^{-10}
2.1	3.726×10^{-10}	4.175×10^{-10}	3.278×10^{-10}
2.2	3.568×10^{-10}	3.998×10^{-10}	3.138×10^{-10}
2.3	3.410×10^{-10}	3.821×10^{-10}	2.999×10^{-10}
2.4	3.255×10^{-10}	3.648×10^{-10}	2.863×10^{-10}
2.5	3.104×10^{-10}	3.478×10^{-10}	2.730×10^{-10}
2.6	2.959×10^{-10}	3.316×10^{-10}	2.603×10^{-10}
2.7	2.821×10^{-10}	3.160×10^{-10}	2.481×10^{-10}
2.8	2.689×10^{-10}	3.012×10^{-10}	2.366×10^{-10}
2.9	2.565×10^{-10}	2.873×10^{-10}	2.258×10^{-10}

Tempurature (GK)	Rate (cm^6 mol^{-2} s^{-1})	$+1\sigma$	-1σ
3.0	2.449×10^{-10}	2.742×10^{-10}	2.157×10^{-10}
3.1	2.341×10^{-10}	2.619×10^{-10}	2.063×10^{-10}
3.2	2.241×10^{-10}	2.506×10^{-10}	1.977×10^{-10}
3.3	2.149×10^{-10}	2.401×10^{-10}	1.897×10^{-10}
3.4	2.064×10^{-10}	2.304×10^{-10}	1.825×10^{-10}
3.5	1.987×10^{-10}	2.215×10^{-10}	1.759×10^{-10}
3.6	1.917×10^{-10}	2.134×10^{-10}	1.700×10^{-10}
3.7	1.854×10^{-10}	2.061×10^{-10}	1.647×10^{-10}
3.8	1.798×10^{-10}	1.995×10^{-10}	1.601×10^{-10}
3.9	1.748×10^{-10}	1.936×10^{-10}	1.560×10^{-10}
4.0	1.704×10^{-10}	1.884×10^{-10}	1.525×10^{-10}
4.1	1.666×10^{-10}	1.838×10^{-10}	1.495×10^{-10}
4.2	1.634×10^{-10}	1.797×10^{-10}	1.470×10^{-10}
4.3	1.606×10^{-10}	1.762×10^{-10}	1.450×10^{-10}
4.4	1.583×10^{-10}	1.733×10^{-10}	1.434×10^{-10}
4.5	1.565×10^{-10}	1.708×10^{-10}	1.422×10^{-10}
4.6	1.551×10^{-10}	1.688×10^{-10}	1.414×10^{-10}
4.7	1.541×10^{-10}	1.672×10^{-10}	1.409×10^{-10}
4.8	1.534×10^{-10}	1.660×10^{-10}	1.408×10^{-10}
4.9	1.531×10^{-10}	1.652×10^{-10}	1.409×10^{-10}
5.0	1.530×10^{-10}	1.646×10^{-10}	1.414×10^{-10}
5.1	1.532×10^{-10}	1.644×10^{-10}	1.420×10^{-10}
5.2	1.537×10^{-10}	1.645×10^{-10}	1.429×10^{-10}
5.3	1.544×10^{-10}	1.648×10^{-10}	1.440×10^{-10}
5.4	1.553×10^{-10}	1.653×10^{-10}	1.452×10^{-10}
5.5	1.563×10^{-10}	1.660×10^{-10}	1.466×10^{-10}
5.6	1.575×10^{-10}	1.669×10^{-10}	1.481×10^{-10}
5.7	1.589×10^{-10}	1.679×10^{-10}	1.498×10^{-10}
5.8	1.603×10^{-10}	1.691×10^{-10}	1.515×10^{-10}
5.9	1.619×10^{-10}	1.704×10^{-10}	1.533×10^{-10}
6.0	1.635×10^{-10}	1.719×10^{-10}	1.551×10^{-10}
6.1	1.652×10^{-10}	1.734×10^{-10}	1.571×10^{-10}
6.2	1.670×10^{-10}	1.749×10^{-10}	1.590×10^{-10}
6.3	1.688×10^{-10}	1.765×10^{-10}	1.610×10^{-10}
6.4	1.706×10^{-10}	1.782×10^{-10}	1.630×10^{-10}
6.5	1.725×10^{-10}	1.799×10^{-10}	1.650×10^{-10}
6.6	1.743×10^{-10}	1.817×10^{-10}	1.670×10^{-10}
6.7	1.762×10^{-10}	1.834×10^{-10}	1.689×10^{-10}
6.8	1.780×10^{-10}	1.851×10^{-10}	1.709×10^{-10}
6.9	1.799×10^{-10}	1.869×10^{-10}	1.728×10^{-10}
7.0	1.817×10^{-10}	1.886×10^{-10}	1.747×10^{-10}

Tempurature (GK)	Rate (cm^6 mol^{-2} s^{-1})	$+1\sigma$	-1σ
7.1	1.835×10^{-10}	1.903×10^{-10}	1.765×10^{-10}
7.2	1.852×10^{-10}	1.920×10^{-10}	1.783×10^{-10}
7.3	1.869×10^{-10}	1.937×10^{-10}	1.801×10^{-10}
7.4	1.886×10^{-10}	1.953×10^{-10}	1.818×10^{-10}
7.5	1.902×10^{-10}	1.969×10^{-10}	1.835×10^{-10}
7.6	1.918×10^{-10}	1.984×10^{-10}	1.851×10^{-10}
7.7	1.933×10^{-10}	1.999×10^{-10}	1.866×10^{-10}
7.8	1.948×10^{-10}	2.013×10^{-10}	1.881×10^{-10}
7.9	1.962×10^{-10}	2.027×10^{-10}	1.895×10^{-10}
8.0	1.975×10^{-10}	2.041×10^{-10}	1.909×10^{-10}
8.1	1.988×10^{-10}	2.053×10^{-10}	1.922×10^{-10}
8.2	2.001×10^{-10}	2.066×10^{-10}	1.934×10^{-10}
8.3	2.012×10^{-10}	2.077×10^{-10}	1.946×10^{-10}
8.4	2.023×10^{-10}	2.088×10^{-10}	1.957×10^{-10}
8.5	2.034×10^{-10}	2.099×10^{-10}	1.967×10^{-10}
8.6	2.044×10^{-10}	2.109×10^{-10}	1.977×10^{-10}
8.7	2.053×10^{-10}	2.118×10^{-10}	1.986×10^{-10}
8.8	2.061×10^{-10}	2.126×10^{-10}	1.995×10^{-10}
8.9	2.069×10^{-10}	2.134×10^{-10}	2.003×10^{-10}
9.0	2.077×10^{-10}	2.142×10^{-10}	2.010×10^{-10}
9.1	2.083×10^{-10}	2.148×10^{-10}	2.017×10^{-10}
9.2	2.090×10^{-10}	2.155×10^{-10}	2.023×10^{-10}
9.3	2.095×10^{-10}	2.160×10^{-10}	2.029×10^{-10}
9.4	2.100×10^{-10}	2.165×10^{-10}	2.034×10^{-10}
9.5	2.105×10^{-10}	2.170×10^{-10}	2.038×10^{-10}
9.6	2.109×10^{-10}	2.174×10^{-10}	2.042×10^{-10}
9.7	2.112×10^{-10}	2.177×10^{-10}	2.045×10^{-10}
9.8	2.115×10^{-10}	2.180×10^{-10}	2.048×10^{-10}
9.9	2.117×10^{-10}	2.182×10^{-10}	2.051×10^{-10}
10.0	2.119×10^{-10}	2.184×10^{-10}	2.053×10^{-10}

Appendix B

Isotope Abundances and Mass Fractions

Table B.1: Isotope abundances and mass fractions in supernovae ejecta from νp-process simulations [Frö06, Arc12] of explosive nucleosynthesis. The 'present' values are the results using the triple-α reaction rates calculated from the results of this experiment (Table A.1), while the 'JINA-REACLIB' values are the results using the triple-α reaction rates published in the JINA compilation [Cyb10] based on the experimental results of Fynbo *et al.* [Fyn05].

	present		JINA-REACLIB		
Isotope	Abundance	Mass Fraction	Abundance	Mass Fraction	present / JINA
^{1}H	3.267×10^{-3}	3.267×10^{-3}	3.344×10^{-3}	3.344×10^{-3}	0.977
^{2}H	1.056×10^{-8}	2.112×10^{-8}	1.153×10^{-8}	2.306×10^{-8}	0.916
^{3}He	4.290×10^{-8}	1.287×10^{-7}	4.660×10^{-8}	1.398×10^{-7}	0.921
^{4}He	2.260×10^{-1}	9.038×10^{-1}	2.267×10^{-1}	9.070×10^{-1}	0.997
^{6}Li	4.949×10^{-15}	2.970×10^{-14}	5.283×10^{-15}	3.170×10^{-14}	0.937
^{7}Li	7.072×10^{-9}	4.950×10^{-8}	6.294×10^{-9}	4.406×10^{-8}	1.124
^{9}Be	3.672×10^{-18}	3.304×10^{-17}	3.954×10^{-18}	3.558×10^{-17}	0.929
^{10}B	1.241×10^{-21}	1.241×10^{-20}	1.394×10^{-21}	1.394×10^{-20}	0.890
^{11}B	1.961×10^{-8}	2.157×10^{-7}	2.077×10^{-8}	2.284×10^{-7}	0.944
^{12}C	6.397×10^{-7}	7.677×10^{-6}	6.657×10^{-7}	7.989×10^{-6}	0.961
^{13}C	1.221×10^{-7}	1.588×10^{-6}	1.329×10^{-7}	1.728×10^{-6}	0.919
^{14}N	3.240×10^{-7}	4.536×10^{-6}	3.247×10^{-7}	4.546×10^{-6}	0.998
^{15}N	1.181×10^{-7}	1.771×10^{-6}	1.165×10^{-7}	1.747×10^{-6}	1.014
^{16}O	3.220×10^{-6}	5.152×10^{-5}	3.258×10^{-6}	5.213×10^{-5}	0.988
^{17}O	2.460×10^{-8}	4.182×10^{-7}	2.193×10^{-8}	3.728×10^{-7}	1.122
^{18}O	1.789×10^{-10}	3.220×10^{-9}	1.576×10^{-10}	2.837×10^{-9}	1.135
^{19}F	3.985×10^{-11}	7.571×10^{-10}	3.806×10^{-11}	7.231×10^{-10}	1.047
^{20}Ne	6.529×10^{-8}	1.306×10^{-6}	6.364×10^{-8}	1.273×10^{-6}	1.026
^{21}Ne	2.090×10^{-11}	4.389×10^{-10}	2.132×10^{-11}	4.477×10^{-10}	0.980
^{22}Ne	1.266×10^{-10}	2.785×10^{-9}	1.248×10^{-10}	2.746×10^{-9}	1.014
^{23}Na	2.277×10^{-10}	5.238×10^{-9}	2.113×10^{-10}	4.861×10^{-9}	1.078
^{24}Mg	5.212×10^{-11}	1.251×10^{-9}	4.794×10^{-11}	1.151×10^{-9}	1.087
^{25}Mg	1.386×10^{-9}	3.465×10^{-8}	1.289×10^{-9}	3.222×10^{-8}	1.075
^{26}Mg	1.117×10^{-9}	2.904×10^{-8}	1.040×10^{-9}	2.705×10^{-8}	1.074

	present		JINA-REACLIB		
Isotope	Abundance	Mass Fraction	Abundance	Mass Fraction	present / JINA
^{27}Al	1.071×10^{-8}	2.892×10^{-7}	1.000×10^{-8}	2.701×10^{-7}	1.071
^{28}Si	8.510×10^{-8}	2.383×10^{-6}	8.054×10^{-8}	2.255×10^{-6}	1.057
^{29}Si	2.616×10^{-9}	7.586×10^{-8}	2.470×10^{-9}	7.163×10^{-8}	1.059
^{30}Si	6.672×10^{-8}	2.002×10^{-6}	6.424×10^{-8}	1.927×10^{-6}	1.039
^{31}P	3.262×10^{-8}	1.011×10^{-6}	3.094×10^{-8}	9.591×10^{-7}	1.054
^{32}S	4.648×10^{-7}	1.487×10^{-5}	4.512×10^{-7}	1.444×10^{-5}	1.030
^{33}S	1.970×10^{-7}	6.502×10^{-6}	1.895×10^{-7}	6.255×10^{-6}	1.040
^{34}S	1.818×10^{-7}	6.180×10^{-6}	1.859×10^{-7}	6.319×10^{-6}	0.978
^{36}S	2.983×10^{-10}	1.074×10^{-8}	3.280×10^{-10}	1.181×10^{-8}	0.909
^{35}Cl	2.009×10^{-7}	7.033×10^{-6}	2.008×10^{-7}	7.029×10^{-6}	1.000
^{37}Cl	1.141×10^{-6}	4.223×10^{-5}	1.104×10^{-6}	4.085×10^{-5}	1.034
^{36}Ar	3.445×10^{-7}	1.240×10^{-5}	3.356×10^{-7}	1.208×10^{-5}	1.027
^{38}Ar	2.178×10^{-6}	8.276×10^{-5}	2.243×10^{-6}	8.524×10^{-5}	0.971
^{40}Ar	4.809×10^{-9}	1.924×10^{-7}	5.258×10^{-9}	2.103×10^{-7}	0.915
^{39}K	1.942×10^{-6}	7.572×10^{-5}	1.940×10^{-6}	7.566×10^{-5}	1.001
^{41}K	2.254×10^{-5}	9.240×10^{-4}	2.166×10^{-5}	8.880×10^{-4}	1.041
^{40}Ca	3.231×10^{-4}	1.292×10^{-2}	3.116×10^{-4}	1.246×10^{-2}	1.037
^{42}Ca	6.498×10^{-6}	2.729×10^{-4}	6.339×10^{-6}	2.662×10^{-4}	1.025
^{43}Ca	1.226×10^{-5}	5.271×10^{-4}	1.188×10^{-5}	5.109×10^{-4}	1.032
^{44}Ca	2.634×10^{-5}	1.159×10^{-3}	2.602×10^{-5}	1.145×10^{-3}	1.012
^{46}Ca	5.705×10^{-8}	2.624×10^{-6}	6.738×10^{-8}	3.100×10^{-6}	0.847
^{45}Sc	9.886×10^{-6}	4.449×10^{-4}	9.877×10^{-6}	4.445×10^{-4}	1.001
^{46}Ti	5.240×10^{-6}	2.410×10^{-4}	5.309×10^{-6}	2.442×10^{-4}	0.987
^{47}Ti	1.021×10^{-5}	4.800×10^{-4}	1.017×10^{-5}	4.780×10^{-4}	1.004
^{48}Ti	2.014×10^{-5}	9.666×10^{-4}	2.020×10^{-5}	9.698×10^{-4}	0.997
^{49}Ti	1.030×10^{-5}	5.048×10^{-4}	1.037×10^{-5}	5.080×10^{-4}	0.993
^{50}Ti	1.319×10^{-7}	6.595×10^{-6}	1.523×10^{-7}	7.617×10^{-6}	0.866
^{51}V	1.038×10^{-5}	5.293×10^{-4}	1.035×10^{-5}	5.278×10^{-4}	1.003
^{50}Cr	6.106×10^{-6}	3.053×10^{-4}	6.256×10^{-6}	3.128×10^{-4}	0.976
^{52}Cr	7.157×10^{-5}	3.722×10^{-3}	6.954×10^{-5}	3.616×10^{-3}	1.029
^{53}Cr	1.539×10^{-5}	8.154×10^{-4}	1.559×10^{-5}	8.265×10^{-4}	0.987
^{54}Cr	2.463×10^{-7}	1.330×10^{-5}	2.806×10^{-7}	1.515×10^{-5}	0.878
^{55}Mn	1.897×10^{-5}	1.044×10^{-3}	1.866×10^{-5}	1.027×10^{-3}	1.017
^{54}Fe	9.261×10^{-6}	5.001×10^{-4}	9.530×10^{-6}	5.146×10^{-4}	0.972
^{56}Fe	3.640×10^{-4}	2.038×10^{-2}	3.520×10^{-4}	1.971×10^{-2}	1.034
^{57}Fe	3.044×10^{-5}	1.735×10^{-3}	3.145×10^{-5}	1.793×10^{-3}	0.968
^{58}Fe	4.002×10^{-7}	2.321×10^{-5}	4.822×10^{-7}	2.797×10^{-5}	0.830
^{59}Co	9.580×10^{-6}	5.652×10^{-4}	9.926×10^{-6}	5.856×10^{-4}	0.965
^{58}Ni	1.067×10^{-5}	6.190×10^{-4}	1.131×10^{-5}	6.562×10^{-4}	0.943

	present		JINA-REACLIB		
Isotope	Abundance	Mass Fraction	Abundance	Mass Fraction	present / JINA
^{60}Ni	1.617×10^{-5}	9.704×10^{-4}	1.581×10^{-5}	9.485×10^{-4}	1.023
^{61}Ni	1.070×10^{-5}	6.528×10^{-4}	1.082×10^{-5}	6.598×10^{-4}	0.989
^{62}Ni	5.990×10^{-6}	3.714×10^{-4}	6.345×10^{-6}	3.934×10^{-4}	0.944
^{64}Ni	7.867×10^{-8}	5.035×10^{-6}	9.534×10^{-8}	6.102×10^{-6}	0.825
^{63}Cu	6.002×10^{-6}	3.781×10^{-4}	6.189×10^{-6}	3.899×10^{-4}	0.970
^{65}Cu	6.427×10^{-6}	4.178×10^{-4}	6.214×10^{-6}	4.039×10^{-4}	1.034
^{64}Zn	1.088×10^{-5}	6.961×10^{-4}	1.026×10^{-5}	6.568×10^{-4}	1.060
^{66}Zn	6.299×10^{-6}	4.157×10^{-4}	6.285×10^{-6}	4.148×10^{-4}	1.002
^{67}Zn	3.209×10^{-6}	2.150×10^{-4}	3.126×10^{-6}	2.094×10^{-4}	1.027
^{68}Zn	6.408×10^{-6}	4.357×10^{-4}	5.652×10^{-6}	3.843×10^{-4}	1.134
^{70}Zn	1.804×10^{-8}	1.263×10^{-6}	2.081×10^{-8}	1.457×10^{-6}	0.867
^{69}Ga	4.901×10^{-6}	3.382×10^{-4}	4.400×10^{-6}	3.036×10^{-4}	1.114
^{71}Ga	3.277×10^{-6}	2.327×10^{-4}	2.965×10^{-6}	2.105×10^{-4}	1.105
^{70}Ge	4.049×10^{-6}	2.834×10^{-4}	3.810×10^{-6}	2.667×10^{-4}	1.063
^{72}Ge	4.409×10^{-6}	3.174×10^{-4}	3.866×10^{-6}	2.784×10^{-4}	1.140
^{73}Ge	3.835×10^{-6}	2.799×10^{-4}	3.318×10^{-6}	2.422×10^{-4}	1.156
^{74}Ge	1.446×10^{-7}	1.070×10^{-5}	1.524×10^{-7}	1.128×10^{-5}	0.949
^{76}Ge	1.891×10^{-9}	1.437×10^{-7}	2.408×10^{-9}	1.830×10^{-7}	0.785
^{75}As	2.741×10^{-6}	2.055×10^{-4}	2.423×10^{-6}	1.817×10^{-4}	1.131
^{74}Se	3.702×10^{-6}	2.740×10^{-4}	3.340×10^{-6}	2.472×10^{-4}	1.108
^{76}Se	3.453×10^{-6}	2.625×10^{-4}	3.021×10^{-6}	2.296×10^{-4}	1.143
^{77}Se	4.539×10^{-6}	3.495×10^{-4}	3.842×10^{-6}	2.958×10^{-4}	1.181
^{78}Se	8.861×10^{-7}	6.911×10^{-5}	8.734×10^{-7}	6.812×10^{-5}	1.015
^{80}Se	3.329×10^{-9}	2.663×10^{-7}	3.835×10^{-9}	3.068×10^{-7}	0.868
^{82}Se	2.183×10^{-10}	1.790×10^{-8}	2.998×10^{-10}	2.458×10^{-8}	0.728
^{79}Br	3.923×10^{-6}	3.099×10^{-4}	3.361×10^{-6}	2.655×10^{-4}	1.167
^{81}Br	5.347×10^{-6}	4.331×10^{-4}	4.627×10^{-6}	3.748×10^{-4}	1.156
^{78}Kr	4.008×10^{-6}	3.126×10^{-4}	3.439×10^{-6}	2.683×10^{-4}	1.165
^{80}Kr	5.555×10^{-6}	4.444×10^{-4}	4.939×10^{-6}	3.952×10^{-4}	1.125
^{82}Kr	6.824×10^{-6}	5.596×10^{-4}	5.930×10^{-6}	4.862×10^{-4}	1.151
^{83}Kr	5.176×10^{-6}	4.296×10^{-4}	4.477×10^{-6}	3.716×10^{-4}	1.156
^{84}Kr	1.993×10^{-7}	1.674×10^{-5}	2.188×10^{-7}	1.838×10^{-5}	0.911
^{86}Kr	2.968×10^{-9}	2.553×10^{-7}	3.933×10^{-9}	3.383×10^{-7}	0.755
^{85}Rb	4.745×10^{-6}	4.034×10^{-4}	4.054×10^{-6}	3.446×10^{-4}	1.170
^{87}Rb	5.412×10^{-10}	4.709×10^{-8}	7.910×10^{-10}	6.882×10^{-8}	0.684
^{84}Sr	6.263×10^{-6}	5.261×10^{-4}	5.622×10^{-6}	4.723×10^{-4}	1.114
^{86}Sr	6.187×10^{-6}	5.320×10^{-4}	5.363×10^{-6}	4.612×10^{-4}	1.154
^{87}Sr	5.722×10^{-6}	4.978×10^{-4}	5.024×10^{-6}	4.371×10^{-4}	1.139
^{88}Sr	7.836×10^{-6}	6.895×10^{-4}	7.106×10^{-6}	6.254×10^{-4}	1.103

	present		JINA-REACLIB		
Isotope	Abundance	Mass Fraction	Abundance	Mass Fraction	present / JINA
^{89}Y	5.215×10^{-6}	4.641×10^{-4}	4.706×10^{-6}	4.189×10^{-4}	1.108
^{90}Zr	6.974×10^{-6}	6.276×10^{-4}	6.279×10^{-6}	5.651×10^{-4}	1.111
^{91}Zr	9.072×10^{-6}	8.255×10^{-4}	8.454×10^{-6}	7.693×10^{-4}	1.073
^{92}Zr	1.477×10^{-6}	1.358×10^{-4}	1.552×10^{-6}	1.427×10^{-4}	0.952
^{94}Zr	2.162×10^{-12}	2.032×10^{-10}	3.289×10^{-12}	3.092×10^{-10}	0.657
^{96}Zr	5.344×10^{-16}	5.130×10^{-14}	9.719×10^{-16}	9.331×10^{-14}	0.550
^{93}Nb	5.063×10^{-6}	4.709×10^{-4}	4.662×10^{-6}	4.336×10^{-4}	1.086
^{92}Mo	7.933×10^{-6}	7.299×10^{-4}	7.417×10^{-6}	6.824×10^{-4}	1.070
^{94}Mo	8.786×10^{-6}	8.259×10^{-4}	8.332×10^{-6}	7.833×10^{-4}	1.054
^{95}Mo	6.489×10^{-6}	6.164×10^{-4}	6.173×10^{-6}	5.864×10^{-4}	1.051
^{96}Mo	6.122×10^{-7}	5.877×10^{-5}	6.806×10^{-7}	6.533×10^{-5}	0.899
^{97}Mo	1.244×10^{-5}	1.207×10^{-3}	1.134×10^{-5}	1.100×10^{-3}	1.097
^{98}Mo	2.366×10^{-11}	2.319×10^{-9}	3.728×10^{-11}	3.653×10^{-9}	0.635
^{100}Mo	7.645×10^{-10}	7.645×10^{-8}	1.222×10^{-9}	1.222×10^{-7}	0.626
^{96}Ru	2.579×10^{-5}	2.476×10^{-3}	2.307×10^{-5}	2.214×10^{-3}	1.118
^{98}Ru	1.277×10^{-5}	1.252×10^{-3}	1.234×10^{-5}	1.209×10^{-3}	1.035
^{99}Ru	7.115×10^{-6}	7.044×10^{-4}	6.769×10^{-6}	6.702×10^{-4}	1.051
^{100}Ru	1.774×10^{-5}	1.774×10^{-3}	1.536×10^{-5}	1.536×10^{-3}	1.155
^{101}Ru	7.643×10^{-6}	7.719×10^{-4}	6.487×10^{-6}	6.552×10^{-4}	1.178
^{102}Ru	3.290×10^{-7}	3.356×10^{-5}	3.905×10^{-7}	3.983×10^{-5}	0.843
^{104}Ru	2.397×10^{-8}	2.493×10^{-6}	3.397×10^{-8}	3.533×10^{-6}	0.706
^{103}Rh	6.449×10^{-6}	6.642×10^{-4}	5.065×10^{-6}	5.217×10^{-4}	1.273
^{102}Pd	1.144×10^{-5}	1.167×10^{-3}	9.462×10^{-6}	9.651×10^{-4}	1.209
^{104}Pd	1.147×10^{-5}	1.193×10^{-3}	8.377×10^{-6}	8.712×10^{-4}	1.369
^{105}Pd	7.643×10^{-6}	8.025×10^{-4}	5.593×10^{-6}	5.873×10^{-4}	1.367
^{106}Pd	7.233×10^{-8}	7.667×10^{-6}	7.909×10^{-8}	8.384×10^{-6}	0.915
^{108}Pd	4.816×10^{-8}	5.201×10^{-6}	4.653×10^{-8}	5.025×10^{-6}	1.035
^{110}Pd	1.416×10^{-8}	1.557×10^{-6}	1.576×10^{-8}	1.734×10^{-6}	0.898
^{107}Ag	9.103×10^{-6}	9.740×10^{-4}	6.664×10^{-6}	7.130×10^{-4}	1.366
^{109}Ag	1.083×10^{-5}	1.180×10^{-3}	8.809×10^{-6}	9.602×10^{-4}	1.229
^{106}Cd	2.082×10^{-5}	2.207×10^{-3}	1.530×10^{-5}	1.622×10^{-3}	1.361
^{108}Cd	1.698×10^{-5}	1.834×10^{-3}	1.386×10^{-5}	1.496×10^{-3}	1.225
^{110}Cd	2.204×10^{-5}	2.424×10^{-3}	2.174×10^{-5}	2.391×10^{-3}	1.014
^{111}Cd	1.129×10^{-5}	1.254×10^{-3}	1.101×10^{-5}	1.222×10^{-3}	1.025
^{112}Cd	1.676×10^{-6}	1.877×10^{-4}	1.508×10^{-6}	1.689×10^{-4}	1.111
^{113}Cd	1.475×10^{-7}	1.666×10^{-5}	1.815×10^{-7}	2.051×10^{-5}	0.813
^{114}Cd	5.944×10^{-7}	6.777×10^{-5}	6.268×10^{-7}	7.146×10^{-5}	0.948
^{116}Cd	2.752×10^{-11}	3.192×10^{-9}	3.351×10^{-11}	3.887×10^{-9}	0.821
^{113}In	6.121×10^{-6}	6.916×10^{-4}	7.194×10^{-6}	8.129×10^{-4}	0.851

	present		JINA-REACLIB		
Isotope	Abundance	Mass Fraction	Abundance	Mass Fraction	present / JINA
^{115}In	5.714×10^{-7}	6.571×10^{-5}	6.460×10^{-7}	7.429×10^{-5}	0.885
^{112}Sn	1.446×10^{-5}	1.619×10^{-3}	1.755×10^{-5}	1.965×10^{-3}	0.824
^{114}Sn	5.223×10^{-6}	5.954×10^{-4}	7.286×10^{-6}	8.306×10^{-4}	0.717
^{115}Sn	1.507×10^{-6}	1.733×10^{-4}	2.148×10^{-6}	2.470×10^{-4}	0.702
^{116}Sn	1.640×10^{-6}	1.902×10^{-4}	2.365×10^{-6}	2.744×10^{-4}	0.693
^{117}Sn	1.629×10^{-6}	1.906×10^{-4}	2.363×10^{-6}	2.765×10^{-4}	0.689
^{118}Sn	2.145×10^{-6}	2.531×10^{-4}	3.639×10^{-6}	4.294×10^{-4}	0.589
^{119}Sn	1.515×10^{-6}	1.803×10^{-4}	2.771×10^{-6}	3.298×10^{-4}	0.547
^{120}Sn	3.396×10^{-7}	4.076×10^{-5}	6.440×10^{-7}	7.728×10^{-5}	0.527
^{122}Sn	4.516×10^{-8}	5.510×10^{-6}	1.076×10^{-7}	1.313×10^{-5}	0.420
^{124}Sn	6.964×10^{-9}	8.636×10^{-7}	2.148×10^{-8}	2.663×10^{-6}	0.324
^{121}Sb	9.756×10^{-7}	1.181×10^{-4}	2.222×10^{-6}	2.688×10^{-4}	0.439
^{123}Sb	1.108×10^{-7}	1.363×10^{-5}	3.037×10^{-7}	3.736×10^{-5}	0.365
^{120}Te	9.891×10^{-7}	1.187×10^{-4}	2.253×10^{-6}	2.703×10^{-4}	0.439
^{122}Te	5.747×10^{-7}	7.011×10^{-5}	1.523×10^{-6}	1.859×10^{-4}	0.377
^{123}Te	2.426×10^{-7}	2.984×10^{-5}	6.066×10^{-7}	7.461×10^{-5}	0.400
^{124}Te	1.764×10^{-7}	2.188×10^{-5}	4.805×10^{-7}	5.958×10^{-5}	0.367
^{125}Te	3.323×10^{-7}	4.154×10^{-5}	9.621×10^{-7}	1.203×10^{-4}	0.345
^{126}Te	7.003×10^{-8}	8.823×10^{-6}	2.213×10^{-7}	2.788×10^{-5}	0.316
^{128}Te	1.876×10^{-9}	2.402×10^{-7}	8.096×10^{-9}	1.036×10^{-6}	0.232
^{130}Te	1.070×10^{-9}	1.391×10^{-7}	6.173×10^{-9}	8.025×10^{-7}	0.173
^{127}I	2.298×10^{-7}	2.918×10^{-5}	8.853×10^{-7}	1.124×10^{-4}	0.260
^{124}Xe	1.407×10^{-7}	1.745×10^{-5}	4.019×10^{-7}	4.983×10^{-5}	0.350
^{126}Xe	2.430×10^{-7}	3.061×10^{-5}	8.770×10^{-7}	1.105×10^{-4}	0.277
^{128}Xe	1.308×10^{-7}	1.674×10^{-5}	6.117×10^{-7}	7.829×10^{-5}	0.214
^{129}Xe	6.469×10^{-8}	8.345×10^{-6}	2.936×10^{-7}	3.788×10^{-5}	0.220
^{130}Xe	3.526×10^{-8}	4.584×10^{-6}	1.622×10^{-7}	2.108×10^{-5}	0.217
^{131}Xe	6.554×10^{-8}	8.586×10^{-6}	3.287×10^{-7}	4.306×10^{-5}	0.199
^{132}Xe	6.360×10^{-8}	8.396×10^{-6}	3.971×10^{-7}	5.242×10^{-5}	0.160
^{134}Xe	2.333×10^{-10}	3.126×10^{-8}	2.077×10^{-9}	2.784×10^{-7}	0.112
^{136}Xe	5.197×10^{-14}	7.068×10^{-12}	6.333×10^{-13}	8.613×10^{-11}	0.082
^{133}Cs	1.949×10^{-8}	2.592×10^{-6}	1.598×10^{-7}	2.125×10^{-5}	0.122
^{130}Ba	2.616×10^{-8}	3.401×10^{-6}	1.325×10^{-7}	1.723×10^{-5}	0.197
^{132}Ba	3.532×10^{-8}	4.662×10^{-6}	2.596×10^{-7}	3.427×10^{-5}	0.136
^{134}Ba	1.727×10^{-8}	2.314×10^{-6}	1.823×10^{-7}	2.443×10^{-5}	0.095
^{135}Ba	4.960×10^{-9}	6.696×10^{-7}	5.418×10^{-8}	7.315×10^{-6}	0.092
^{136}Ba	4.510×10^{-9}	6.133×10^{-7}	4.925×10^{-8}	6.698×10^{-6}	0.092
^{137}Ba	2.115×10^{-9}	2.898×10^{-7}	2.413×10^{-8}	3.305×10^{-6}	0.088
^{138}Ba	2.083×10^{-11}	2.875×10^{-9}	3.574×10^{-10}	4.932×10^{-8}	0.058

	present		JINA-REACLIB		
Isotope	Abundance	Mass Fraction	Abundance	Mass Fraction	present / JINA
^{138}La	1.404×10^{-9}	1.938×10^{-7}	1.866×10^{-8}	2.575×10^{-6}	0.075
^{139}La	1.357×10^{-9}	1.886×10^{-7}	2.422×10^{-8}	3.366×10^{-6}	0.056
^{129}Ce	2.696×10^{-16}	3.478×10^{-14}	5.165×10^{-16}	6.663×10^{-14}	0.522
^{136}Ce	3.147×10^{-10}	4.280×10^{-8}	3.196×10^{-9}	4.346×10^{-7}	0.098
^{138}Ce	5.707×10^{-10}	7.876×10^{-8}	9.234×10^{-9}	1.274×10^{-6}	0.062
^{140}Ce	1.746×10^{-10}	2.445×10^{-8}	4.253×10^{-9}	5.954×10^{-7}	0.041
^{142}Ce	4.906×10^{-13}	6.967×10^{-11}	1.699×10^{-11}	2.412×10^{-9}	0.029
^{129}Pr	4.856×10^{-24}	6.264×10^{-22}	3.846×10^{-24}	4.962×10^{-22}	1.263
^{134}Pr	6.378×10^{-18}	8.547×10^{-16}	1.544×10^{-17}	2.070×10^{-15}	0.413
^{141}Pr	6.327×10^{-11}	8.920×10^{-9}	1.369×10^{-9}	1.930×10^{-7}	0.046
^{142}Nd	1.893×10^{-11}	2.688×10^{-9}	4.909×10^{-10}	6.970×10^{-8}	0.039
^{143}Nd	9.292×10^{-12}	1.329×10^{-9}	2.762×10^{-10}	3.949×10^{-8}	0.034
^{144}Nd	2.301×10^{-12}	3.313×10^{-10}	8.104×10^{-11}	1.167×10^{-8}	0.028
^{145}Nd	8.205×10^{-13}	1.190×10^{-10}	3.237×10^{-11}	4.694×10^{-9}	0.025
^{146}Nd	1.361×10^{-13}	1.987×10^{-11}	6.200×10^{-12}	9.053×10^{-10}	0.022
^{148}Nd	2.808×10^{-15}	4.156×10^{-13}	1.657×10^{-13}	2.452×10^{-11}	0.017
^{150}Nd	5.820×10^{-17}	8.730×10^{-15}	4.153×10^{-15}	6.230×10^{-13}	0.014
^{144}Sm	1.804×10^{-14}	2.598×10^{-12}	4.981×10^{-13}	7.173×10^{-11}	0.036
^{146}Sm	6.504×10^{-15}	9.496×10^{-13}	2.411×10^{-13}	3.519×10^{-11}	0.027
^{147}Sm	8.528×10^{-14}	1.254×10^{-11}	3.601×10^{-12}	5.293×10^{-10}	0.024
^{148}Sm	2.864×10^{-14}	4.239×10^{-12}	1.144×10^{-12}	1.693×10^{-10}	0.025
^{149}Sm	3.370×10^{-14}	5.022×10^{-12}	1.524×10^{-12}	2.270×10^{-10}	0.022
^{150}Sm	5.227×10^{-15}	7.840×10^{-13}	2.631×10^{-13}	3.946×10^{-11}	0.020
^{152}Sm	5.271×10^{-15}	8.013×10^{-13}	3.277×10^{-13}	4.982×10^{-11}	0.016
^{154}Sm	3.679×10^{-16}	5.666×10^{-14}	2.967×10^{-14}	4.569×10^{-12}	0.012
^{151}Eu	1.780×10^{-14}	2.687×10^{-12}	9.662×10^{-13}	1.459×10^{-10}	0.018
^{153}Eu	1.764×10^{-15}	2.699×10^{-13}	1.251×10^{-13}	1.914×10^{-11}	0.014
^{148}Gd	1.827×10^{-19}	2.704×10^{-17}	7.369×10^{-18}	1.091×10^{-15}	0.025
^{150}Gd	4.630×10^{-18}	6.944×10^{-16}	1.614×10^{-16}	2.421×10^{-14}	0.029
^{152}Gd	8.343×10^{-18}	1.268×10^{-15}	3.606×10^{-16}	5.481×10^{-14}	0.023
^{154}Gd	2.228×10^{-17}	3.431×10^{-15}	1.188×10^{-15}	1.829×10^{-13}	0.019
^{155}Gd	1.145×10^{-16}	1.775×10^{-14}	9.183×10^{-15}	1.423×10^{-12}	0.012
^{156}Gd	3.353×10^{-17}	5.230×10^{-15}	2.666×10^{-15}	4.160×10^{-13}	0.013
^{157}Gd	1.535×10^{-17}	2.410×10^{-15}	1.325×10^{-15}	2.080×10^{-13}	0.012
^{158}Gd	3.032×10^{-18}	4.790×10^{-16}	2.935×10^{-16}	4.637×10^{-14}	0.010
^{160}Gd	5.870×10^{-19}	9.392×10^{-17}	7.461×10^{-17}	1.194×10^{-14}	0.008
^{159}Tb	1.887×10^{-18}	3.001×10^{-16}	2.042×10^{-16}	3.247×10^{-14}	0.009

Bibliography

Note: This bibliography lists the page number, or numbers, of every citation of the reference that occurs in the text. This list of pages is located directly after each reference.

[Abb99] D. J. Abbott, W. G. Heyes, E. Jastrzembski, R. W. MacLeod, C. Timmer, & E. Wolin. *CODA Performance in the Real World. Real Time Conference, 1999. Santa Fe 1999. 11th IEEE NPSS*, pp. 119–122 (1999).
Cited on p. 37

[Abr64] M. Abramowitz & I. Stegun. *Handbook of Mathematical Functions with Formulas, Graphs, and Mathematical Tables.* Dover Publications, New York (1964).
Cited on p. 90

[Ago03] G. D'Agostini. *Bayesian Reasoning in Data Analysis: A Critical Introduction.* World Scientific Publishing Company, Singapore (2003).
Cited on p. 86

[Ahm08] M. W. Ahmed, M. A. Blackston, M. D. Busch, A. S. Crowell, S. S. Henshaw, C. R. Howell, J. Li, P. Kingsberry, B. A. Perdue, S. Stave, H. R. Weller, M. Emamian, S. Mikhailov, G. Swift, Y. K. Wu, R. M. Prior, & M. C. Spraker. *Precise Determination of Total Absolute γ-ray Intensity at HIγS.* TUNL Progress Report XLVII, Triangle Universities Nuclear Laboratory (2008).
Cited on p. 23

[Ajz90] F. Ajzenberg-Selove. *Energy Levels of Light Nuclei A = 11–12.* Nucl. Phys. A **506**, 1 (1990).
Cited on p. 2, 4, 113, 114, 115, 117

[Alc12] M. Alcorta, M. J. G. Borge, M. Cubero, C. A. Diget, R. Domínguez-Reyes, *et al. Properties of ^{12}C Resonances Determined from the $^{10}B(^3He,p\alpha\alpha\alpha)$ and $^{11}B(^3He,d\alpha\alpha\alpha)$ Reactions Studied in Complete Kinematics.* Phys. Rev. C **86**, 064306 (2012).
Cited on p. 7, 8, 115

[Ald56] K. Alder, A. Bohr, T. Huus, B. Mottelson, & A. Winther. *Study of Nuclear Structure by Electromagnetic Excitation with Accelerated Ions.* Rev. Mod. Phys. **28**, 432 (1956).
Cited on p. 95

[Ang99] C. Angulo, M. Arnould, M. Rayet, P. Descouvemont, D. Baye, *et al. A Compilation of Charged-Particle Induced Thermonuclear Reaction Rates.* Nucl. Phys. A **656**, 3 (1999).
Cited on p. 9, 10, 102, 105, 107, 118

[Ann98] P. Annis, S. Aoki, G. Brooijmans, J. Brunner, J. Dupraz, *et al. The CHORUS Scintillating Fiber Tracker and Opto-Electronic Readout System.* Nucl. Instrum. Methods A **412**, 19 (1998).
Cited on p. 29, 30

[Arc12] A. Arcones, C. Fröhlich, & G. Martínez-Pinedo. *Impact of Supernova Dynamics on the νp-Process.* Astrophys. J. **750**, 18 (2012).
Cited on p. 107, 108, 123

[Arn] O. Arnon. *Optical Engineering, 78a Shenkin Street, Tel Aviv.*
Cited on p. 30

[Assu06] M. Assunção, M. Fey, A. Lefebvre-Schuhl, J. Kiener, V. Tatischeff, *et al. E*1 *and E*2 *S-Factors of* $^{12}C(\alpha,\gamma)^{16}O$ *from γ-Ray Angular Distributions with a 4 π-Detector Array.* Phys. Rev. C **73**, 055801 (2006).
Cited on p. 72

[Ban97] P. Bandžuch, M. Morháč, & J. Krištiak. *Study of the Van Cittert and Gold Iterative Methods of Deconvolution and their Application in the Deconvolution of Experimental Spectra of Positron Annihilation.* Nucl. Instrum. Methods A **384**, 506 (1997).
Cited on p. 44

[Bar74] A. R. Barnett, D. H. Feng, J. W. Steed, & L. J. B. Goldfarb. *Coulomb Wave Functions for All Real η and ρ.* Comput. Phys. Commun. **8**, 377 (1974).
Cited on p. 90

[Ber98] M. J. Berger, J. H. Hubbell, S. M. Seltzer, J. Chang, J. S. Coursey, R. Sukumar, D. S. Zucker, & K. Olsen. *XCOM: Photon Cross Sections Database.* `http://www.nist.gov/physlab/data/xcom/index.cfm` NBSIR 87-3597, National Institute of Standards and Technology (1998).
Cited on p. 23, 41, 83

[Bet39] H. A. Bethe. *Energy Production in Stars.* Phys. Rev. **55**, 434 (1939).
Cited on p. 3

[Bia99] S. F. Biagi. *Monte Carlo Simulation of Electron Drift and Diffusion in Counting Gases Under the Influence of Electric and Magnetic Fields.* Nucl. Instrum. Methods A **421**, 234 (1999).
Cited on p. 60

[Bla52] J. M. Blatt & V. F. Weisskopf. *Theoretical Nuclear Physics*. John Wiley & Sons, Inc., New York (1952).
Cited on p. 90, 94, 95

[Boh75] A. Bohr & B. R. Mottelson. *Nuclear Deformations*, Volume II of *Nuclear Structure*. W. A. Benjamin, Inc., New York (1975).
Cited on p. 5, 112, 113

[Böh05] J. K. Böhlke, J. R. de Laeter, P. De Bièvre, H. Hidaka, H. S. Peiser, K. J. R. Rosman, & P. D. P. Taylor. *Isotopic Compositions of the Elements, 2001*. J. Phys. Chem. Ref. Data **34**, 57 (2005).
Cited on p. 84

[Bor78] E. Borie & G. A. Rinker. *Improved Calculation of the Muonic-Helium Lamb Shift*. Phys. Rev. A **18**, 324 (1978).
Cited on p. 112

[Bra12] E. Bravo & G. Martínez-Pinedo. *Sensitivity Study of Explosive Nucleosynthesis in Type Ia Supernovae: Modification of Individual Thermonuclear Reaction Rates*. Phys. Rev. C **85**, 055805 (2012).
Cited on p. 8

[Bre79] A. Breskin, G. Charpak, S. Majewski, G. Melchart, G. Petersen, & F. Sauli. *The Multistep Avalanche Chamber: A New Family of Fast, High-Rate Particle Detectors*. Nucl. Instrum. Methods A **161**, 19 (1979).
Cited on p. 25

[Bri52] R. Britten. *The Scattering of 31.5-Mev Protons from Several Elements*. Phys. Rev. **88**, 283 (1952).
Cited on p. 4

[Bru97] R. Brun & F. Rademakers. *ROOT — An Object Oriented Data Analysis Framework*. Nucl. Instrum. Methods A **389**, 81 (1997).
Cited on p. 39

[Buc06] L. R. Buchmann & C. A. Barnes. *Nuclear Reactions in Stellar Helium Burning and Later Hydrostatic Burning Stages*. Nucl. Phys. A **777**, 254 (2006).
Cited on p. 8

[Bur57] E. M. Burbidge, G. R. Burbidge, W. A. Fowler, & F. Hoyle. *Synthesis of the Elements in Stars*. Rev. Mod. Phys. **29**, 547 (1957).
Cited on p. 8

[Cam95] M. C. A. Campos, P. von Neumann-Cosel, F. Neumeyer, A. Richter, G. Schrieder, E. Spamer, B. A. Brown, & R. J. Peterson. *Isospin Mixing in the Electroexcitation of the E_x = 10.84 MeV, $J^\pi; T = 1^-; 0$ State in ^{12}C*

at Low Momentum Transfers. Phys. Lett. B **349**, 433 (1995).
Cited on p. 111

[Cha78] G. Charpak & F. Sauli. *The Multistep Avalanche Chamber: A New High-Rate, High-Accuracy Gaseous Detector.* Phys. Lett. B **78**, 523 (1978). 25

[Cha87] G. Charpak, J.-P. Fabre, F. Sauli, M. Suzuki, & W. Dominik. *An Optical, Proportional, Continuously Operating Avalanche Chamber.* Nucl. Instrum. Methods A **258**, 177 (1987).
Cited on p. 25

[Cha06] M. B. Chadwick, P. Obložinský, M. Herman, N. M. Greene, R. D. McKnight, *et al. ENDF/B-VII.0: Next Generation Evaluated Nuclear Data Library for Nuclear Science and Technology.* Nucl. Data Sheets **107**, 2931 (2006).
Cited on p. 43

[Che07] M. Chernykh, H. Feldmeier, T. Neff, P. von Neumann-Cosel, & A. Richter. *Structure of the Hoyle State in* ^{12}C. Phys. Rev. Lett. **98**, 032501 (2007).
Cited on p. 5, 11, 14, 15, 113, 116

[Che10] M. Chernykh, H. Feldmeier, T. Neff, P. von Neumann-Cosel, & A. Richter. *Pair Decay Width of the Hoyle State and its Role for Stellar Carbon Production.* Phys. Rev. Lett. **105**, 022501 (2010).
Cited on p. 106

[Coh65] S. Cohen & D. Kurath. *Effective Interactions for the 1p Shell.* Nucl. Phys. **73**, 1 (1965).
Cited on p. 11, 115

[Coo57] C. W. Cook, W. A. Fowler, C. C. Lauritsen, & T. Lauritsen. *B^{12}, C^{12}, and the Red Giants.* Phys. Rev. **107**, 508 (1957).
Cited on p. 4

[Cyb10] R. H. Cyburt, A. M. Amthor, R. Ferguson, Z. Meisel, K. Smith, S. Warren, A. Heger, R. D. Hoffman, T. Rauscher, A. Sakharuk, H. Schatz, F. K. Thielemann, & M. Wiescher. *The JINA REACLIB Database: Its Recent Updates and Impact on Type-I X-ray Bursts.* Astrophys. J. Suppl. Ser. **189**, 240 (2010).
Cited on p. 9, 10, 105, 107, 108, 118, 119, 120, 123

[Des87] P. Descouvemont & D. Baye. *Microscopic Theory of the* $^{8}\mathrm{Be}(\alpha,\gamma)^{12}C$ *Reaction in a Three-Cluster Model.* Phys. Rev. C **36**, 54 (1987).
Cited on p. 11, 111, 116

[Des10] P. Descouvemont & D. Baye. *The R-matrix Theory.* Rep. Prog. Phys. **73**, 036301 (2010).
Cited on p. 90, 98, 112

[Die11] R. de Diego, E. Garrido, D. V. Fedorov, & A. S. Jensen. *The Triple Alpha Reaction Rate and the 2^+ Resonances in ^{12}C.* Phys. Lett. B **695**, 324 (2011).
Cited on p. 10

[Dig05] C. A. Diget, F. C. Barker, M. J. G. Borge, J. Cederkäl, V. N. Fedosseev, *et al. Properties of the ^{12}C 10 MeV State Determined Through β-Decay.* Nucl. Phys. A **760**, 3 (2005).
Cited on p. 6, 7, 8, 115

[Dun53] D. N. F. Dunbar, R. E. Pixley, W. A. Wenzel, & W. Whaling. *The 7.68-MeV State in C^{12}.* Phys. Rev. **92**, 649 (1953).
Cited on p. 4

[Dye74] P. Dyer & C. A. Barnes. *The $^{12}C(\alpha,\gamma)^{16}O$ Reaction and Stellar Helium Burning.* Nucl. Phys. A **233**, 495 (1974).
Cited on p. 72, 91

[Ebr12] J.-P. Ebran, E. Khan, T. Nikšić, & D. Vretenar. *How Atomic Nuclei Cluster.* Nature (London) **487**, 341 (2012).
Cited on p. 5

[Eid05] M. E. Eid. *Astrophysics: The Process of Carbon Creation.* Nature (London) **433**, 117 (2005).
Cited on p. 8

[Epe09] E. Epelbaum, H. Krebs, D. Lee, & U.-G. Meißner. *Ground-State Energy of Dilute Neutron Matter at Next-to-Leading Order in Lattice Chiral Effective Field Theory.* Eur. Phys. J. A **40**, 199 (2009).
Cited on p. 15

[Epe10a] E. Epelbaum, H. Krebs, D. Lee, & U.-G. Meißner. *Lattice Calculations for A = 3, 4, 6, 12 Nuclei Using Chiral Effective Field Theory.* Eur. Phys. J. A **45**, 335 (2010).
Cited on p. 15, 16

[Epe10b] E. Epelbaum, H. Krebs, D. Lee, & U.-G. Meißner. *Lattice Effective Field Theory Calculations for A =3, 4, 6, 12 Nuclei.* Phys. Rev. Lett. **104**, 142501 (2010).
Cited on p. 15, 118

[Epe11] E. Epelbaum, H. Krebs, D. Lee, & U.-G. Meißner. *Ab Initio Calculation of the Hoyle State.* Phys. Rev. Lett. **106**, 192501 (2011).
Cited on p. 16, 118

[Epe12] E. Epelbaum, H. Krebs, T. A. Lähde, D. Lee, & U.-G. Meißner. *Structure and Rotations of the Hoyle State.* Phys. Rev. Lett. **109**, 252501 (2012).
Cited on p. 11, 16, 113, 116

[Epe13] E. Epelbaum, H. Krebs, T. A. Lähde, D. Lee, & U.-G. Meißner. *Viability of Carbon-Based Life as a Function of the Light Quark Mass.* Phys. Rev. Lett. **110**, 112502 (2013).
Cited on p. 118

[Esk98] E. Eskut, A. Kayis, G. Onengüt, R. van Dantzig, M. de Jong, *et al. A Search for $\nu_\mu \to \nu_\tau$ Oscillation.* Phys. Lett. B **424**, 202 (1998).
Cited on p. 29

[Fre09] M. Freer, H. Fujita, Z. Buthelezi, J. Carter, R. W. Fearick, S. V. Förtsch, R. Neveling, S. M. Perez, P. Papka, F. D. Smit, J. A. Swartz, & I. Usman. *2^+ Excitation of the ^{12}C Hoyle State.* Phys. Rev. C **80**, 041303 (2009).
Cited on p. 6, 8, 90, 115

[Fre12a] M. Freer. *Nuclear Physics: Nucleons Come Together.* Nature (London) **487**, 309 (2012).
Cited on p. 5, 111

[Fre12b] M. Freer, M. Itoh, T. Kawabata, H. Fujita, H. Akimune, *et al. Consistent Analysis of the 2^+ Excitation of the ^{12}C Hoyle State Populated in Proton and α-Particle Inelastic Scattering.* Phys. Rev. C **86**, 034320 (2012).
Cited on p. 6, 8, 90, 112, 115

[Frö06] C. Fröhlich, G. Martínez-Pinedo, M. Liebendörfer, F.-K. Thielemann, E. Bravo, W. R. Hix, K. Langanke, & N. T. Zinner. *Neutrino-Induced Nucleosynthesis of $A > 64$ Nuclei: The νp Process.* Phys. Rev. Lett. **96**, 142502 (2006).
Cited on p. 9, 107, 108, 123

[Frö13] C. Frölich. private communication (2013).
Cited on p. 107, 108, 118

[Fun03] Y. Funaki, A. Tohsaki, H. Horiuchi, P. Schuck, & G. Röpke. *Analysis of Previous Microscopic Calculations for the Second 0^+ State in ^{12}C in Terms of 3-α Particle Bose-Condensed State.* Phys. Rev. C **67**, 051306 (2003).
Cited on p. 13

[Fun05] Y. Funaki, A. Tohsaki, H. Horiuchi, P. Schuck, & G. Röpke. *Resonance States in ^{12}C and α-Particle Condensation.* Eur. Phys. J. A **24**, 321 (2005).
Cited on p. 13

[Fyn05] H. O. U. Fynbo, C. A. Diget, U. C. Bergmann, M. J. G. Borge, J. Cederkall, *et al. Revised Rates for the Stellar Triple-α Process from Measurement of ^{12}C Nuclear Resonances.* Nature (London) **433**, 136 (2005).
Cited on p. 6, 7, 8, 9, 10, 105, 107, 108, 115, 123

[Fyn11] H. O. U. Fynbo & M. Freer. *Rotations of the Hoyle State in Carbon-12.* Physics **4**, 94 (2011).
Cited on p. 4, 5

[Gai10] M. Gai, M. W. Ahmed, S. C. Stave, W. R. Zimmerman, A. Breskin, B. Bromberger, R. Chechik, V. Dangendorf, T. Delbar, R. H. France III, S. S. Henshaw, T. J. Kading, P. P. Martel, J. E. R. McDonald, P.-N. Seo, K. Tittelmeier, H. R. Weller, & A. H. Young. *An Optical Readout TPC (O-TPC) for Studies in Nuclear Astrophysics with Gamma-Ray Beams at HIGS.* JINST **5**, P12004 (2010).
Cited on p. 25

[Gug47] K. M. Guggenheimer, H. Heitler, & C. F. Powell. *The Elastic Scattering of 6.5 MeV Deuterons by Deuterium, Helium, and Other Light Elements.* Proc. R. Soc. London, Ser. A **190**, 196 (1947).
Cited on p. 4

[Gui52] W. H. Guier, H. W. Bertini, & J. H. Roberts. *Energy Levels in C^{12} from $Be^9(\alpha, n)C^{12}$.* Phys. Rev. **85**, 426 (1952).
Cited on p. 4

[Hol40] M. G. Holloway & B. L. Moore. *The Disintegration of N^{14} and N^{15} by Deuterons.* Phys. Rev. **58**, 847 (1940).
Cited on p. 4

[Hoy53] F. Hoyle, D. N. F. Dunbar, W. A. Wenzel, & W. Whaling. *A State in C^{12} Predicted from Astrophysical Evidence.* Phys. Rev. **92**, 1095 (1953).
Cited on p. 3

[Hoy54] F. Hoyle. *On Nuclear Reactions Occuring in Very Hot Stars. I. The Synthesis of Elements from Carbon to Nickel.* Astrophys. J. Suppl. Ser. **1**, 121 (1954).
Cited on p. 4

[Hug58] D. J. Hughes, R. L. Zimmerman, & R. E. Chrien. *Strength Functions for Deformed Nuclei.* Phys. Rev. Lett. **1**, 461 (1958).
Cited on p. 111

[Hyl10] S. Hyldegaard, M. Alcorta, B. Bastin, M. J. G. Borge, R. Boutami, *et al. R-Matrix Analysis of the β Decays of ^{12}N and ^{12}B.* Phys. Rev. C **81**, 024303 (2010).
Cited on p. 7, 8, 115

[IEE08] *IEEE Standard for a High-Performance Serial Bus.* IEEE Std 1394-2008 pp. 1–906 (2008).
Cited on p. 37

[Ike68] K. Ikeda, N. Takigawa, & H. Horiuchi. *The Systematic Structure-Change into the Molecule-like Structures in the Self-Conjugate 4n Nuclei.* Prog. Theor. Phys. Suppl. **E68**, 464 (1968).
Cited on p. 4

[Ito04] M. Itoh, H. Akimune, M. Fujiwara, U. Garg, H. Hashimoto, T. Kawabata, K. Kawase, S. Kishi, T. Murakami, K. Nakanishi, Y. Nakatsugawa, B. Nayak, S. Okumura, H. Sakaguchi, H. Takeda, S. Terashima, M. Uchida, Y. Yasuda, M. Yosoi, & J. Zenihiro. *Study of the Cluster State at E_x = 10.3 MeV in ^{12}C.* Nucl. Phys. A **738**, 268 (2004).
Cited on p. 6, 8, 115

[Ito11] M. Itoh, H. Akimune, M. Fujiwara, U. Garg, N. Hashimoto, T. Kawabata, K. Kawase, S. Kishi, T. Murakami, K. Nakanishi, Y. Nakatsugawa, B. K. Nayak, S. Okumura, H. Sakaguchi, H. Takeda, S. Terashima, M. Uchida, Y. Yasuda, M. Yosoi, & J. Zenihiro. *Candidate for the 2^+ Excited Hoyle State at E_x∼10 MeV in ^{12}C.* Phys. Rev. C **84**, 054308 (2011).
Cited on p. 6, 8, 115

[Kar95] S. Karataglidis, P. J. Dortmans, K. Amos, & R. de Swiniarski. *Fully Microscopic Model of 200 MeV Proton-^{12}C Elastic and Inelastic Scattering.* Phys. Rev. C **52**, 861 (1995).
Cited on p. 11, 111

[Kho11] D. T. Khoa, D. C. Cuong, & Y. Kanada-En'yo. *Hindrance of the Excitation of the Hoyle State and the Ghost of the 2_2^+ State in ^{12}C.* Phys. Lett. B **695**, 469 (2011).
Cited on p. 115

[Lan58] A. M. Lane & R. G. Thomas. *R-Matrix Theory of Nuclear Reactions.* Rev. Mod. Phys. **30**, 257 (1958).
Cited on p. 90, 91, 96, 97

[Lit96] V. N. Litvinenko, B. Burnham, J. M. J. Madey, S. H. Park, & Y. K. Wu. *Duke Storage Ring UV/VUV FEL: Status and Prospects.* Nucl. Instrum. Methods A **375**, 46 (1996).
Cited on p. 19

[Lit97] V. N. Litvinenko, B. Burnham, M. Emamian, N. Hower, J. M. J. Madey, *et al.* *Gamma-Ray Production in a Storage Ring Free-Electron Laser.* Phys. Rev. Lett. **78**, 4569 (1997).
Cited on p. 17, 20

[Lit01] V. N. Litvinenko, S. F. Mikhailov, N. A. Vinokurov, N. G. Gavrilov, G. N. Kulipanov, O. A. Shevchenko, & P. D. Vobly. *Helical Wigglers for the OK-5 Storage Ring VUV FEL at Duke.* Nucl. Instrum. Methods A **475**, 247

(2001).
Cited on p. 19

[Lyo86] L. Lyons. *Statistics for Nuclear and Particle Physicists*. Cambridge University Press, Cambridge (1986).
Cited on p. 72

[Mal51] R. Malm & W. W. Buechner. *Alpha-Particle Groups from the $N^{14}(d,\alpha)C^{12}$ and $N^{15}(d,\alpha)C^{13}$ Reactions*. Phys. Rev. **81**, 519 (1951).
Cited on p. 4

[Mer92] A. C. Merchant & W. D. M. Rae. *Systematics of Alpha-Chain States in 4N-Nuclei*. Nucl. Phys. A **549**, 431 (1992).
Cited on p. 112

[Mie07a] K. Miernik, W. Dominik, H. Czyrkowski, R. Dąbrowski, A. Fomitchev, M. Golovkov, Z. Janas, W. Kuśmierz, M. Pfützner, A. Rodin, S. Stepantsov, R. Slepniev, G. M. Ter-Akopian, & R. Wolski. *Optical Time Projection Chamber for Imaging Nuclear Decays*. Nucl. Instrum. Methods A **581**, 194 (2007).
Cited on p. 25

[Mie07b] K. Miernik, W. Dominik, Z. Janas, M. Pfützner, L. Grigorenko, C. R. Bingham, H. Czyrkowski, M. Ćwiok, I. G. Darby, R. Dąbrowski, T. Ginter, R. Grzywacz, M. Karny, A. Korgul, W. Kuśmierz, S. N. Liddick, M. Rajabali, K. Rykaczewski, & A. Stolz. *Two-Proton Correlations in the Decay of ^{45}Fe*. Phys. Rev. Lett. **99**, 192501 (2007).
Cited on p. 25

[Mor56] H. Morinaga. *Interpretation of Some of the Excited States of 4n Self-Conjugate Nuclei*. Phys. Rev. **101**, 254 (1956).
Cited on p. 1, 5, 111, 112, 117

[Mor66] H. Morinaga. *On the Spin of a Broad State Around 10 MeV in ^{12}C*. Phys. Lett. **21**, 78 (1966).
Cited on p. 112

[Nav00a] P. Navrátil, J. P. Vary, & B. R. Barrett. *Large-Basis Ab Initio No-Core Shell Model and its Application to ^{12}C*. Phys. Rev. C **62**, 054311 (2000).
Cited on p. 11

[Nav00b] P. Navrátil, J. P. Vary, & B. R. Barrett. *Properties of ^{12}C in the Ab Initio Nuclear Shell Model*. Phys. Rev. Lett. **84**, 5728 (2000).
Cited on p. 11, 111

[Nef12] T. Neff. private communication (2012).
Cited on p. 11, 116

[NIM64] U.S. AEC Report TID-20893, Standard Nuclear Instrument Modules (Specifications of the NIM System) (1964).
Cited on p. 31

[Oer06] W. von Oertzen, M. Freer, & Y. Kanada-En'yo. *Nuclear Clusters and Nuclear Molecules*. Phys. Rep. **432**, 43 (2006).
Cited on p. 5

[Öpi51] E. J. Öpik. *Stellar Models with Variable Composition. II. Sequences of Models with Energy Generation Proportional to the Fifteenth Power of Temperature*. Proc. of the Royal Irish Academy A **54**, pp. 49 (1951).
Cited on p. 3

[Opt] Optimax Systems, Inc. *6367 Dean Parkway, Ontario, New York*.
Cited on p. 30

[Per10] B. Perdue. *Measurements of the Absolute Cross Section of the Three-body Photodisintegration of ^3He Between E_γ = 11.4 MeV and 14.7 MeV at HIγS*. Ph.D. thesis, Duke University (2010).
Cited on p. 23

[Pot84] D. M. Potter. *Optical Readout of a High Resolution Parallel Plate Avalanche Chamber*. Nucl. Instrum. Methods A **228**, 56 (1984).
Cited on p. 25

[Rae64] H. Raether. *Electron Avalanches and Breakdown in Gases*. Butterworth, London (1964).
Cited on p. 48, 77

[Rol88] C. E. Rolfs & W. S. Rodney. *Cauldrons in the Cosmos*. University of Chicago Press, Chicago (1988).
Cited on p. 8, 100, 101

[Rot04] R. Roth, T. Neff, H. Hergert, & H. Feldmeier. *Nuclear Structure Based on Correlated Realistic Nucleon-Nucleon Potentials*. Nucl. Phys. A **745**, 3 (2004).
Cited on p. 14

[Rot05] R. Roth, H. Hergert, P. Papakonstantinou, T. Neff, & H. Feldmeier. *Matrix Elements and Few-Body Calculations Within the Unitary Correlation Operator Method*. Phys. Rev. C **72**, 034002 (2005).
Cited on p. 14

[Sal52] E. E. Salpeter. *Nuclear Reactions in Stars without Hydrogen.* Astrophys. J. **115**, 326 (1952).
Cited on p. 3

[Sch00] E. Schreiber. *Measurement of a High-Intensity Gamma-Ray Beam and the Analyzing Power for* $^2He(\vec{\gamma}, n)p$ *Near Threshold.* Ph.D. thesis, Duke University (2000).
Cited on p. 49

[Smi12] F. D. Smit, F. Nemulodi, Z. Buthelezi, J. Carter, R. W. Fearick, S. V. Förtsch, M. Freer, H. Fujita, M. Jingo, C. O. Kureba, J. Mabiala, J. Mira, R. Neveling, P. Papka, G. F. Steyn, J. A. Swartz, I. T. Usman, & J. J. van Zyl. *No Evidence of an 11.16 MeV* 2^+ *State in* ^{12}C. Phys. Rev. C **86**, 037301 (2012).
Cited on p. 7, 8, 115

[Sta08] S. Stave, M. W. Ahmed, & H. R. Weller. *Beam Intensity Determination at HI*γ*S Using the* $^2H(\gamma, n)p$ *Reaction.* TUNL Progress Report XLVII, Triangle Universities Nuclear Laboratory (2008).
Cited on p. 24

[Sun09a] C. Sun. *Characterizations and Diagnostics of Compton Light Source.* Ph.D. thesis, Duke University (2009).
Cited on p. 22, 44

[Sun09b] C. Sun, Y. K. Wu, G. Rusev, & A. P. Tonchev. *End-to-End Spectrum Reconstruction Method for Analyzing Compton Gamma-ray Beams.* Nucl. Instrum. Methods A **605**, 312 (2009).
Cited on p. 25, 43, 44

[Sun11] C. Sun & Y. K. Wu. *Theoretical and Simulation Studies of Characteristics of a Compton Light Source.* Phys. Rev. Spec. Top. Accel. Beams **14**, 044701 (2011).
Cited on p. 22

[Suz72] Y. Suzuki, H. Horiuchi, & K. Ikeda. *Study of* α *Chain States through Their Decay Widths.* Prog. Theor. Phys. **47**, 1517 (1972).
Cited on p. 112

[Tei52] T. Teichmann & E. P. Wigner. *Sum Rules in the Dispersion Theory of Nuclear Reactions.* Phys. Rev. **87**, 123 (1952).
Cited on p. 95

[Til04] D. R. Tilley, J. H. Kelley, J. L. Godwin, D. J. Millener, J. E. Purcell, C. G. Sheu, & H. R. Weller. *Energy Levels of Light Nuclei A=8,9,10.* Nucl. Phys. A

745, 155 (2004).
Cited on p. 3, 97, 112

[Toh94] A. Tohsaki. *New Effective Internucleon Forces in Microscopic α-Cluster Model*. Phys. Rev. C **49**, 1814 (1994).
Cited on p. 13

[Toh01] A. Tohsaki, H. Horiuchi, P. Schuck, & G. Röpke. *Alpha Cluster Condensation in ^{12}C and ^{16}O*. Phys. Rev. Lett. **87**, 192501 (2001).
Cited on p. 12, 13, 14

[VME87] *IEEE Standard for a Versatile Backplane Bus: VMEbus*. ANSI/IEEE Std. 1014-1987 (1987).
Cited on p. 31, 32

[Vog62] E. Vogt. *Theory of Low Energy Nuclear Reactions*. Rev. Mod. Phys. **34**, 723 (1962).
Cited on p. 97, 111

[Wan11] S. Wanajo, H.-T. Janka, & S. Kubono. *Uncertainties in the νp-Process: Supernova Dynamics Versus Nuclear Physics*. Astrophys. J. **729**, 46 (2011).
Cited on p. 9, 10

[War69] E. K. Warburton & J. Weneser. *The Role of Isospin in Electromagnetic Transitions. Isospin in Nuclear Physics* (D. H. Wilkinson, editor), pp. 152–228 (North-Holland Publishing Company, Amsterdam, 1969).
Cited on p. 110

[Wei06] L. Weissman, M. Gai, A. Breskin, R. Chechik, V. Dangendorf, K. Tittelmeier, & H. R. Weller. *Amplification and Scintillation Properties of Oxygen-Rich Gas Mixtures for Optical-TPC Applications*. JINST **1**, P05002 (2006).
Cited on p. 26

[Wel09] H. R. Weller, M. W. Ahmed, H. Gao, W. Tornow, Y. K. Wu, M. Gai, & R. Miskimen. *Research Opportunities at the Upgraded HIγS Facility*. Prog. Part. Nucl. Phys. **62**, 257 (2009).
Cited on p. 1, 18

[Win09] Developed by Wind River Systems, Inc., Alameda, CA, USA. `http://www.windriver.com` (2009).
Cited on p. 37

[Wu96] Y. K. Wu, V. N. Litvinenko, B. Burnham, J. M. Madey, & S. H. Park. *The Performance of the Duke FEL Storage Ring*. Nucl. Instrum. Methods A **375**, 74 (1996).
Cited on p. 19

[Wu01] Y. K. Wu, V. N. Litvinenko, S. F. Mikhailov, O. A. Shevchenko, N. A. Vinokurov, N. G. Gavrilov, T. V. Shaftan, & D. A. Kairan. *Lattice Modification and Nonlinear Dynamics for Elliptically Polarized VUV OK-5 FEL Source at Duke Storage Ring.* Nucl. Instrum. Methods A **475**, 253 (2001).
Cited on p. 19

[Yam04] T. Yamada & P. Schuck. *Dilute Multi-α Cluster States in Nuclei.* Phys. Rev. C **69**, 024309 (2004).
Cited on p. 12, 13

[Yam05] T. Yamada & P. Schuck. *Single α-Particle Orbits and Bose-Einstein Condensation in ^{12}C.* Eur. Phys. J. A **26**, 185 (2005).
Cited on p. 5, 11, 13, 113, 116

[Zie10] J. F. Ziegler, M. D. Ziegler, & J. P. Biersack. *SRIM — The Stopping and Range of Ions in Matter (2010).* Nucl. Instrum. Methods B **268**, 1818 (2010).
Cited on p. 57, 60, 63

[Zim11] W. R. Zimmerman, N. E. Destefano, M. Freer, M. Gai, & F. D. Smit. *Further Evidence for the Broad 2_2^+ State at 9.6 MeV in ^{12}C.* Phys. Rev. C **84**, 027304 (2011).
Cited on p. 6, 8, 90, 115

[Zim13] W. R. Zimmerman, M. W. Ahmed, B. Bromberger, S. C. Stave, A. Breskin, V. Dangendorf, T. Delbar, M. Gai, S. S. Henshaw, J. M. Mueller, C. Sun, K. Tittelmeier, H. R. Weller, & Y. K. Wu. *Unambiguous Identification of the Second 2^+ State in ^{12}C and the Structure of the Hoyle State.* Phys. Rev. Lett. **110**, 152502 (2013).
Cited on p. 3